

**Phase transformation in High Entropy Bulk Metallic Glass  
(HE-BMG) and Lamellar Structured-High Entropy Alloy (HEA)**



**Norhuda Hidayah Binti Nordin**

A thesis submitted for the degree of Doctor of Philosophy

**Department of Materials Science and Engineering**

**The University of Sheffield**

**2018**

*To my late father for his encouragement,*

*Hj Nordin Bin Saad*

## **DECLARATION**

I hereby declare that I have conducted, completed the research work and written the dissertation entitles “Phase transformation in High Entropy Bulk Metallic Glass (HE-BMG) and Lamellar structured -High Entropy Alloys (HEA)”. I also declare that it has not been previously submitted for the award of any qualification or other similar title of this for any other examining body or University. This dissertation contains fewer than 40,000 words including appendices, bibliography, footnotes, equations and tables and has fewer than 80 figures.

## ACKNOWLEDGEMENTS

Thanks God for his blessing I can finish my PhD journey successfully. I owe a debt of gratitude to the people around me for their support and kindness during my PhD studies. First and foremost, I would like to express my sincere gratitude to my supervisors, Prof Iain Todd and Dr Russell Goodall for their guidance, immense knowledge, endless support and treasured suggestions while allowing me to work on my own way. I would also like to say special thanks to the members in Mercury centre, Sorbey centre and technical staff especially Dean Haylock, Dawn Bussey, Joanne Sharp and Ben Palmer for their skill in guiding me to operate the machines confidently and never hesitate to help me in anyway. My sincere thanks also go to all the postdocs and colleagues, Dr Zhao Y Leong, Dr Philips Mahoney, Yuhe, Dr Dikai and Dr Gao that always share their knowledge and skill with me during my PhD programme.

I would also like to acknowledge my sponsors, Ministry of High Education Malaysia (MoHE) and International Islamic University Malaysia (IIUM) for the financial support that without which my time in UK would not have been possible.

To my dearest husband, Mohd Haikal Idris, thank you for your endless support despite the thousands of miles we have been apart during my final year. Your positive words and your faith in me and ever failed to give me strength to raise our 'PhD daughter', Aisya Insyirah on my own while doing this research. I have experienced a tough life when it comes to both studies and parenting responsibilities. But it is become a driving force for me to strive for the best in my studies. I also owe my mother, Mrs Fatimah Arshad and my parent in law, Mr Idris and Mrs Jamilah for their support and prayers for my success. To all my family members, thank you for always support me through my ups and downs life in the UK.

To my amazing best friends, Fadhilah, Aina and Atiqah who I shared the goods and tough times and always cherish my life. Thank you for always be there for me and lastly let's finish whatever we have started!

## TABLE OF CONTENTS

DECLARATION.....	i
ACKNOWLEDGEMENTS .....	ii
TABLE OF CONTENTS .....	iii
LIST OF TABLES .....	vii
LIST OF FIGURES.....	viii
ABSTRACT .....	xiii
CHAPTER 1 - INTRODUCTION .....	1
1.1 Introduction .....	1
CHAPTER 2 - LITERATURE REVIEW .....	4
2.1 High entropy alloys .....	4
2.1.1 A new concept of alloy design.....	4
2.1.2 Scientific approach to design HEA.....	7
2.1.3 Validity of empirical parameters to the formation of phases.....	9
2.1.4 Four core effects of HEA.....	14
1. High Entropy effect .....	14
2. Severe lattice distortion .....	15
3. Sluggish diffusion.....	16
4. Cocktail effect.....	17
2.2 Phase formation tendency in High Entropy Alloys .....	18
2.2.1 Solid solution .....	18
2.2.2 Intermetallic .....	19
2.2.3 Amorphous .....	22
2.3 The Metastability of Liquid in High Entropy Alloys .....	26
2.3.1 Phase transformation in HEAs.....	30
2.3.2 Crystallisation kinetics in HE-BMGs .....	32
2.4 Alloys design and properties of HEAs with secondary phases .....	37

2.4.1	Mechanical properties.....	38
2.5	Summary of literature review .....	49
CHAPTER 3 - METHODOLOGY .....		51
3.1	Introduction .....	51
3.2	Materials preparation.....	51
3.2.1	Arc melting and casting.....	51
3.2.2	Melt spinning .....	56
3.3	Annealing process .....	58
3.4	Characterisation techniques.....	59
3.4.1	Phase analysis .....	59
3.4.1.1	X-Ray diffraction (XRD).....	59
3.4.1.2	Determination of Phase Fraction by Rietveld refinement	60
3.4.2	Thermal analysis .....	61
3.4.2.1	Differential Scanning Calorimetric (DSC).....	61
3.4.2.2	Differential Thermal Analysis (DTA).....	62
3.4.3	Microscopy .....	62
3.4.3.1	Scanning Electron Microscopy (SEM).....	62
3.4.3.2	Transmission Electron Microscopy (TEM).....	62
3.5	Mechanical Testing.....	63
3.5.1	Compression testing.....	63
3.5.2	Hardness testing.....	64
3.5.2.1	Micro indentation tests .....	64
3.5.2.2	Nano indentation tests .....	64
CHAPTER 4.....		66
Crystallisation Kinetics and Thermal Stability of TiZrHfNiCu High Entropy Bulk Metallic Glass by Differential Scanning Calorimetry (DSC) .....		66
4.1	Abstract.....	66
4.2	Introduction .....	67
4.3	Theoretical background .....	69
4.4	Experimental procedure.....	71
4.4.1	Characterisations.....	72
4.4.2	Crystallization kinetics experiments.....	72

4.5	Result and Discussion.....	73
4.5.1	Alloys design .....	73
4.5.2	Non-isothermal annealing.....	79
4.5.3	Isothermal annealing.....	94
4.6	Conclusions .....	101
CHAPTER 5.....		102
Design of Lamellar-structured High Entropy Alloys with the Addition of Boron		
Content.....		102
5.1	Abstract.....	102
5.2	Introduction .....	103
5.3	Experimental procedure.....	105
5.4	Results and Discussion .....	106
5.4.1	Predictions of phase formation using empirical rules of HEA formation .....	106
5.4.2	Determination of phase presence by XRD characterisation .....	108
5.4.3	Refinement of lamellar microstructure through boron addition ..	117
5.4.4	Interfacial energy of the alloy systems .....	120
5.5	Conclusions .....	123
CHAPTER 6.....		125
Mechanical properties of Lamellar-structured High Entropy Alloys .....		
6.1	Abstract.....	125
6.2	Introduction .....	126
6.3	Experimental procedure.....	128
6.4	Mechanical properties.....	129
6.4.1	Strength and ductility change with boron addition.....	129
6.4.2	Deformation behaviour of lamellar structured HEA .....	133
6.4.3	Hardness change with boron addition.....	134
6.4.4	Nanoindentation and indentation size effect of different phases in the alloy .....	138
6.5	Conclusions .....	144

CHAPTER 7.....	145
7.1 Suggestions for Future Works.....	147
7.2 Contributions of Current Work.....	148
PUBLICATIONS AND CONFERENCE PRESENTATION .....	148
References .....	149
Appendix A .....	162
Appendix B.....	165

## LIST OF TABLES

		Pages
Table 2.1	List of produced high entropy metallic glass alloy with methods and references.	26
Table 2.2	The values of Avrami exponent ( $n$ ) in various crystallisation conditions [116]	36
Table 2.3	Example of typical hardness range for each phases in HEAs [19].	38
Table 4.1	Parameters of $\Delta H_{mix}$ , $\Delta S_{mix}$ , $\delta$ and $\Delta\chi$ for TiZrHfNiCu HE-BMG	74
Table 4.2	Atomic size ratios for the elements in alloys system [158].	75
Table 4.3	Summary of sample diameter with phase identification from the XRD patterns.	76
Table 4.4	Characteristic temperature ( $T_g$ , $T_{x1}$ , $T_{p1}$ , $T_{x2}$ , $T_{p2}$ and $\Delta T_x$ ) for TiZrHfNiCu HE-BMG alloy at different heating rates	80
Table 4.5	Apparent activation energy for the glass transition and crystallization by Kissinger, Ozawa and Augis-Bennet method.	83
Table 4.6	List of local activation energy at different crystallisation fraction of the TiZrHfNiCu HE-BMG	86
Table 4.7	The value of $n$ and $m$ of Avrami exponent to determine nucleation modes and crystallisation mechanism in the alloy respectively.	90
Table 4.8	The kinetic parameters of TiZrHfNiCu HE-BMG under isothermal annealing conditions.	97
Table 5.1	Parameters of $\Delta H$ , $\Delta S$ , $\delta$ and $\Delta X$ for FeCoNi( $B_x Al_{1-x}$ ) <sub>0.1</sub> Si <sub>0.1</sub> alloys.	106
Table 6.1	Vickers hardness values for FeCoNi( $B_x Al_{1-x}$ ) <sub>0.1</sub> Si <sub>0.1</sub> with increasing boron content	135
Table 6.2	Average hardness of three different phases FCC, lamellar (FCC+Fe <sub>2</sub> B) and FCC/BCC + lamellar in B0.7 and B1.0	143

## LIST OF FIGURES

		Pages
Figure 2.1	2D maps for $\delta$ - $\Delta H_{mix}$ on some of HEAs and BMGs [33].	10
Figure 2.2	Effect of $\Delta H_{mix}$ , $\delta$ , $\Delta\chi$ , $\Delta S_{mix}$ and VEC on phase stability in equi-atomic multi-component alloys and BMGs. The symbol $\circ$ symbolises equi-atomic amorphous phase forming alloys; $\bullet$ symbolises non-equi-atomic amorphous phase forming alloys; $\square$ symbolises solid solution phases and $\Delta$ symbolises intermetallic phases [36].	11
Figure 2.3	2D maps for correlation of $\delta$ - $\Omega$ on some of HEAs and BMGs [21].	13
Figure 2.4	The alloy fraction of solid solution (SS), intermetallics (IM) and mixture of solid solution and intermetallics (SS + IM) with increasing number of component at (a) $T = T_m$ and (b) $T = 600\text{ }^\circ\text{C}$ [55].	15
Figure 2.5	Difference of lattice distortion between BCC phase in one component alloy and BCC phase in five-component alloy [22].	16
Figure 2.6	(A) Diffraction patterns of CoCrCuFeNi and CoCrCuFeNiNb and SEM images of (B) CoCrCuFeNiNb coatings and (C) CoCrCuFeNi [78].	22
Figure 2.7	Time-temperature transformation diagram for bulk glassy, amorphous and crystalline alloys [83].	24
Figure 2.8	Phase evolution that occurs in HEAs during solidification process in liquid state [48].	30
Figure 2.9	Microstructure of the as-cast $\text{Al}_{0.5}\text{CoCrCuFeNi}$ by arc melting and casting [95].	31
Figure 2.10	Laser scanning Confocal Microscope (LSCM) micrograph shows lamellar structure of $\text{AlCoCrFeNi}_{2.1}$ HEA in low magnification and (b and c) SEM micrograph where A and B symbols indicate two different phases in the structure while BII shows nanoprecipitate of B2 phase within the FCC phases [127].	40
Figure 2.11	(a) XRD patterns of as-cast $\text{AlCoCrFeNi}_{2.1}$ HEA alloys and b) DSC curve of the alloy in both heating and cooling process [127].	41

Figure 2.12	Tensile stress strain curve of AlCoCrFeNi <sub>2.1</sub> HEA at a) room temperature and b) at 600°C and 700°C, respectively [127].	41
Figure 2.13	The pseudo binary phase diagram of CoCrFeNiNb <sub>x</sub> alloys developed by Thermo-calc software.	42
Figure 2.14	SEM images of CoCrFeNiNb <sub>x</sub> alloys; (a and b) x = 0.1 shows divorced eutectic (c and d) x = 0.25 shows hypo-eutectic; (e and f) x = 0.5, hypo-eutectic; (g and h) x = 0.8, hyper-eutectic and (i) x = 0.65, eutectic. The proeutectic phases are symbolled as A while the eutectic is marked as B [128].	43
Figure 2.15	(a) Engineering stress-strain curve and (b) hardness of CoCrFeNiNb <sub>x</sub> EHEA with increasing Nb content [128].	44
Figure 2.16	(a) Surface topography of as-cast AlCoCrFeNi <sub>2.1</sub> EHEA taken before nanoindentation mapping (b) hardness maps shows clear lamellar structure and (c) Histogram from the hardness values of the alloys.	45
Figure 2.17	Mechanism of deformation in the TRIP-DP-HEA with increasing tensile deformation at room temperature. a), EBSD phase maps illustrating the deformation-induced martensitic transformation as a function of deformation where $\epsilon_{loc}$ is the local strain and TD is the tensile direction. b), ECCI analyses presenting the evolution of defect substructures in the FCC. and HCP. phases where g is the diffraction vector, $\gamma$ is the FCC phase and $\epsilon$ is the HCP. phase. c), Schematic drawings demonstrating the arrangement of microprocesses in the TRIP-DP-HEA.	46
Figure 2.18	Mechanical properties TRIP-DP-HEAs compared to various single-phase HEAs [137]. a) The engineering stress-strain curve of DP-HEAs with respect to grain sizes, b) Strain-hardening response where the inset shows how the stability of the FCC. phase was improved upon grain refinement to increase the strain-hardening ability.	47
Figure 3.1	(a) MAM1 arc melting machine, (b) schematic of melting process (c) melting hearth attached to the arc melting machine, (d and e) ingot of 5g and 8g respectively.	54
Figure 3.2	(a) MAM1 casting configuration, (b) schematic of casting process (c) casting hearth attached to the arc melting machine, (d) different size of mould used (e) sample after casting.	55
Figure 3.3	Figure (a) Melt spinning machine, (b) molten alloy inside the chamber during spinning process, (c) schematic process of melt spinning process, (d and e) melt spun ribbon at 20m/s and 40m/s speed respectively.	57

Figure 3.4	Parameter profile for (a) isothermal annealing (b) non-isothermal annealing process.	59
Figure 3.5	Illustration for indentation array region in 50 $\mu\text{m}$ sample area.	65
Figure 4.1	Relationship of heat of mixing among constituent elements in the TiZrHfNiCu HE-BMG alloy	74
Figure 4.2	XRD patterns of the as prepared TiZrHfNiCu alloy at different casting diameter.	76
Figure 4.3	XRD pattern of fully crystalline TiZrHfNiCu alloy with diameter of 2 mm produced by [79] for comparison.	77
Figure 4.4	(a) SEM micrograph of the as cast TiZrHfNiCu HE-BMG and (b) Composition mapping of constituent elements Cu, Zr, Ti, Ni and Hf.	79
Figure 4.5	DSC curves of TiZrHfNiCu sample recording at various heating rates	79
Figure 4.6	(a) Kissinger plot, (b) Ozawa plot and (c) Augis-Bennett plot of TiZrHfNiCu HE-BMG alloy	82
Figure 4.7	Plots of crystallized volume fraction $x$ , versus temperature of TiZrHfNiCu HEBMG at different heating rates for (a) first and (b) second crystallization events	85
Figure 4.8	Plot of activation energy at difference crystallisation fraction for first and second crystallisation process	86
Figure 4.9	JMA plots of TiZrHfNiCu HE-BMG at different heating rates for (a) first and (b) second exothermic peaks.	89
Figure 4.10	Kissinger-Akahira-Sunose (KAS) plots for different crystallization volume fractions $x$ at (a) first and (b) second exothermic peaks.	92
Figure 4.11	Local activation energy ( $E_a$ ) on the degree of crystallization volume fraction	92
Figure 4.12	Isothermal DSC curves at various annealing temperature.	94
Figure 4.13	Crystallisation volume fraction, $x$ as a function of annealing time for various annealing temperatures.	95
Figure 4.14	Crystallisation volume fraction as a function of annealing time for different annealing temperature.	96

Figure 4.15	Local Avrami exponent as a function of crystallisation fraction at different annealing temperature.	97
Figure 4.16	Plots for activation energy determination for isothermal annealing in TiZrHfNiCu HE-BMG	99
Figure 4.17	Activation energy as a function of crystallisation volume fraction, $x$ in isothermal mode	99
Figure 5.1	XRD patterns of $\text{FeCoNi}(\text{B}_x\text{Al}_{1-x})_{0.1}\text{Si}_{0.1}$ with increasing boron content	108
Figure 5.2	Phase fraction of each composition determined from experimental XRD data by Rietveld refinement	109
Figure 5.3	$T_m$ , $T_c$ and $T_\Omega$ for the range of $\text{FeCoNi}(\text{B}_x\text{Al}_{1-x})_{0.1}\text{Si}_{0.1}$ compositions where the blue, orange and grey regions indicate areas where $T_m > T_\Omega$ , $T_\Omega > T_c$ , and $T_c > T_\Omega$ respectively. Values of $T_c = T_m - \Delta T_c$ are obtained via Equation 5.1. (a) $T_c$ values calculated based on $X = 0.4$ , (b) $T_c$ values calculated based on $X = 0.23$ . Blue regions indicate the preference for formation of disordered structures, gray regions indicate the increase stability of metastable semi-ordered structures, while orange regions indicate the preferred formation of ordered structures. Figure 5.3 (b) is in better agreement with the XRD characterisation in Figure 5.2 compared to Figure 5.3 (a), and is suggestive of the increased metastability of HEAs	114
Figure 5.4	SEM images (backscattered mode) of $\text{FeCoNi}(\text{B}_x\text{Al}_{1-x})_{0.1}\text{Si}_{0.1}$ lamellar structured HEA; (a) $\text{FeCoNi}(\text{Al}_{0.1}\text{Si}_{0.1})$ HEA alloys, (b) $\text{FeCoNi}(\text{B}_{0.2}\text{Al}_{0.8})_{0.1}\text{Si}_{0.1}$ , (c) $\text{FeCoNi}(\text{B}_{0.4}\text{Al}_{0.6})_{0.1}\text{Si}_{0.1}$ , (d) $\text{FeCoNi}(\text{B}_{0.5}\text{Al}_{0.5})_{0.1}\text{Si}_{0.1}$ and (e) $\text{FeCoNi}(\text{B}_{0.7}\text{Al}_{0.3})_{0.1}\text{Si}_{0.1}$ (f) $\text{FeCoNi}(\text{B}_{0.9}\text{Al}_{0.1})_{0.1}\text{Si}_{0.1}$ , and (g) $\text{FeCoNi}(\text{B}_{1.0})_{0.1}\text{Si}_{0.1}$	117
Figure 5.5	Herringbone-like pattern in (a) $\text{FeCoNi}(\text{B}_{0.9}\text{Al}_{0.1})_{0.1}\text{Si}_{0.1}$ (b) $\text{FeCoNi}(\text{B}_{0.1})_{0.1}\text{Si}_{0.1}$ HEA	119
Figure 5.6	Interfacial energy as a function of boron addition	121
Figure 6.1	Engineering stress-strain curves of $\text{FeCoNi}(\text{B}_x\text{Al}_{1-x})_{0.1}\text{Si}_{0.1}$ alloys at room temperature, obtained from compression testing	129
Figure 6.2	Compression engineering stress-strain curves of $\text{FeCoNi}(\text{B}_x\text{Al}_{1-x})_{0.1}\text{Si}_{0.1}$ alloys at room temperature	129
Figure 6.3	Compression strength and plastic strain of typical EHEAs under various strain rate: $\text{FeCoNi}(\text{B}_x\text{Al}_{1-x})_{0.1}\text{Si}_{0.1}$ , $\text{CoCrFeNiTa}_x$ [207], $\text{CoCrFeNiNb}_x$ [208], $\text{Co}_2\text{Mo}_x\text{Ni}_2\text{VW}_x$ [205], $\text{CoFeNiVMo}_x$ [205], $\text{CoFeNi}_2\text{V}_{0.5}\text{Nb}_x$ [206]	132

Figure 6.4	SEM images of compression fractured surface of FeCoNi(B <sub>x</sub> Al <sub>1-x</sub> ) <sub>0.1</sub> Si <sub>0.1</sub> (a) B = 0, (b) B = 0.2, (c) B = 0.4 (d) B= 0.9 at room temperature	133
Figure 6.5	Effect of interlamellar spacing and boron content on the hardness of the alloys	135
Figure 6.6	Hall-Petch plot of ln changed in hardness vs ln interlamellar spacing, $\lambda$	136
Figure 6.7	Optical microscope image of the sample surface after the indentation test of (a) the whole sample area,(b) magnified image of each indentation area with the hardness values in GPa (inside the dashed square region) of B0.7 alloy	139
Figure 6.8	Optical microscope image from the sample surface after the indentation test of (a) the whole sample area,(b)magnified image of each indentation area with the hardness values in GPa (inside the dashed square region) of B1.0 alloy	140
Figure 6.9	Distribution of hardness values of FCC, Fe <sub>2</sub> B and BCC/B <sub>2</sub> phases in B0.7 sample	143
Figure 6.10	Distribution of hardness values of FCC, Fe <sub>2</sub> B and BCC/B <sub>2</sub> phases in B1.0 sample	143

## ABSTRACT

An investigation into the phase transformation of metastable alloys such as high entropy alloys (HEAs) and high entropy bulk metallic glasses (HE-BMGs) was performed. Bulk metallic glasses (BMGs) and HEAs were known to have a metastable phase at high temperature, while HEAs was reported to have a sluggish diffusion at high temperature. Besides, the drawback of many single phase HEAs is that they are mechanically unstable due to the presence of single phase either body centred cubic (BCC) or face centred cubic (FCC) structures. Here, a systematic study on the crystal structure, physical and mechanical properties of TiZrHfNiCu HE-BMG and FeCoNi(B<sub>x</sub>Al<sub>1-x</sub>)<sub>0.1</sub>Si<sub>0.1</sub> (0 ≤ x ≤ 1) lamellar structured HEA were explored. It was revealed that, a phase transformation occurred in HE-BMG in isothermal and non-isothermal conditions, yet the nucleation and growth behaviour was relatively slow at high temperature compared to most Zr-based amorphous alloys. This phenomenon was proven by the attained data of activation energy and crystallisation mechanism which reflect the crystallisation resistance of the alloy. The addition of boron as a substitution of aluminium in FeCoNi(B<sub>x</sub>Al<sub>1-x</sub>)<sub>0.1</sub>Si<sub>0.1</sub> alloy changed the phase formation, phase stability, morphology characteristics and mechanical properties of the alloy. The unique lamellar herringbone-like structure was formed with increasing boron content and led to improvement of mechanical properties of the alloy such as the hardness from B0.4 to B1.0. Lamellar structured-HEA was designed to obtain a balance in strength and ductility for FeCoNi(B<sub>x</sub>Al<sub>1-x</sub>)<sub>0.1</sub>Si<sub>0.1</sub> HEA where it can be tailored by modifying the boron content. The optimum balance of strength (1550 MPa) and ductility (19%) was attained at 0.5 at% boron content.

# CHAPTER 1

## INTRODUCTION

### 1.1 Introduction

Back in 10,000 BC, pure metal such as gold, copper, bronze and iron have contributed to human civilisation, since humans relied on them for daily applications. After the Iron Age, humans started to develop stronger materials by adding small amounts of elements to improve its properties, such as producing steel and alloy steel. The alloying process of steel occurred accidentally when the iron interacted with carbon forming astonishing, high-performance material, such as wootz steel which was used widely and very popular as a Damascus sword in ancient times. In the 18th century when industrial revolution started in England, the development of advanced materials, especially in iron and textiles grew rapidly. Nearly 30 alloy systems were synthesised using various processes for variety of products [1]. However, all the systems are based on one principle element such as Fe-based alloy.

The improvement of alloy properties has been continuous. Nowadays, most advanced applications, such as in the aerospace sector require structures that demand new materials with excellent performance, low density and high thermal stability particularly at high temperature [2, 3]. The problems of imbalance in mechanical stability and instability of the materials at severe temperature reduces the components service performance and unreliability of the material for long-term usage. Consequently, extra time and cost is required for the development of new materials to overcome these problems. Alloys that have the right balance between strength and ductility and can resist phase changes at high temperature could provide solutions to some of these technical challenges that currently exist.

The discovery of High Entropy Alloys, HEAs occurred in 2002, arising due to scientific curiosity among the researchers who realised that almost all materials designed are based on one major element. There are huge numbers of possible phases in the middle of the phase diagram that can be explored and expanded to utilise the benefit of all elements involved in making potential new material. Supporting this view, a wide array of possible phases has been produced by the combination of multiple equi-atomic components, including single phase, multiple phases, nanocrystalline and amorphous alloys. The HEAs in their own right were originally proposed to benefit from solid solution stabilisation through entropy maximization and sluggish diffusion, particularly at high temperature. Yet, the stability of the mentioned phases might be different from a thermodynamic viewpoint.

Currently, most of the discovered HEAs emphasise single phase solid solution formation, such as BCC or FCC, that may in general have either high strength or good ductility respectively [4]. A refractory alloy, VNbMoTaW with a BCC phase has exceeded a conventional superalloy, Inconel 718, with a good yield strength at 1440°C, yet has a very poor ductility even at room temperature [3], while for the FCC type HEA, CoCrFeNiMn has been reported to have a very good ductility and good thermal stability, but cannot be used for high strength applications particularly at high temperature [5-7]. Therefore, a precipitation or addition of second phase of different character may be a way for supporting the single phase HEAs by precipitation strengthening. The second phase could be an intermetallic compound or disordered solid solution phases. Controlled distribution of the second phases such as particle sizes and spacing can retain the effectiveness of the alloys at high temperature by particle strengthening. Although exploring new alloy compositions for HEA continues to be important, focus is now being turned towards the development of HEAs with a

good combination of mechanical properties and phase stability at high temperature. This alloy could be possible to be used in various technological field such as aerospace, energy, transportation and manufacturing.

The current project is mainly discussed the metastability of HEAs which focussed on the phase formation in HEAs. This including a study of kinetics of phase transformation in HEAs such as nucleation, crystallization and phase clusters formation. Moreover, the novel alloys are designed to obtain a strength-ductility balance in a HEA with a systematic approach. Therefore, in this thesis, the topics has been divided into several chapters.

Chapter 2 provides a review of the published literature related to this study while in Chapter 3, the methodology including sample preparation, characterisation, equipment used, and mechanical testing are described accordingly. Chapter 4 emphasises the understanding of phase transformation and crystallization kinetics that occur in amorphous type HEAs by means of the glassy alloy being annealed in isothermal and non-isothermal conditions. Chapter 5 mainly centres on the design of a novel lamellar structured HEA by addition of boron to form a second phase in solid solution HEA with BCC/B2 structure, microstructural characterisation and discussion of the metastability of this alloy after undercooling state. Chapter 6 discusses the mechanical properties and deformation behaviour of the designed alloys that relate to their structures.

## CHAPTER 2

### LITERATURE REVIEW

#### 2.1 High entropy alloys

##### 2.1.1 A new concept of alloy design

Traditionally, the conventional alloy development strategy followed a system whereby a major element was chosen as a matrix while small amount of alloying element was added into the system as a solute to improve the properties of the main component. Alloying additions can tune the mechanical, and other properties of the materials by modifying the chemical properties of the alloys, like the addition of chromium to form stainless steel. This concept of alloy design has successfully generated numerous of applications that contribute to civilization and daily life. However, the route has led to huge amount of multicomponent alloy systems that are limited to one or two principal elements with the variation of properties depending only on the main elements. Therefore, the knowledge of the alloys containing several main component in equi-atomic or near equi-atomic proportion is desirable to explore the properties of the alloy in the centre of the phase diagram [8].

The enthusiasm to discover unexplored areas of the phase diagram was started in the late eighteenth century by Franz Karl Achard who studied the multi-principal equi-mass alloys with five to seven elements [9]. About two centuries later, Alain Vincent supervised by Brian Cantor synthesised several equi-atomic multicomponent alloys and found that an alloy with a composition of  $\text{Fe}_{20}\text{Cr}_{20}\text{Ni}_{20}\text{Mn}_{20}\text{Co}_{20}$  can form a single phase FCC solid solution that solidifies dendritically, when processed by melt spinning techniques [10]. The work was published in 2004 before Cantor moved on to explore another interesting area in HEAs field which is high entropy metallic glass

alloys (HE-BMGs) [11]. In 1995, Yeh proposed a new concept for multicomponent alloys by naming it “High Entropy Alloys” introducing the idea that the high mixing entropy is the key factor that contributes to the simplification of the crystalline phases in such high order mixtures of elements [12]. These alloys have been reported to form either a single solid solution or a combination of solid solutions consisting of simple crystal structures. HEAs also reputedly tend to possess several excellent properties such as good oxidation resistance, good hardness, high strength, and wear resistance.

This new concept changed the perception that a complex alloy would cause the formation of undesirable intermetallic compounds that weaken its mechanical properties as predicted by many binary and ternary phase diagrams [13]. The Hume Rothery rules explained the concept of mutual solubility of solvent and solute components in binary alloys where the 1) crystal structures of each element are the same, 2) the atomic size difference is small, 3) the electron valence is low and 4) the electronegativity difference between the elements involved is small. All of these factors would enhance the mutual solubility between constituent components and lead to simpler phases. These factors also contribute to the interaction mechanism between the elements in the system. For example, the formation of intermetallic compound occurs when the enthalpy of mixing is negative, where the attractive interaction forms ordered structure, and positive enthalpy of mixing leads to segregation and clustering while the disordered solid solutions form when the enthalpy of mixing approaching zero [14].

Thermodynamically, the equimolar multicomponent alloys do tend to be more stable due to their high entropy of mixing which can be divided into four factors; that are configurational, vibrational, magnetic dipole and electronic randomness [15, 16]. However, configurational entropy is the main factor. This can be calculated from the

Debye temperature at high temperature [16]. In equi-atomic multicomponent alloy systems, the relationship between configurational entropy and complexity of the system can be described by the Boltzman's equation as below:

$$S_{conf} = k \ln \Omega = -R \ln \frac{1}{n} = R \ln n \quad \text{Equation 2.1}$$

where  $S_{conf}$  is configurational entropy or entropy of mixing,  $k$  is Boltzman's constant ( $1.38 \times 10^{-23}$  J/K) and  $\Omega$  is number of ways atoms can position themselves in a non-equivalent lattice point of the crystal unit cell and  $n$  is number of component in the system. As the number of components increases, the system gets more disordered, and thus reduces the tendency to form complex structures. Therefore, HEAs can be defined as a multicomponent equal-molar alloy systems involving at least 5 metallic elements where each element has a composition between 5 to 35 at.% and a simple solid solution structure (BCC, FCC or HCP) is formed rather than intermetallic compounds when more elements are added into the system [17-19].  $S_{conf}$  for equimolar alloys with 3, 5, 6, 9, and 13 elements are 1.1R, 1.1R, 1.61R, 1.61R, 1.79R, 2.2R and 2.57R respectively [20]. The addition of at least 5 elements in the alloy results in increasing of the configurational entropy. Thus high entropy alloys are defined as alloys with a configurational entropy higher than 1.5R where R is the gas constant [21].

Although the definition of HEA has been questioned and still under debate among researchers, the concept has opened the doors of research activities to explore the new area in metallurgy. Increasing numbers of publications with the keywords High entropy alloys have been reported from 2003 to 2014 [22]. Most of the publication involve the elements from the transition metals but not all form a simple solid solution. Therefore, a guideline has been proposed to predict the phase formation

in HEAs from different groups of elements to obtain various properties of alloys [23, 24].

### 2.1.2 Scientific approach to design HEA

A parametric approach has been developed to predict the phase formation in HEAs. The formation of solid solution HEA can be explained from the thermodynamic principles of Gibbs free energy where the configurational effect of HEAs reduces the free energy of solid solution state and facilitates their formation particularly at elevated temperature. According to the Second Law of Thermodynamics, the free energy of mixing can be expressed as:

$$G_{mix} = H_{mix} - TS_{mix} \quad \text{Equation 2.2}$$

where  $H_{mix}$  is the enthalpy of mixing,  $T$  is temperature and  $S_{mix}$  is the entropy of mixing. The configurational entropy is related to the atomic configurations and system complexity in the alloy. It is noticed that, higher values of configurational entropy is achieved when the system has an equi-atomic composition either in random solid solution or amorphous phase. Therefore, the alloys which are near or at equi-atomic conditions and have numbers of components  $n \geq 5$  have high  $\Delta S_{conf}$ .

Each element in a multicomponent system has neighbouring atoms with distinct species thus having different values of enthalpy for each atomic pair. Therefore, Miedema's model is used to calculate the total enthalpy of mixing for the multicomponent alloy system [25, 26]:

$$\Delta H_{mix} = \sum_{i=1, j \neq 1}^n 4 \Delta H_{ij} c_i c_j \quad \text{Equation 2.3}$$

where  $c_i$  and  $c_j$  is the atomic percentage of component  $i$  and  $j$  while  $\Delta H_{ij}$  is the enthalpy formation of the component interaction between the pairs.

Besides, there are other important factors to predict the solubility formation in binary system as according to the Hume Rothery empirical rules (namely atomic size

difference ( $\delta$ ), mixing entropy ( $\Delta S_{\text{mix}}$ ), electronegativity difference ( $\Delta\chi$ ), and VEC [27]. These factors are also applicable for multicomponent systems such as HEAs and BMGs.

### 1. Atomic size difference

Complete solubility can be formed when the atomic size difference between the atoms involved in the system is  $< 15\%$ . This will also reduce the strain energy contribution to mixing enthalpy and mixing free energy by reducing the effect of lattice distortion. On the other hand, large atomic size difference enhances the formation of intermediate phase such as an intermetallic compound or complex phases [28, 29]. Therefore, equation can be used to determine the atomic mismatch for the system.

$$\delta = 100 \sqrt{\sum_{i=1}^n C_i (1 - r_i/\bar{r})^2} \quad \text{Equation 2.4}$$

where  $\bar{r} = \sum_{i=1}^n c_i r_i$ ,  $c_i$  and  $r_i$  are the percentage content and atomic radius for the  $i$ th element and  $n$  is the total number of elements involved in the system.

### 2. Electronegativity

Electronegativity can be described as an ability of the atom to attract electron toward itself. In multicomponent alloys, this is related to electronic interactions between the constituent components. Small electronegativity difference occurs when pairs of electrons involved in the alloy composition have the same tendency to attract electron and share, which will tend to result in formation of a solid solution. Meanwhile, large electronegativity difference between atoms due to electronic charge transfer results in the formation of compound phase. As electronegativity is impossible to directly measure, there is several methods that have been used in the literature to

calculate the reactivities of the atoms such as Pauling [30], Mulliken [31], Allen [32] etc. In HEAs, the Pauling scale is mostly used; this derives from the measures of heats of formation and combustion of gaseous molecules as in Equation 2.5,

$$\chi = -\sqrt{c_i \sum_{k=0}^n (\chi_i - \bar{\chi})^2} \quad \text{Equation 2.5}$$

where  $\chi_i$  is the Pauling electronegativity for the respective  $i$ th element.

### 3. Valence Electron Concentration

VEC can be defined as the number of electrons in the outermost shell of the orbitals that function in the bonding mechanism, arising from electronic structure. VEC for this calculation is the count of the total electrons in the d-electron positions as well as in the valence band. The value of electron concentration per atom (e/a) ratio used in the Hume-Rothery rule can indicate the formation of different crystal structures (FCC, BCC or HCP) and determine the phase stability of the alloys. In HEAs, FCC has been reported to be stabilised at  $VEC > 8$ , BCC  $< 7$  while mixed phases of FCC/BCC or intermetallics are found to be occurred between  $7 < VEC < 8$ . This value can be obtained from Equation 2.6:

$$VEC = \sum_{k=0}^n c_i (VEC)_i \quad \text{Equation 2.6}$$

where  $c_i$  and  $VEC_i$  are the composition and the Valence Electron Concentration of the  $i$ -th element in the system.

#### 2.1.3 Validity of empirical parameters to the formation of phases

From the parameters that have been discussed above, various 2-D plots have been presented that show the relationship between parameters. It can be guidelines for the formation of phases in HEAs and BMGs. For example, Guo *et al.* [33] used 2D maps in Figure 2.1 to plot the data for  $\delta - \Delta H_{\text{mix}}$  on some of HEAs and BMGs. It can be identified that solid solution can be formed when  $\delta \leq 6.6$  and  $-11.6 < \Delta H_{\text{mix}} < 3.2 \text{ kJ/mol}$ .

Meanwhile, the glassy structure can be formed when  $\delta > 6.4$  and  $\Delta H_{\text{mix}} < 12.2 \text{ kJ/mol}$ . If competition from intermetallic phases can be ruled out by composition adjustment, HEA that locate in the amorphous phase region of the  $\delta$ - $\Delta H_{\text{mix}}$  plot are able to solidify to form metallic glasses. This has been proved by Gao who published a series of Zr based alloy formed by melt spinning [34]. Thus, this can be a prototype for a guideline to design the alloy with crystalline or glassy structure.

Inoue [35] has developed the following empirical rules to design high entropy bulk metallic glass (HE-BMGs). (1) For HEA requirement concept, the alloy must compose of more than three elements, the second and third rules favour the formation of BMGs which are (2) large atomic size differences, and (3) large negative mixing enthalpies. The high in entropy of mixing ( $S_{\text{mix}}$ ) and lower critical cooling rate are favourable for glass formation [24]. In order to form HE-BMG, it is suggested to choose HEAs that are predicted to form intermetallic phases rather than simple phases [19]. So, it will ease to form amorphous instead of crystalline structure.

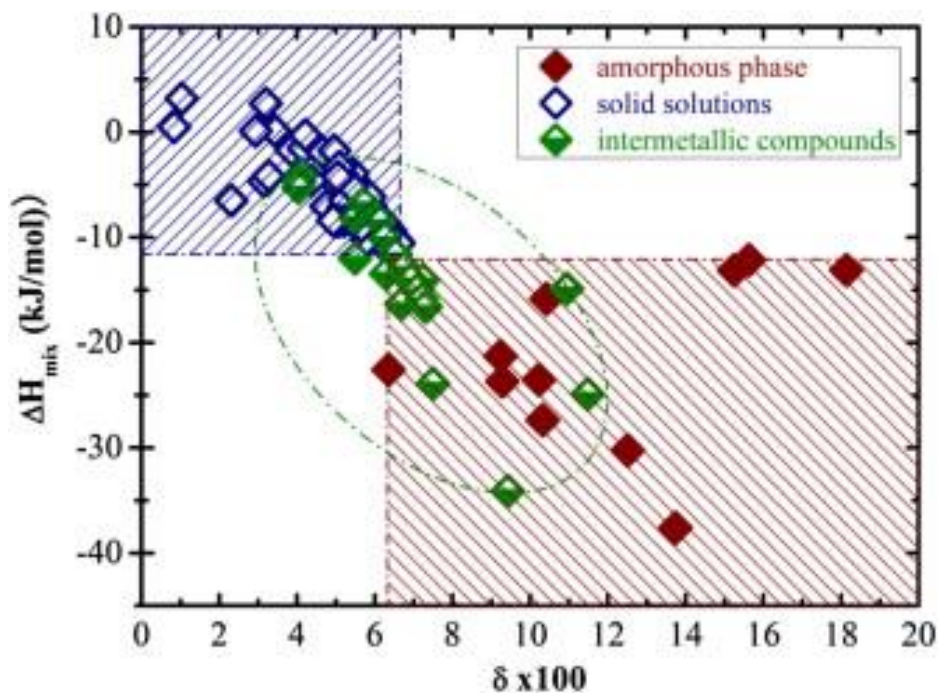


Figure 2.1: 2D maps for  $\delta$ - $\Delta H_{\text{mix}}$  on some of HEAs and BMGs [33].

Figure 2.2 gives a clear version on the range of value for VEC,  $\Delta\chi$ ,  $\delta$ ,  $\Delta H_{\text{mix}}$  and  $\Delta S_{\text{mix}}$  for the formation of equi-atomic amorphous alloy, non equi-atomic amorphous alloy, solid solution and intermetallic phases. The findings show that solid solution phases are formed in the positive value region of the  $\Delta H_{\text{mix}}$ , small different size between the elements ( $\delta$ ) and higher  $\Delta S_{\text{mix}}$ . In contrast, the formation of amorphous phase occurs at lower values of  $\Delta H_{\text{mix}}$ , high atomic size mismatch ( $\delta$ ) and lower  $\Delta S_{\text{mix}}$  value.

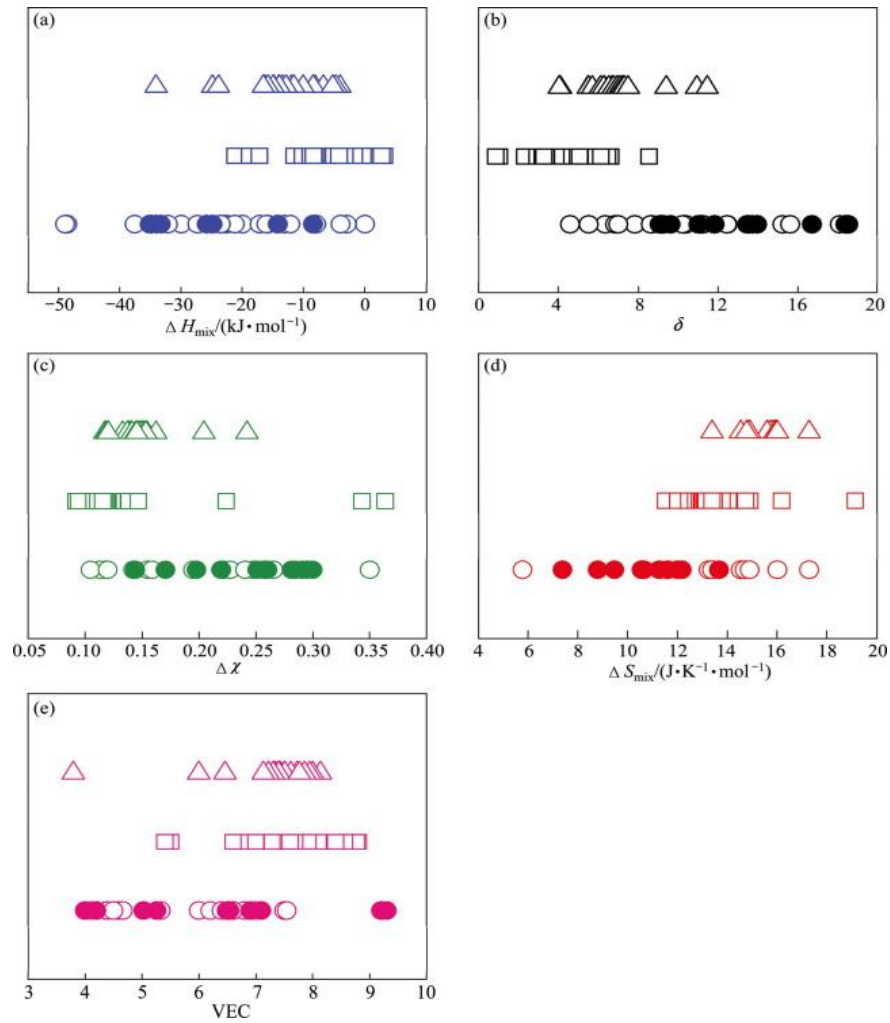


Figure 2.2: Effect of  $\Delta H_{\text{mix}}$ ,  $\delta$ ,  $\Delta\chi$ ,  $\Delta S_{\text{mix}}$  and VEC on phase stability in equi-atomic multi-component alloys and BMGs. The symbol ○ symbolises equi-atomic amorphous phase forming alloys; ● symbolises non-equi-atomic amorphous phase forming alloys; □ symbolises solid solution phases and △ symbolises intermetallic phases [36].

Detailed studies by Cunliffe *et al.* [37] deployed this method for glass formation in HEA based on critical temperature,  $T_c$  where it can be defined as the temperature where the particular composition gives the value of  $\Delta G_{mix}=0$  and it is given by:

$$T_c = \frac{|\Delta H_{mix}|}{\Delta S_{conf}} \quad \text{Equation 2.7}$$

It is also reported that, when the  $T_c$  of a potential HEA composition is higher than its solidus temperature, the high entropy phase is suppressed. The composition of  $(\text{TiZrNbCu})_{1-x}\text{Ni}_x$  were synthesised where  $x = 0.125, 0.15, 0.2,$  and  $0.25$ . At  $x = 0.125$  and  $x = 0.15$  where  $T_c \leq T_m$ , the precipitation of a dual phase microstructure containing Nb and a simple BCC phase was observed. Meanwhile at  $x = 0.2$  and  $x = 0.25$ , it was observed that  $T_c \geq T_m$  where the microstructure contained precipitation of complex  $\text{Ni}_{42}(\text{ZrTi})_{58}$  and  $\text{Cu}_{10}\text{Zr}_7$  phases. It is also noted that the alloy that showed low tendency to form crystalline structure in the XRD trace has low  $T_c$  whilst the alloy that easy to form crystalline structure has higher  $T_c$  than  $T_m$  of the alloy [37]. Yang and Zhang [21, 38, 39] also used the combination of  $\Delta H_{mix}$  and  $\Delta S_{mix}$  to develop a new parameter,  $\Omega$  to determine the stability of solid solution in the multicomponent alloys system as in Equation 2.8:

$$\Omega = \frac{T_m \Delta S_{mix}}{\Delta H_{mix}} = \frac{T_m}{T_c} \quad \text{Equation 2.8}$$

where  $T_m$  is the average of melting temperature calculated from the rule of mixture. The new guideline has been proposed where  $\Omega \geq 1.1$  and  $\delta \leq 6.6\%$  for solid solution phase to occur while intermetallic compound and BMG has smaller value of  $\Omega$  and larger value of  $\delta$  as in Figure 2.4 that shows a clear distinction between simple and complex phases through the 2D plot.

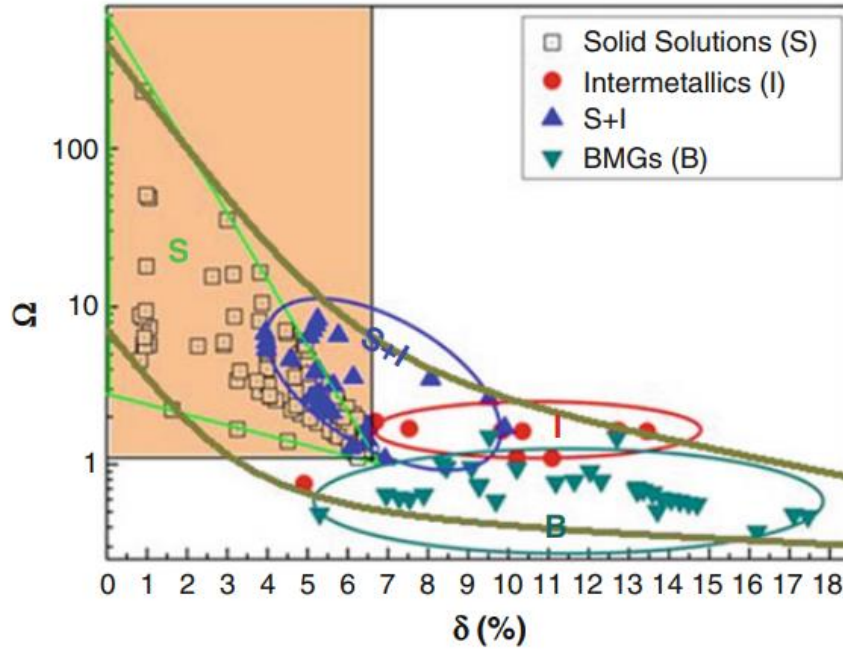


Figure 2.3: 2D maps for correlation of  $\delta$ - $\Omega$  on some of HEAs and BMGs [21].

In addition, highly integrated computational techniques have been developed such as MATLAB, CALPHAD [40-42] and *ab-initio* as an approach for predicting phase formation in HEA in more direct manner. *Ab-initio* simulation methods such as density functional theory (DFT) are used to generate a new database for intended phases or expand the information of the known database [43]. Atomistic methods [44] like molecular dynamic (MD) [45] and Monte Carlo (MC) [46] and continuum method are created for solving structures development such as nucleation, growth or phase cluster formation through fitting or extrapolating the information obtained from the experimental data [47]. Finite element method using thermodynamic database is used to determine microstructure and structure formation during materials processing. Therefore, combination of simulation and experimental works are essential to obtain optimisation in process, structure and property hence accelerating the process of making new alloys.

#### 2.1.4 Four core effects of HEA

According to the studies by Yeh *et al.* [48], four important factors that contribute to the phase formation and properties in HEAs have been proposed. The four core effects are high entropy, severe lattice distortion, sluggish diffusion and cocktail effect which then can be classified by thermodynamics, structure, kinetics and properties respectively [18, 48]. Therefore, the knowledge to predict stability of phases in HEAs is important for the alloys development strategy.

##### 1. High Entropy effect

Conventionally, the alloys with multiple elements are expected to produce complicated structure. In the early studies, it was claimed that, there is a low tendency for a complicated structure to occur in HEAs due to the high entropy effect that results in the formation of solid solution. As stated in Equation 2.2, high configurational entropy would potentially push lower the mixing free energy particularly at high temperature, result in simpler phase formation. However, most of the recent studies have shown the instabilities of the HEAs solid solution at all temperature up to melting. For example, Otto *et al.*[49] have investigated the phase stability of the first reported multicomponent alloy, CrMnFeCoNi [10] by prolong annealing at intermediate temperature. Interestingly it has found that, the precipitation of Cr-rich  $\sigma$  phase has occurred in the alloy when it was exposure below 800 °C. Therefore, CrMnFeCoNi is not a stable single phase below its solidus temperature. Since then, the stabilities of single phase HEAs have received a great deal of attention. Subsequent studies have been done with different HEA compositions to confirm this view [50-54]. From the reported studies of HEAs stability, it was found that, most of the single phase HEAs decompose into more than one phase when it was triggered to high temperature.

Besides, earlier studies also claimed that the configurational entropy reaches maximum when the elements are in equi-atomic proportion and increase with increasing number of alloying elements, leads to simpler phases and microstructure which is not as expected in conventional alloys [17]. However, studies by Senkov *et al.* [55] found that the formation of intermetallic phase are expected to form with increasing of alloying elements as shown in Figure 2.4. This scenario contradicts with the HEA design concept as stated above.

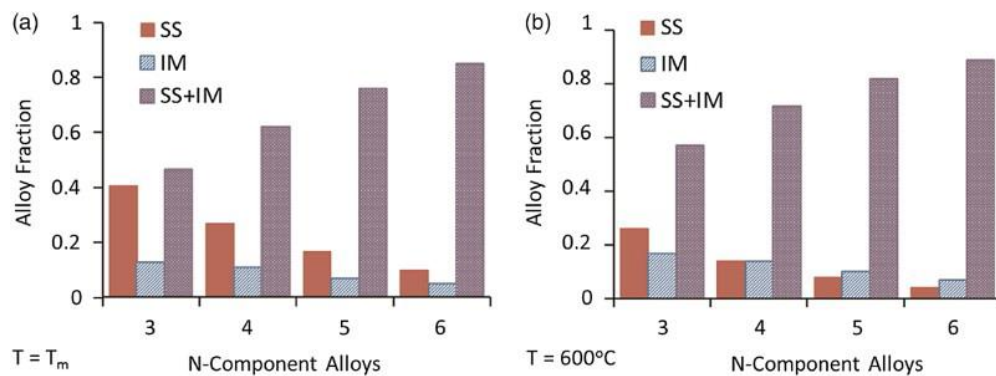


Figure 2.4: The alloy fraction of solid solution (SS), intermetallics (IM) and mixture of solid solution and intermetallics (SS + IM) with increasing number of component at (a)  $T = T_m$  and (b)  $T = 600^\circ\text{C}$  [55].

## 2. Severe lattice distortion

Since HEAs has the similar proportion (between 5 – 35 at%) of constituent elements, each of the elements can act as the matrix in the system. Figure 2.5 shows lattice distortion in solid solution HEAs are much severe than conventional alloys due to difference type of neighbouring atoms surrounding the system instead of just one kind of atom as the neighbour. The effect of lattice distortion also contributes to the changes in HEAs properties such as hardness [56], electrical properties, thermal conductivity [57].

Significant difference in atomic size between the atom contributes to the lattice distortion hence leading to solid solution strengthening [58]. Besides, different bonding energy and crystal structure also contributes to the formation of lattice distortion in non-symmetrical surrounding atoms [59]. This phenomenon can be detected using XRD whereby the decrease of XRD peak intensity indicates the lattice straining that may occur in the alloy bonding. However, it was argued by Pickering and Jones [60] in which the XRD peak intensity will also be effected by crystallographic texture, thermal vibration and fluorescence. Therefore, higher techniques need to be carried out as an attempts to accurately assess the lattice distortion effect in HEAs such as high resolution TEM (HR-TEM) [61] or using pair distribution function (PDF) analysis [62].

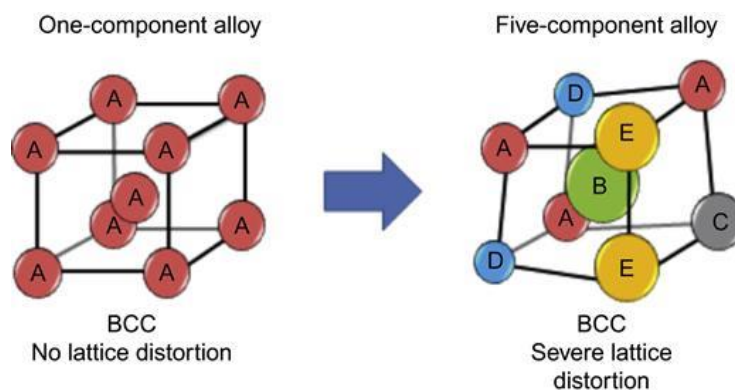


Figure 2.5: Difference of lattice distortion between BCC phase in one component alloy and BCC phase in five-component alloy [22].

### 3. Sluggish diffusion

It is also claimed that the diffusion mechanism in HEA is much slower than conventional alloy [19, 48, 63]. It is because, HEA has whole solute matrix compared to conventional alloy that has only one main matrix that control diffusion rate in the system. Therefore, a vacancy in the whole solute matrix is surrounded by atoms from different kind of elements during the diffusion. Besides, high potential energy

between the lattice sites (HEAs surrounded by different type of atoms and has different bond configuration which leads to different lattice potential energy), hinder the diffusion of the atom. This will result in sluggish diffusion kinetics and require high activation energy. Sluggish diffusion effect in HEA therefore has various advantages such as controlling phase transformation for a new phase to occur, high activation energy and reduce coarsening kinetics in grain growth process which can improve the properties of HEA especially at high temperature applications.

It has been reported that HEA has the most sluggish diffusion rate compared to conventional alloy and pure metal accordingly [59]. Tsai *et al.* proved his hypothesis by analysing the diffusion data on each element in ideal solid solution of FeCoNiCrMn and found that melting point normalised activation energy,  $\frac{Q}{T_m}$  value in HEA is the highest compared to pure metal of Fe, Co, Ni and stainless steel [59]. Having a high value of activation energy means that high kinetic reaction barrier is needed for the diffusion to occur.

#### **4. Cocktail effect**

The cocktail effect can be defined as the contributions of properties from mutual interaction of each of the component in HEA that mix in a complex way giving an enhancement of properties in the system. This is including size, morphology, grain size distribution, phase boundaries and properties of each element. For example, phase transformation from FCC to BCC has been occurred in FeCoCrCuAl<sub>x</sub> HEA as Al is increased until maximum value. Besides, the hardness value also increases as the phase transformation occurs from FCC, FCC+BCC to BCC showing that interaction of the constituent element in HEA derived from the cocktail effect [64].

## 2.2 Phase formation tendency in High Entropy Alloys

To date, a majority of HEAs in the published research papers reported more than one phase involved in the microstructure either in as-cast or after annealing states. The second law of thermodynamics mentioned that, there would be several possible states that will produce in the solid state of the alloy, however the lowest free energy of mixing would be at the equilibrium state [48]. The other competing possible states are solid solution phases, intermetallic compound or even amorphous phase at higher cooling rate. The competition has been attributed from enthalpy and entropy of mixing and atomic size difference among the constituent elements in the alloys.

### 2.2.1 Solid solution

In a single element, elemental phase is a terminal solid solution, while solid solution is the phase where all elements involve in the system have complete mixing having a structure of body centered cubic (BCC), face centered cubic (FCC) or hexagonal closed packed (HCP). The Hume-Rothery rules describe the factors that influence the formation of solid solution phase for a binary system. The idea also has been employed in BMGs and HEAs to understand the factors that contribute to the formation of different phases of alloys. The empirical rules include atomic size effect, electronegativity of each constituent element in the system and the electron concentration described in detail below [65]:

1. A complete solid solution can be obtained if the atomic size difference between solvent and solute is lower than 8%. However, a solid solution can still occur if the radii difference between each atom is less than 15%.
2. To prevent intermetallic compound formation, similar electronegativity between solvent and solute is preferable. Each atom with similar electronegativity will have similar attraction for electrons toward itself,

thus avoiding the formation of compound and potentially allowing a formation of simple solid solution.

3. Valence electron concentration (VEC) for solvent and solute is similar.
4. The system should involve elements with similar crystal structure.

It is vastly reported studies on single solid solution HEAs in the literature since the discovery of the first simple solid solution multicomponent alloys in 2004 [20]. For example, refractory elements HEAs such as MoNbTaW and MoNbTaVW have been synthesized and have shown to have single-phase BCC structure in the as-cast state [56]. On the other hand, the CCFN-type (CoCrFeNi) equi-atomic alloys usually exhibit a single phase FCC structure due to similar size, valencies and electronegativities among all elements [66].

### **2.2.2 Intermetallic**

Intermetallic compounds are complex phases with stoichiometric compositions that produce superlattices. For example, NiAl compound has a B2 structure while Ni<sub>3</sub>Ti having DO<sub>24</sub> structure. An intermetallic phase is the intermediate phase between solid solution and a fully stoichiometric intermetallic compound with partial solid solution. They may also be classified as ordered solid solutions. The structures of intermetallic compounds include sigma phase and Laves phases while intermetallic phase include ordered solid solution B2 and L12 phase.

#### **1. B2 phase**

The B2 phase is a cubic crystal structure with an ordered BCC phase where the atom in the body centred position and the atom at the corners are non-identical. B2 phase has been observed in most of HEAs either as a single phase or with BCC phase [64, 67, 68]. 3d transition elements for instance Fe, Co, Ni, Cr, Mn and Ti have a tendency to form b2 phase with high Al content [69, 70]. It is because, Al has strong affinity

especially with one of these elements to form B2 phase. While, the other elements involved may dissolve in the B2 phase due to mixing entropy effect. It has been reported that, B2 phase is claimed as BCC solid solution (A2 structure) instead of ordered B2 phase in most of HEAs studies because of large numbers of elements involved in the system making the intensity of superlattice reflection low [71]. It is found in  $Al_xNiCoFeCr$  HEA, BCC and B2 are always coherently present where the morphologies of each phase can be seen as weave like and spherical BCC nano-precipitates inside the B2 matrix respectively [72]. Besides, B2 phase also can be found by evolution of  $Al_xCoCrCuFeNi$  high-entropy alloy structure after heat treatment process from FCC phase with increasing Al content [73].

## 2. $L_{12}$ phase

$L_{12}$  phase is a cubic crystal structure from ordered FCC phase. The face centred is occupied by the atom of one type while the atom at the corner is another kind of atom. The presence of  $L_{12}$  phase in HEAs commonly occurs in the alloys containing Ni and Al that possesses FCC phase or  $L_{12}$  phase as major component. However, if the amount of Al is too high, the BCC or B2 phase otherwise will be formed [68]. Co-existence between FCC and  $L_{12}$  phase always is frequently observed in HEAs. This is because, both phases have nearly identical lattice parameter, making the XRD peaks overlap [68]. Therefore, when the volume fraction of ordered phase is low, XRD may reflect only to the peak belonging to disordered solid solution. Hence, TEM is required to determine the existence of  $L_{12}$  phase.

## 3. Sigma phase

Sigma phase,  $\sigma$  is a topologically close-packed phase in which components with larger atomic size occupy one definite set of lattice sites while smaller atoms occupy another set. The formation of sigma phase in fact is proof that the formation of solid solution

in HEA is not only depends on the configurational entropy alone but also be influenced by the interaction (enthalpy of mixing) and atomic size difference between the elements. Formation of  $\sigma$  phase in HEAs commonly occurs in HEAs containing V and Cr with the presence of Fe, Ni and Co. For Example,  $\text{Al}_{0.5}\text{CoCrCuFeNiV}_x$  has FCC crystal structure at  $x = 0$ , however multiple phases; FCC, BCC and  $\sigma$  phase forms as V is added to the system. The  $\sigma$  phase can be seen along with the BCC phase as  $x$  increases from 0.6- to 1.0 [74]. In addition, Cr is reported as a BCC stabiliser which also promotes the formation of  $\sigma$  phase along with the B2 phase in most equi-atomic alloys. Hsu *et al.* reported that,  $\text{AlCoCr}_x\text{FeMo}_{0.5}\text{Ni}$  HEA consists of B2 and  $\sigma$  phase. Volume fraction of  $\sigma$  phase in this alloy increases with the addition of Cr that causes the major phase to change from B2 to  $\sigma$  phase [75].

#### 4. Laves phase

Laves phase is intermetallic compound that has a complex structure with a stoichiometry of  $\text{AB}_2$ . The A atoms has an ordered structure in a diamond or hexagonal diamond shape while the B atoms assembles in tetrahedral position around the A atoms. There are three types of Laves phases; cubic  $\text{MgCu}_2$  (C15), hexagonal  $\text{MgZn}_2$  (C14) and hexagonal  $\text{MgNi}_2$  (C36). Laves phases have been reported in many HEAs either as major or minor components. The addition of Ti along with other transition elements contributes to the formation of Laves phases either as cast structure or by precipitation after heat treatment. For example, Cr-rich Laves has been observed with two BCC phases in  $\text{CrMo}_{0.5}\text{NbTa}_{0.5}\text{TiZr}$  as-cast alloy [76]. Moreover, Dong *et al.* reported that, in the absence of Al,  $\text{Al}_x\text{CoCrFeNiTi}_{0.5}$  alloys showed only a single FCC phase. However, as  $x$  increases up to 0.8, multiple phases have been observed where Laves phase is dominant along with BCC and FCC phase [77]. Figure 2.6 shows the XRD patterns and morphology images of  $\text{CoCrCuFeNi}$  before and after Nb coating.

In the absence of Nb, only dendritic (DR) and interdendritic (ID) can be seen in the SEM images which proved that only FCC phase is present. After Nb coating, (Co-Cr) Nb-type Laves has been observed along with the FCC phase which also contributes to the improvement of mechanical properties in the alloy [78].

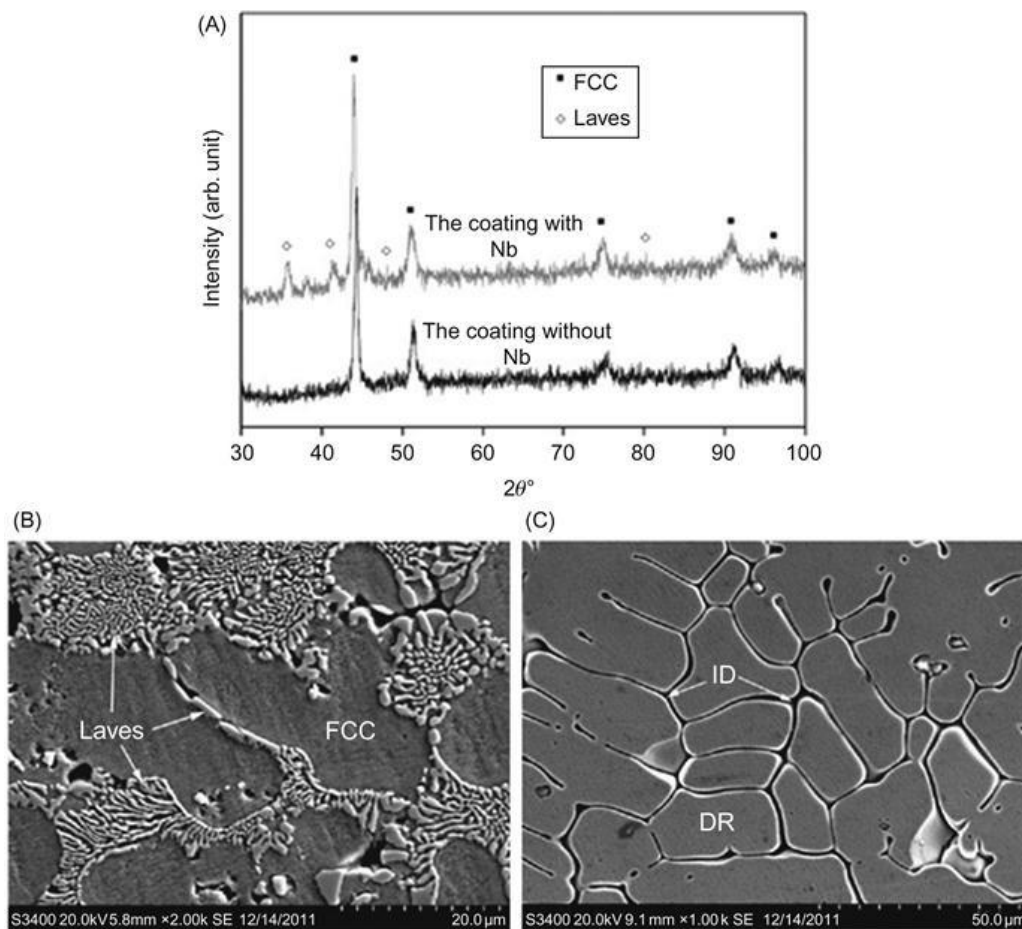


Figure 2.6: (A) Diffraction patterns of CoCrCuFeNi and CoCrCuFeNiNb and SEM images of (B) CoCrCuFeNiNb coatings and (C) CoCrCuFeNi [78].

### 2.2.3 Amorphous

In 2002, the idea for a new class of glasses namely high entropy metallic glass pioneered by Ma *et al.* [79] has been introduced by substituting a similar nature of elements in equal proportion in which the selection of the elements is well in accordance with the three empirical rules mentioned above. Compositional elements

involve including transition metals, metalloids as well as rare earth metals. Most of them is originally from conventional bulk metallic glass component elements. In the same year, Cantor *et al.* [10] produced a series of novel multicomponent alloys by equal atomic substitution and produced stable  $(\text{Ti}_{33}\text{Zr}_{33}\text{Hf}_{33})_{40}(\text{Ni}_{50}\text{Cu}_{50})_{50}\text{Al}_{10}$  amorphous alloy ribbons via melt spinning, however the alloy cannot be defined as a BMG due to the size (20–30  $\mu\text{m}$  thick).

The amorphous structure of high entropy metallic glass is obtained by extremely rapid cooling of the molten metal (normally  $10^2$ – $10^6$  K/s) at temperature below their glass transition temperature,  $T_g$  to prevent crystallisation. Under this condition, the molecules have very high mobility to follow any further decrease in temperature to reach equilibrium states. Yet, as the temperature decreases, the molecules were out of equilibrium as they are solidified at  $T_g$ . Therefore, amorphous formation is considered as kinetic phenomenon since it involves in inhibition of crystallisation nucleation and growth.

Figure 2.7 shows the Time-Temperature Transformation (TTT) diagram for  $\text{Al}_{0.5}\text{CuNiPdTiZr}$  alloy with different processes. The lowest critical cooling rate for glass formation is as low as  $0.067 \text{ Ks}^{-1}$  where the crystalline nose phase is in the right [80]. On the other hand, ordinary amorphous alloy and conventional crystalline alloy exhibit  $10^6 \text{ Ks}^{-1}$  and  $10^{15} \text{ Ks}^{-1}$  on their critical cooling temperature respectively. The thermal stability of metallic glass at low cooling rates enables the production of bulk metallic glass in bigger scale [81].

Differential Scanning Calorimetric (DSC) traces for metallic glass will give the information for the reduced glass temperature ( $T_{rg}$ ) which is the ratio between  $T_g$  and  $T_m$  [82]. Thus, high  $T_{rg}$  would give possibilities for the thicker glass to be synthesized at lower cooling rates. Besides, GFA also can be represented by super-

cooled liquid region [35]. It is measured by  $\Delta T_x$  which is the temperature interval between  $T_g$  and  $T_x$ . High value of  $\Delta T_x$  result in a good glass formation alloy.

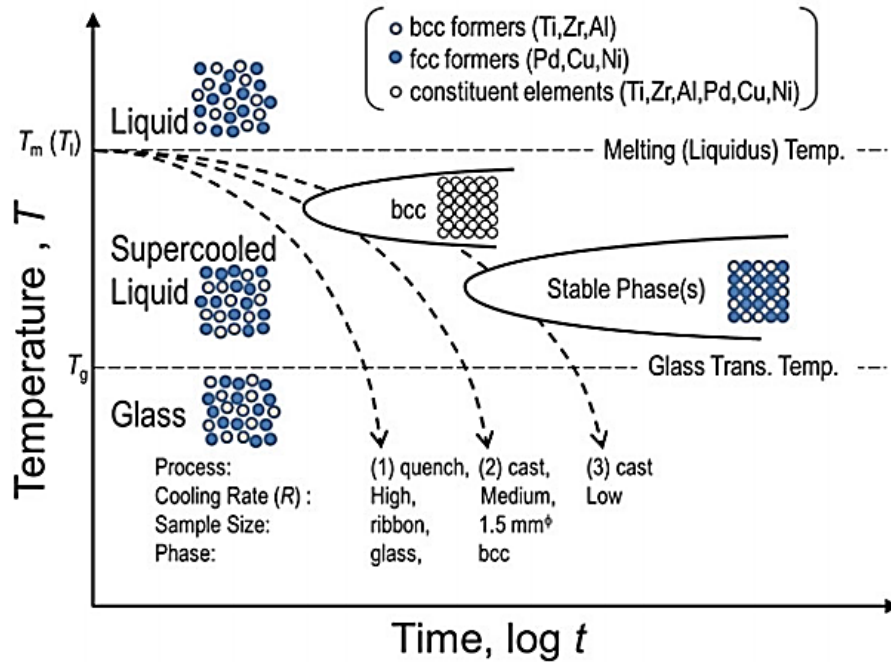


Figure 2.7: Time-temperature transformation diagram for bulk glassy, amorphous and crystalline alloys [83].

Based on the numerous glassy alloy system produced with high GFA, Inoue *et al.* suggested three empirical rules [35] which state that:

1. Three or more elements in multicomponent system increases complexity and size of the crystal unit cell reduced the formation of ordered structure thus increase the configurational entropy of super-cooled liquid phase.
2. Atomic radius different (about 12%) between constituents result in high packing density and low free volume in liquid state which need greater volume increase for crystallisation and has solubility limitation in crystalline state.
3. Negative heats of mixing between elements increase the energy barrier at solid liquid interphase and increase atomic diffusivity. It will impede

local atomic rearrangement and crystal nucleation rate hence prolong the super-cooled liquid temperature.

These rules can be very important as a guidance for selection of the metallic glass which is in contrast to the Hume-Rothery rules of solid solution as stated beforehand. Thus, by observing these rules, a good GFA with multi-component metallic material can be produced.

Various studies have been done over the last decade that focus on the development of multicomponent metallic glass alloy. Zr-based [84], Fe-based [85], Ni-based [86] and Ti-based [87] multicomponent amorphous alloy has been developed by utilizing the empirical rules strategy for good glass-forming ability (GFA) alloy. Those strategies are by selecting the major component, finding binary or ternary additions with a deep eutectic reaction with the main component and minor alloying additions to increase the GFA [88]. However, these studies are accumulated on the one or two main components. Indeed, only a number of studies have developed for amorphous alloys which have near equi-atomic or equi-atomic proportions as listed in Table 2.1. Table 2.1 summarises the HE-BMGs reported from 2002 until now, where the atomic substitution of typical BMGs appears to be a common approach.

From the table, it can be seen that an amorphous structure can be obtained via a regular preparation process as long as it can achieve a sufficient cooling rate as it cools rapidly from the molten state. For example, Takeuchi *et al.* has successfully formed the highest critical size of HE-BMG in 10mm diameter by flux water quenching [89]. However, the sample form crystalline phases at larger sizes. While, AlCrMoTaTiZr forms a BCC solid solution with Al<sub>2</sub>Zr structure when it is cast in bulk form. However, an amorphous structure can be obtained when it is deposited into a thin film by RF magnetron sputtering [93]. Therefore, it can be concluded that, cooling

rate plays an important role when forming an amorphous structure in high entropy metallic glass alloys.

Table 2.1: List of produced high entropy metallic glass alloy with methods and references.

Material	VEC	$\Delta\chi$	$\delta$	$\Delta H_{mix}$	$\Delta S_{mix}$	Method	Ref
ErTbDyNiAl	4.4	0.319	13.22	-27.04	13.38	CMC	[33]
SrCaYb(Li <sub>0.55</sub> Mg <sub>0.45</sub> )Zn	4.09	0.261	15.70	-12.15	14.52	CMC	[33]
SrCaYbMgZnCu	4.1	0.305	16.36	-10.6	14.53	CMC	[33]
PdPtCuNiP	9.2	0.159	9.285	-23.68	13.38	FWQ	[89]
CaMgZnSrYb	4.2	0.255	15.25	-13.12	13.38	CMC	[90]
CuNbNiTiZr	6.8	0.22	9.25	-21.28	13.38	MS	[37]
ZrHfTiCuNiAl	5.4	0.23	8.89	-31.05	14.56	MS	[91]
ZrHfTiCuNi	6.6	0.27	10.32	-27.36	13.38	CMC	[79]
ZrHfTiCuFe	6.2	0.25	10.42	-15.84	13.38	MS	[79]
ZrHfTiCuCo	6.4	0.26	10.23	-23.52	13.38	MS	[79]
ZrTiNiCuBe	6.2	0.77	12.52	-30.24	13.38	CMC	[79]
FeSiBAlNi	5.47	0.16	16.90	-40.52	14.87	MA	[92]
TiZrNbCuNi	6.8	9.258	0.22	-21.28	13.38	MS	[37]
AlCrMoTaTiZr	4.67	0.26	9.09	-16.11	14.90	MS	[93]

\*CMC is copper mould casting, FWQ is flux water quenching, MA is mechanical alloying, MS is melt spinning and IC is injection casting.

### 2.3 The Metastability of Liquid in High Entropy Alloys

Difference in Gibbs free energy,  $\Delta G$ , between metastable phase and stable phase is a vital parameter to investigate the phase stability of the alloys for example the determination of phase boundary and the kinetics of phase transformation [94].

According to Gibbs free energy,  $\Delta G_{mix} = \Delta H_{mix} - T\Delta S_{mix}$ , where  $\Delta H_{mix}$  and  $\Delta S_{mix}$  are the enthalpy of mixing and entropy of mixing respectively, the large number of elements will contribute to high value of  $\Delta S_{mix}$  thus lowering the mixing free energy. In the solid state, solid solution HEA have a good stability especially at high

temperature due to sluggish diffusion effect. However, numerous possible phase formation (ie: crystalline, intermetallic or amorphous) and the kinetics of sluggish diffusion effect in HEAs, make the kinetics of phase transformation more complex and intriguing. Zhang *et al.* [38, 39], has classified the stability of these alloys according to thermodynamic parameter,  $\Omega$  value by calculating the ratio of melting temperature to the ratio of the enthalpy of mixing to the entropy of mixing,  $\Omega = \frac{T_m}{T_c} = \frac{\Delta H_m}{\Delta S}$ . Solid solutions can be formed if  $\Omega \geq 1.1$

Melting temperature,  $T_m$  of the substance can be defined as the onset of the transition from crystalline solid to liquid state. In a single component system, the liquid and crystalline phases coexist at the same temperature in thermodynamic equilibrium. Meanwhile, in multicomponent system, the solid crystals are able to remain stable in a range of temperature above  $T_m$ . However, the crystals can coexist in stable thermodynamic equilibrium with the liquid at Liquidus temperature,  $T_l$ . Upon cooling of the molten metal HEA, solidification will start from  $T_l$  and finish at  $T_m$ . Crystallisation processes occur during liquid-solid transition where the equilibrium liquid transform to equilibrium crystalline solid which involve the nucleation and growth of the crystals.

Generally, crystallisation of a substance will start to occur at  $T_m$  or  $T_l$  for one component and multicomponent substance respectively. Metastable equilibrium condition is occurred when the liquid cooled below  $T_m$  or  $T_l$  without crystallising where it is referred to supercooling or undercooling. In some alloys, the crystallization temperature is very close to  $T_m$  or  $T_l$  thus no undercooling can be detected while for metallic glass and some HEA, the alloys are not crystallised for the entire range of undercooling and leads to liquid-glass transition.

The process of crystallization of the liquid started with the nucleation of the clusters of the stable crystal phase and it is related to the change in free energy. Therefore, the free energy changes can be described as in Equation 2.9:

$$\Delta G' = \Delta G_v + \Delta G_s \quad \text{Equation 2.9}$$

where  $\Delta G_v$  is the free energy obtain from the formation of the solid phase volume and  $\Delta G_s$  is the free energy from the creation of the liquid-solid interface. Since the phase transition from undercooled liquid to a solid is thermodynamically favoured, the sign of  $\Delta G_v$  will be negative while the interfacial energy from the creation of liquid can be calculated as  $\Delta G_s = \sigma A$  where  $\sigma$  and  $A$  is the interfacial energy and area of the interface respectively. The free energy of cluster formation can be expressed as:

$$\Delta G' = -V_s \Delta G_v^{l-x}(T) + \sigma A \quad \text{Equation 2.10}$$

where  $V_s$  is the volume of the cluster solid (assume as spherical) and  $\Delta G_v^{l-x}(T)$  refer as the difference in free energy per unit volume between liquid and crystalline states. The volume of the spherical crystal cluster can be determined as  $V_s = \frac{4}{3}\pi r^3$ , and area of the liquid-solid interface with surface area,  $A = 4\pi r^2$ , equation can be rewritten as:

$$\Delta G' = -\frac{4}{3}\pi r^3 \Delta G_v^{l-x}(T) + 4\pi r^2 \sigma \quad \text{Equation 2.11}$$

If the radius of the cluster smaller than critical value,  $r^*$  the system will be able to lower its free energy by dissolution of the solid cluster back into the liquid phase. On the other hand, if the cluster radius is larger than  $r^*$ , the cluster will form a stable nucleus. Thus, if  $r > r^*$ , result in lower value of  $\Delta G'(r)$ . The free energy of cluster formation,  $\Delta G'(r)$ , has a maximum of  $\Delta G^*$  at  $r^*$ . This is the critical free energy for the formation of the stable crystalline nuclei in the liquid phase, namely nucleation barrier.

By solving the equation  $\frac{d\Delta G'(r)}{dr} = 0$ ,  $\Delta G^*$  is found to be:

$$\Delta G^* = \frac{16\pi\sigma^3}{3(\Delta G_v^{l-x})^2} \quad \text{Equation 2.12}$$

where the *critical radius*;

$$r^* = \frac{2\sigma}{\Delta G_v^{l-x}} \quad \text{Equation 2.13}$$

The nucleation barrier can be expressed as a function of the undercooling,  $\Delta T$ :

$$\Delta G^* = \frac{16\pi\sigma^3 T_{liq}^2}{3(\Delta H_f)_v^2} \frac{1}{(\Delta T)^2} \quad \text{Equation 2.14}$$

Where  $\Delta H_f$  is per unit volume of latent heat of fusion which is the approximation from the Gibbs free energy curve. The exact approximation of the free energy difference between undercooled liquid and the crystal can be obtained by integration as below equation 2.15:

$$\Delta G^{l-x}(T) = \left(1 - \frac{T}{T_{liq}}\right) \Delta H_f - \int_{T_{liq}}^T \Delta C_p^{l-x}(T') dT' + \int_{T_{liq}}^T \frac{\Delta C_p^{l-x}(T')}{T'} dT' \quad \text{Equation 2.15}$$

Where  $\Delta G^{l-x} = \Delta H^{l-x} - T_{liq} \Delta S^{l-x} = 0$  at equilibrium, hence the difference of enthalpy and entropy difference between the liquid and crystalline states can be determined as below:

$$\Delta S_f = \frac{\Delta H_f}{T_{liq}} \quad \text{Equation 2.16}$$

The average size distribution of the cluster,  $N_r$  (where  $r$  is the radius of spherical cluster per unit volume) at any given moment from the large temperature can be given by:

$$N_r = N_0 \exp\left(\frac{\Delta G'}{kT}\right) \quad \text{Equation 2.17}$$

where  $N_0$  is the total number of atom per unit volume and  $G'$  can be obtained from Equation 2.11 for any value of  $r$ . For  $T > T_{liq}$  this expression is useable for all

value of  $r$ . However, the expression is only valid for  $r \leq r^*$  for  $T < T_{liq}$  because it is assumed that, at higher cluster size (bigger than  $r^*$ ), the cluster tend to grow rapidly to macroscopic sizes and leaving the liquid system forming nuclei.

### 2.3.1 Phase transformation in HEAs

Solidification process determine the microstructure formation and properties of HEA. Upon solidification, the liquid melt crystallised from the casting wall towards the centre of the mould. High mixing entropy effect contributes to solid solution formation at high temperature due to  $T\Delta S_{mix}$ . At slow cooling, segregation or precipitation of second phase may occur due to decreasing  $T\Delta S_{mix}$  hence forming a heterogeneous microstructure. However, the sluggish diffusion properties of some HEAs reduces the formation of precipitates. Figure 2.8 shows the transformation of phases during solidification of the alloys.

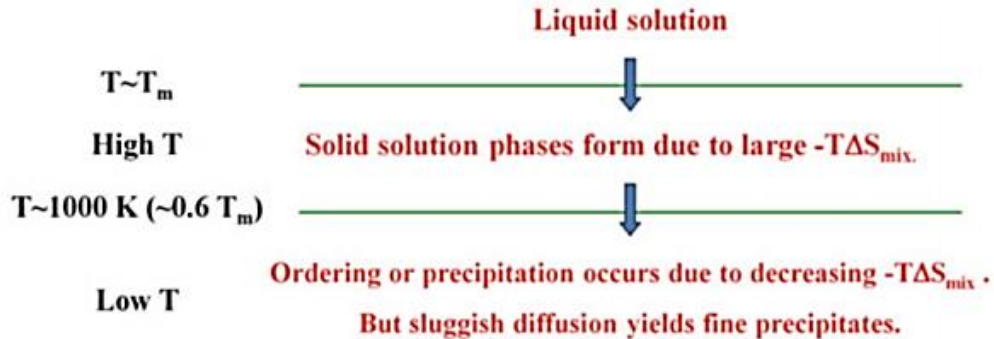


Figure 2.8: Phase evolution that occurs in HEAs during solidification process in liquid state [48].

Typically, dendritic microstructure with interdendritic (ID) segregation can be seen in HEA that is produced by arc melting and casting as shown in Figure 2.9. Faster cooling rate can suppress the precipitation of secondary phases therefore form a single-phase alloys. These can be obtained by different casting techniques such as splat quenching, melt spinning, injection casting, suction casting and drop casting. On the

other hand, if the multiple element alloy has limited mixing entropy at high temperature, intermetallic phases would form at high temperature. This will result in more complex phases with poor mechanical properties during cooling [48].

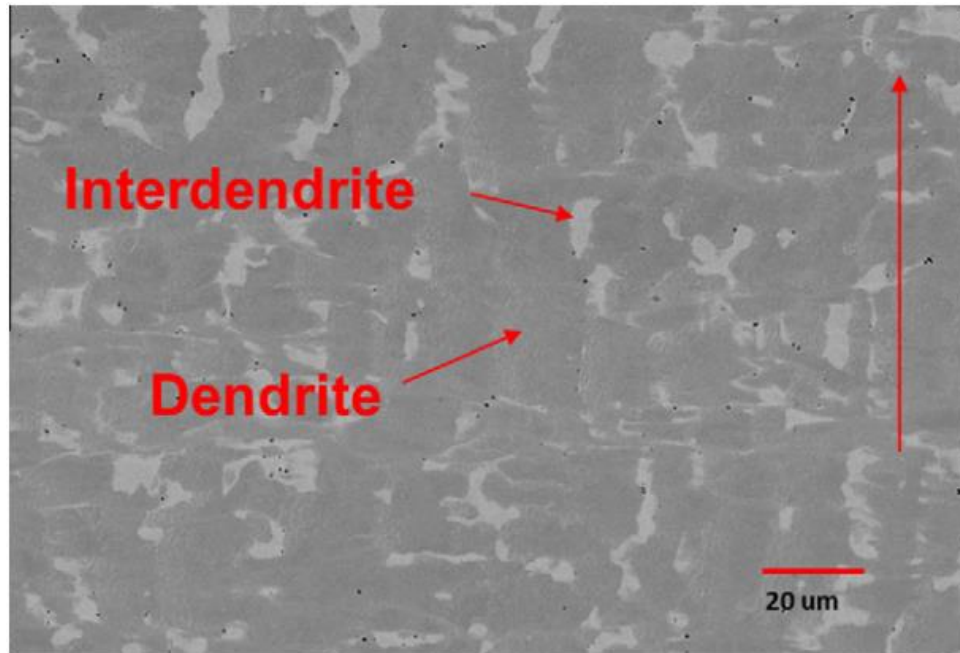


Figure 2.9: Microstructure of the as-cast Al<sub>0.5</sub>CoCrCuFeNi by arc melting and casting [95].

Phase transformation in HEAs also can be influenced by the lattice distortion and sluggish diffusion effect. It is then divided into two categories which is diffusion type and diffusionless type phase transformation. Spinodal decomposition, eutectic and eutectoid reaction, solidification, precipitation and dissolution are some of the examples for diffusion type phase transformation that commonly found in the phase diagram as the alloys undergo heating or cooling process. Annealing process with longer holding time will cause precipitation of second phase. The diffusion type phase transformation is commonly reported in literature related to HEAs. Meanwhile, diffusionless type phase transformation such as martensitic transformation can be

described as the movement of atom in restricted manner where atoms are travelled less than one interatomic spacing in any phase transformation [96].

It is also reported that, the formation of non-equilibrium simple solid solution is easy to be obtained under severe deformation (i.e mechanical alloying process) and undercooling condition (i.e sputtering deposition process) due to kinetic reasons where long-range atomic diffusion is inhibited [97]. The phase transformation in multi component elements HEAs to glassy structure is attribute from the topological instability and large atomic size difference based on Egami's principle [98, 99] which states that the glass formability of liquid for metallic alloy and glass system is influenced by local topological instability and atomic size mismatch. The atomic size mismatch with sluggish diffusion in HEAs enhances the formation of glassy phase by avoiding crystallization process and freezing atomic configuration at high cooling rates. Besides, Inoue's rule [35], selection of components for a deep eutectic [100] and confusion principle [13] has to be followed in order to avoid nucleation and growth process during cooling and to increase glass formability in solid solution.

### **2.3.2 Crystallisation kinetics in HE-BMGs**

Amorphous HEAs or high entropy bulk metallic glasses (HE-BMGs) appear to have a random distribution of atomic arrangement compared to regular HEAs. Crystallisation of amorphous liquid is rather a complex process because it involves simultaneous nucleation and growth of crystallites [101]. The theory of crystallisation in glassy alloys can be explained by considering the structure and the kinetics of crystallisation. Numerous research on investigation of crystallisation kinetics have been presented with different approaches to clarify the crystallisation process including mechanism, activation energy and correlation between kinetics and structural in amorphous alloys. However, the investigation of kinetics transformation

is only focussed on BMGs with little information is available to date for crystallisation kinetics of HE-BMGs [102]. The first report on crystallisation kinetics of HE-BMG was published by Gong *et al.* in 2005 by choosing  $\text{Ti}_{16.7}\text{Zr}_{16.7}\text{Hf}_{16.7}\text{Cu}_{16.7}\text{Ni}_{16.7}\text{Be}_{16.7}$  as composition using both non-isothermal and isothermal modes [103].

In the isothermal method, the sample is heated above the glass transition temperature and the heat absorbed during the crystallisation process is recorded as a function of time [103-106] while for non-isothermal method, the sample is heated at constant rate and the change of enthalpy is measured as a function of temperature [95, 103, 107, 108]. Non-isothermal experiments in comparison to isothermal ones, have the advantage of an easier and faster performance with a minor noise to signal ratio for kinetic experiments. Crystallisation behaviour of amorphous alloys can be determined by monitoring resistivity or heat evolution in order to detect phase transformation. Crystallization temperature,  $T_x$  has been used throughout the literature as indicator to measure thermal stability [101, 109, 110]. It is not an intrinsic property since it is affected by transformation kinetics. Therefore, it does not have a constant value because of the dependency of time and temperature. Differential scanning calorimetric (DSC) and differential thermal analysis (DTA) are thermoanalytical techniques that has been used widely for the rapid evaluation of thermally-induced transformations in amorphous alloys because of large exothermic heat is released generally accompanied with crystallisation process [101].

The utilisation of this techniques offered the promise of obtaining useful information for analysing the crystallisation kinetics of amorphous alloys. Numbers of mathematical equations have been proposed for interpreting the DTA and DSC results based on formal theory of transformation kinetics. Johnson, Mehl and Avrami have first defined an effective coefficient of crystallisation rate with dependence on

Arrhenian temperature. Later, several different ways of analysing the data has been proposed by Ozawa, Piloyan and Borchardt, Coats, Redfren and Sestak, Ozawa and Chen, Takhor, Kissinger and Augis and Bennet; where each has their own perspective thus leading to contradictory results. However, by taking consideration on temperature dependence and crystallisation rate coefficient, all the methods lead to similar conclusions [101] where the overall activation energy of the crystallisation process is the gradient of the straight lines between two parameters based on Johnson-Mehl-Avrami relation [111-114]. However, the range of applicability of the different non-isothermal methods of analysis must be considered, because most of them were obtained as approximations of theories which theoretical applicability is on isothermal regimes.

The theory of transformation kinetics describes the crystallisation fraction,  $x$  of the glass forming alloys with time,  $t$  in term of nucleation frequency per unit volume,  $I_v$  and the crystal growth rate,  $u$  which can be expressed in the basic expressions as in Equation 2.18:

$$x = 1 - \exp \left[ -g \int_0^t I_v \left( \int_{t'}^t u d\tau \right)^m dt' \right] \quad \text{Equation 2.18}$$

where  $g$  is the geometric factor influenced by the crystal growth and  $m$  is a numeral or half numeral that depends on the growth mechanism which measured by the dimensionality values of the crystal growth with  $u$  independent of time  $t$ . For the  $m$  value of 1, 2 and 3 indicates interface-controlled growth or diffusion-controlled growth of one-, two- and three-dimensional growth respectively. Meanwhile, for diffusion controlled where  $u$  decreases as  $t^{-1/2}$ ,  $m$  assumes the values  $1/2$ , 1 and  $3/2$  for respective dimensionality of growth.

For isothermal crystallisation with the nucleation and growth rate are independent of time, equation can be integrated to yield:

$$x = 1 - \exp(-g' I_v u^m t^n) \quad \text{Equation 2.19}$$

where  $n = m+ 1$  for  $I_v \neq 0$  and  $g'$  is factor of new shape. The resulting equation of the fraction transformed to nucleation rate, growth rate and time expresses by Johnson-Mehl and Avrami (J-M-A) relation to yield:

$$x = 1 - \exp[-K(t)]^n \quad \text{Equation 2.20}$$

where  $n$  can be obtained by mathematical manipulation of Equation 2.20 as below:

$$1 - x = \exp(-kt^n) \quad \text{Equation 2.21}$$

$$\ln(1 - x) = -kt^n \quad \text{Equation 2.22}$$

$$\ln[\ln(1 - x)] = \ln k - n \ln t \quad \text{Equation 2.23}$$

Therefore, the value of  $n$  can be obtained by taking the slope of the plot of logarithm  $(1-x)$  versus negative logarithm of  $t$  [115]. The details explanation of Avrami exponent value for different condition are states in Table 2.2:

Different approaches have been developed for analysis of the kinetics data that are obtained from non-isothermal experiments. Kissinger equation was firstly developed to investigate the variation of crystallisation temperature at different heating rate. Matusita *et al.* has improved the Kissinger's method by introducing the concept of nucleation and growth in the equation. This gives an information regarding the Avrami exponent and dimensionality of the growth. Studies by Greer identified that the average Avrami exponents,  $n$ , for the crystallisation process of Metglas 2605 Fe<sub>80</sub>B<sub>20</sub> alloys change from 0.7 to 4.87 [117]. However there was no clarification proposed for the low values of  $n$ . Nicolaus *et al.* [118] have studied the crystallisation kinetics of amorphous Zr<sub>67</sub>Co<sub>33</sub> BMG and obtained an average Avrami exponent of  $n$

= 2.44, which is also lower than 3. However, the value of  $n$  not dependable at different temperature.

Table 2.2: The values of Avrami exponent ( $n$ ) in various crystallisation conditions [116]

(i) Interface controlled growth	
Condition,	$n$
Increasing nucleation rate	>4
Constant nucleation rate	4
Decreasing nucleation rate	3-4
Zero nucleation rate (site saturation)	3
Grain edge nucleation after saturation	2
Grain boundary nucleation after saturation	1
(ii) Diffusion controlled growth	
Conditions, $n$	
All shapes growing from small dimensions	
Increasing nucleation rate	>2.5
Constant nucleation rate	2.5
Decreasing nucleation rate	1.5-2.5
Zero nucleation rate	1.5
Growth of particles of considerable initial volume	1-1.5
Needles and plates of fine long dimensions, small in comparison with their separation	1
Thickening of long cylinders (needles)	1
Thickening of very large plates	0.5
Precipitation on dislocations	~0.67

Augis and Bennett's method was introduced later which has been preferred among the other model because it provides kinetics parameter such as frequency factor ( $K_0$ ) and rate constant ( $k$ ) along with the activation energy of crystallisation. In non-isothermal method, the value of Avrami exponent,  $n$  is determined from Ozawa equation [119]:

$$\ln[-\ln(1-x)] = n \ln \beta + const \quad \text{Equation 2.24}$$

where  $x$  is crystallisation fraction for the heating rate  $\beta$ .  $n$  values can be calculated from the slope of  $\ln [-\ln(1-x)]$  versus  $\ln \beta$  while crystallisation mechanism,  $m$  can be obtained from the method by Matusita *et al.* [120] .

Numerous attempts has been done to increase the crystallisation temperature of the amorphous alloys [88]. Small addition of alloying elements will not only change the thermal stability of the alloys but also the sequence of crystallisation reactions. Comparison has been done between TiZrCuNiBe HE-BMG and  $Zr_{41.2}Ti_{13.8}Cu_{12.5}Ni_{10}Be_{22.5}$  BMG, it shown that the larger values of activation energy on HE-BMG for  $T_{x1}$  and  $T_{p1}$  which can be due to the multicomponent alloying elements with sluggish diffusion kinetics and high entropy effect. Besides, it is also observed that, the crystallization process of  $Zr_{41.2}Ti_{13.8}Cu_{12.5}Ni_{10}Be_{22.5}$  BMG the crystallization process occurs very rapidly from  $E_a(x) = \sim 170$  kJ/mol at  $x=0.1$  to  $\sim 230$ kJ/mol at  $x=0.9$ . The large difference of average activation energy,  $E_a(x)$  indicates that the alloys has complex crystallisation process compared to HE-BMG [102] as consequence of the complexity of the phase relationship according to phase diagram.

#### 2.4 Alloys design and properties of HEAs with secondary phases

HEAs have been shown to have promising properties for variety of applications. Product design and materials selection are important factor in designing the alloys for specific application. The four core effects of solid solution HEAs as mentioned before provides unique features particularly in physical and mechanical properties, making HEAs attractive in many field. In fact, nanoscale precipitates or secondary phases in solid solution HEAs could further enhance some of the properties of these alloys. Therefore, in the presentation of the properties, composition of the alloys, crystal structure, processes and microstructures are correlated to give a better understanding of the phenomena and mechanism involved the alloys.

### 2.4.1 Mechanical properties

Structural applications require adequate combination of mechanical properties such as hardness, yield strength, elastic modulus, fatigue, creep, nanoindentation, and wear. These properties are important to demonstrate the stabilities and lifetime of the alloys in applications. Since HEAs involve wide composition range and numbers of alloying elements in the alloys system, the mechanical properties (in term of hardness and strength) of these alloys will be different based on a few factors all of which are aspects of the microstructure.

1. Hardness/strength of each phase involve in the alloy
2. Relative volume percent of each phase
3. Morphology and distribution of phases in the alloys

Table 2.3 shows various phases with difference hardness range in HEAs [19]. From the table, it can be seen that, valence compound such as carbide group exhibit the highest hardness values followed by covalent bonding group that have complex phases and subsequently BCC and FCC phases that possess lower hardness values. It is suggested that, the stoichiometry of simple phase HEAs can be modified by including a portion of complex phase to improve their mechanical properties [121-125].

Table 2.3: Example of typical hardness range for each phases in HEAs [19].

Type	Examples	Typical hardness (HV)
Valence compounds	Carbides, borides, silicides	1000-4000
Intermetallic phases with non- simple structures	Laves, $\eta$ , $\sigma$	650-1300
BCC and derivatives	BCC, B2, Heusler	300-700
FCC and derivatives	FCC, L12, L10	100-300

Although published works have proven that single phase HEAs has shown a good mechanical properties compared to conventional metallic systems [63, 126], there is also reported work that reveals that the structures consists of secondary phase such as intermetallic compound can improve the properties of single phase HEAs. For example, AlCoCrFeNi<sub>2.1</sub> HEA has demonstrated a good combination of strength (tensile) and ductility at high temperature that also can resist phase changes at high temperature. It has been named as high temperature-eutectic high entropy because the use of eutectic concept in the HEA design that combining the advantages of both HEAs and eutectic alloys and removes the disadvantages of these two alloys at the same time. Figure 2.10 shows SEM micrographs of the alloys that displays a lamellar dual phase structure compose of two different phases which are FCC and B2 phase as proved by XRD traces in Figure 2.11(a) while DSC data shows in Figure 2.11(b) shows a single peak at 1300°C both in heating and cooling process. However, DSC data alone are not enough to claim these alloys as eutectic HEAs (EHEAs). The addition of data from thermodynamic calculation based on phase diagram (CALPHAD), will make this research more reliable and establish. In term of mechanical properties, the presence of both FCC/B2 phases offer a balance of high fracture strength (944MPa) and high ductility (25.6%) for engineering stress-strain curve and 1186MPa and 22.8% respectively when it converted to true stress and strain curve as shown in Figure 2.12. Besides, the properties can be retained up to 600°C before it started to decrease due to presence of another complex phases that increase the brittleness and reduce the elongation of the alloy. The large strain hardening of this alloys is attributed from homogeneous alternating of soft FCC phase with hard bcc phase along with the B2 nanoprecipitate that hinder the movement of dislocation in the alloys [127].

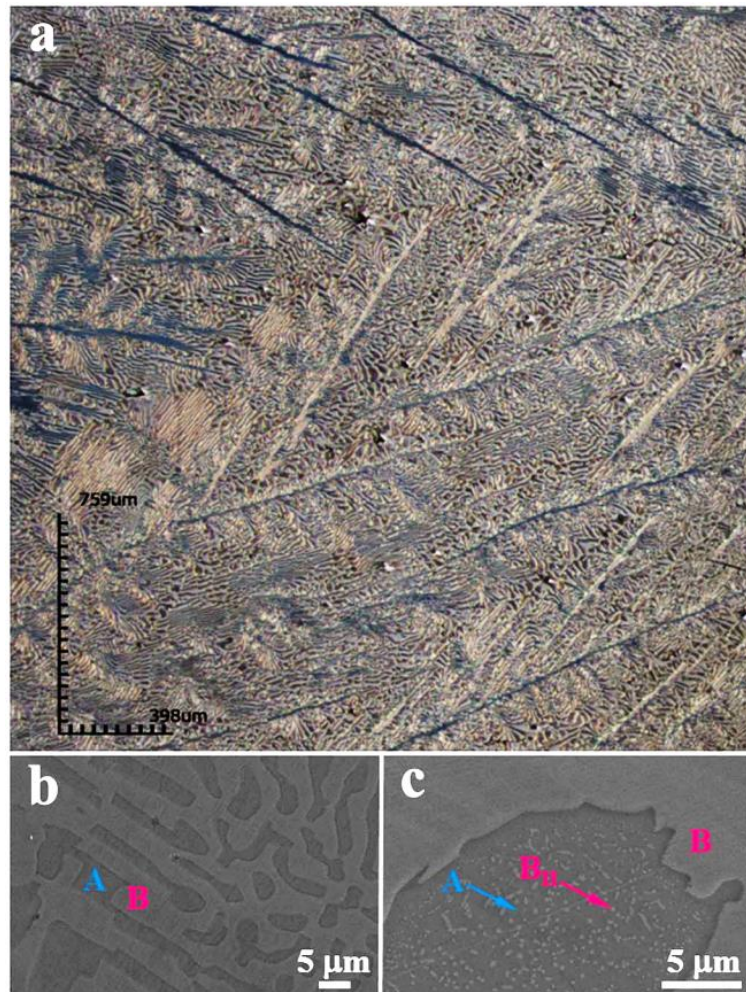


Figure 2.10: Laser scanning Confocal Microscope (LSCM) micrograph shows lamellar structure of  $\text{AlCoCrFeNi}_{2.1}$  HEA in low magnification and (b and c) SEM micrograph where A and B symbols indicate two different phases in the structure while  $B_{II}$  shows nanoprecipitate of B2 phase within the FCC phases [127].

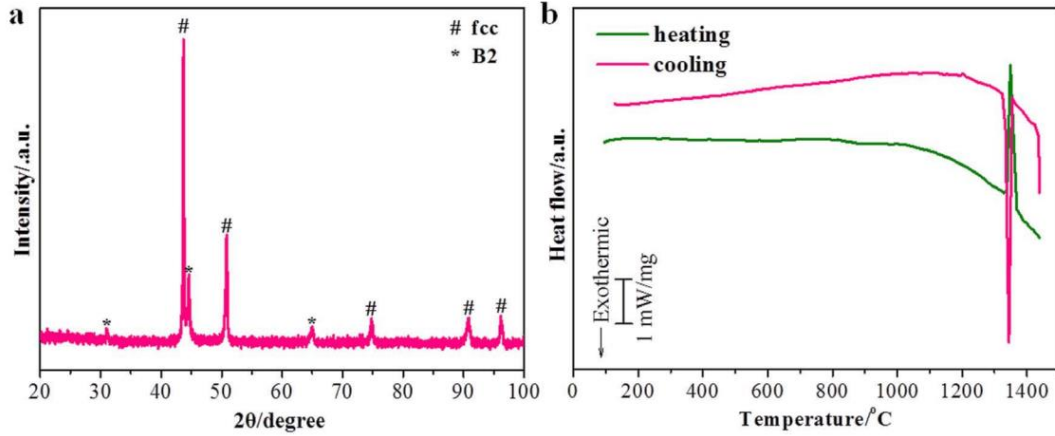


Figure 2.11: (a) XRD patterns of as-cast AlCoCrFeNi<sub>2.1</sub> HEA alloys and (b) DSC curve of the alloy in both heating and cooling process [127].

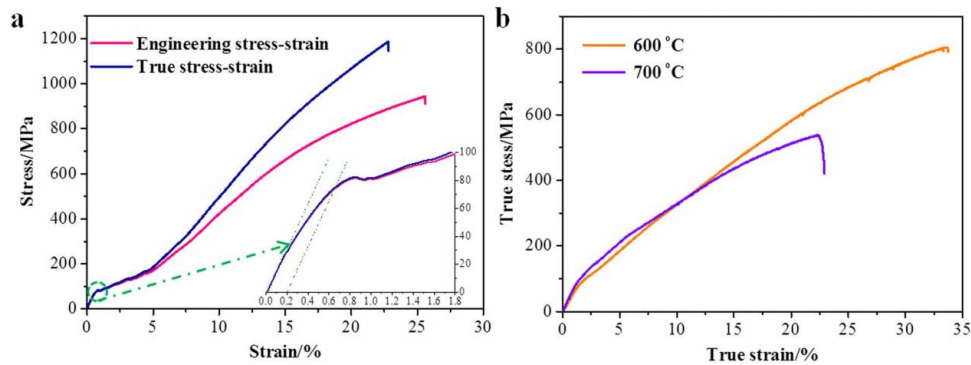


Figure 2.12: Tensile stress strain curve of AlCoCrFeNi<sub>2.1</sub> HEA at a) room temperature and b) at 600°C and 700°C, respectively [127].

Feng and his colleagues [128] subsequent improved the eutectic HEA studies by considering the existing binary alloys system using CALPHAD data on their communication. The strategy is by identifying the pseudo binary phase diagram with single phase solid solution that can form eutectic structure with a single element. The binary phase diagram has been successfully employed in predicting phases in HEAs in some reported HEA studies [55, 129, 130]. It has been found that Fe, Co, Cr and Ni can form eutectic structure with Nb (Fe-Nb [131], Cr-Nb [132], Co-Nb [133], Ni-Nb [134]). Therefore, a pseudo-binary phase diagram of (CoCrFeNi)-Nb has been constructed from Thermo-Calc software using Ni-based database as in Figure 2.13

which clearly shows formation of different phases with increasing Nb content. The morphology of  $\text{CoCrFeNiNb}_x$  in Figure 2.14 shows difference microstructure that indicates hypo-eutectic, eutectic and hyper-eutectic as Nb is varied from 0 to 0.8 at.%. The microstructures therefore influence the mechanical properties of the alloys where compressive ultimate strength increases from 2025 MPa to 2505 MPa when the Nb content  $x$  increases from 0.25 to 0.8, while the compressive fracture strain decreases from 38.8% to 12.8% due to lack of volume fraction of soft FCC phase. The  $\text{CoCrFeNiNb}_{0.25}$  alloy has optimum balance of strength and ductility, with high fracture strength and strain of 2024.6 MPa and 38.8%, respectively. Meanwhile, the hardness of these alloys increases with the increase of Nb content, with the highest hardness value of 713 HV at  $x=0.8$  as can be seen in Figure 2.16.

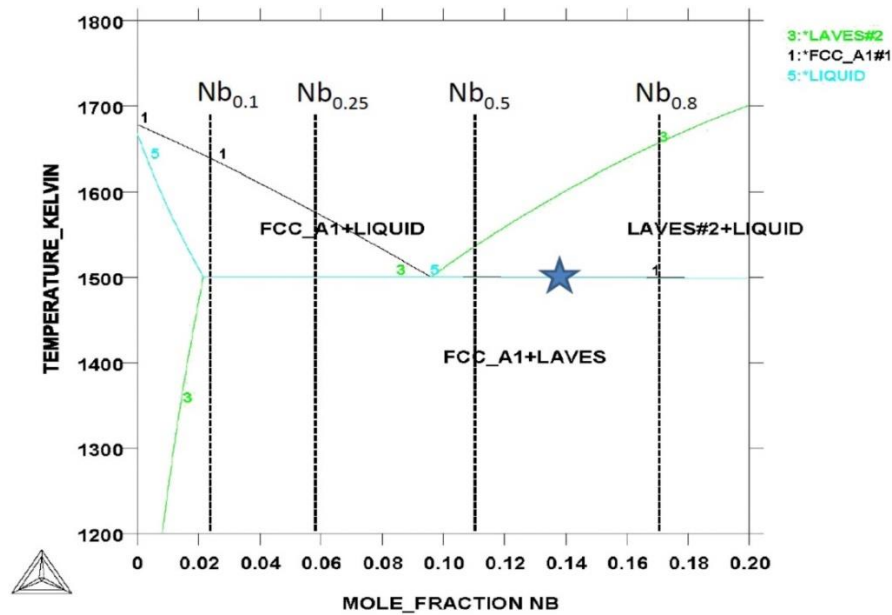


Figure 2.13: The pseudo binary phase diagram of  $\text{CoCrFeNiNb}_x$  alloys developed by Thermo-calc software.

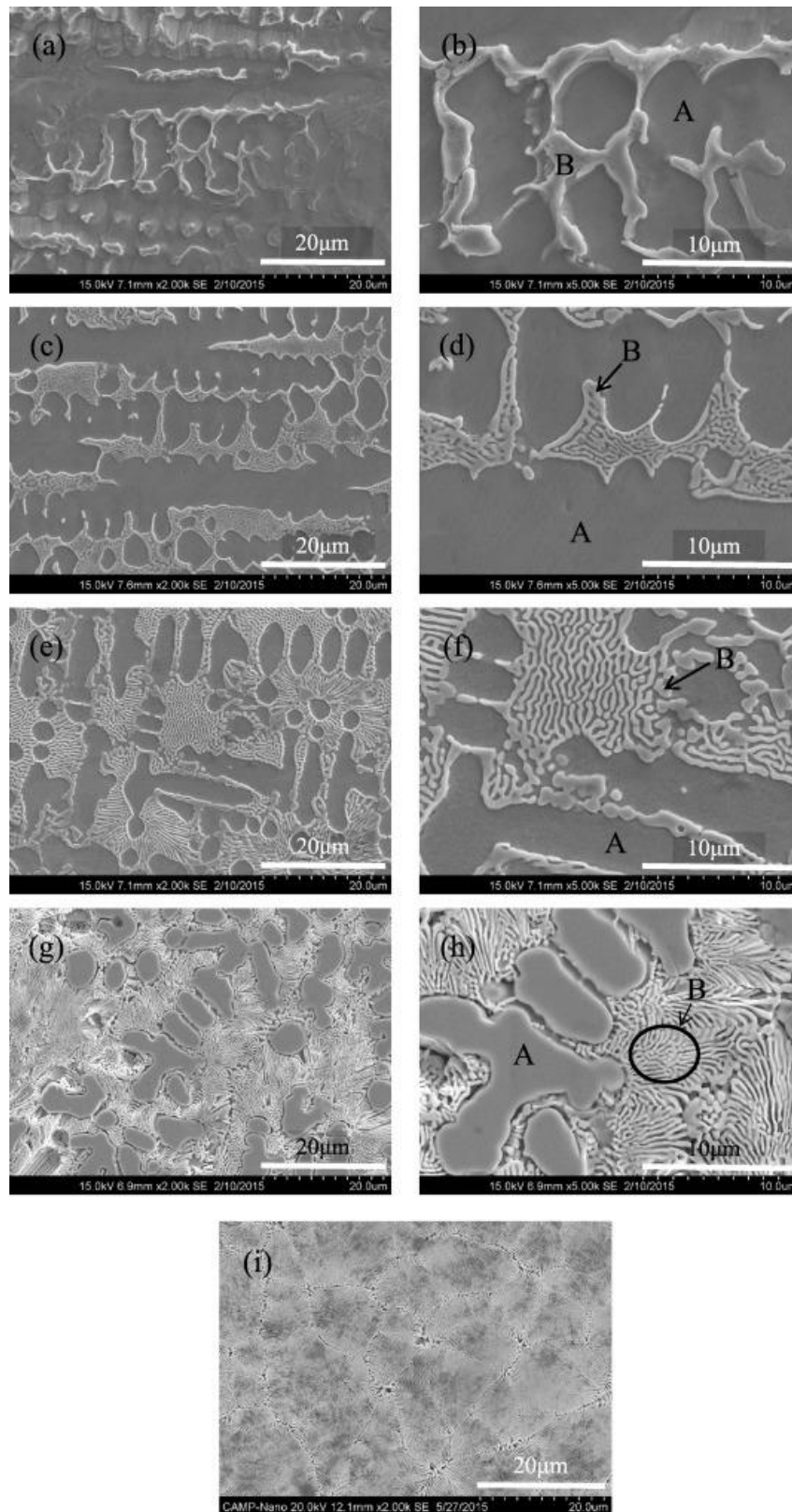


Figure 2.14 SEM images of  $\text{CoCrFeNiNb}_x$  alloys; (a and b)  $x = 0.1$  shows divorced eutectic (c and d)  $x = 0.25$  shows hypo-eutectic; (e and f)  $x = 0.5$ , hypo-eutectic; (g and h)  $x = 0.8$ , hyper-eutectic and (i)  $x = 0.65$ , eutectic. The proeutectic phases are symbolled as A while the eutectic is marked as B [128].

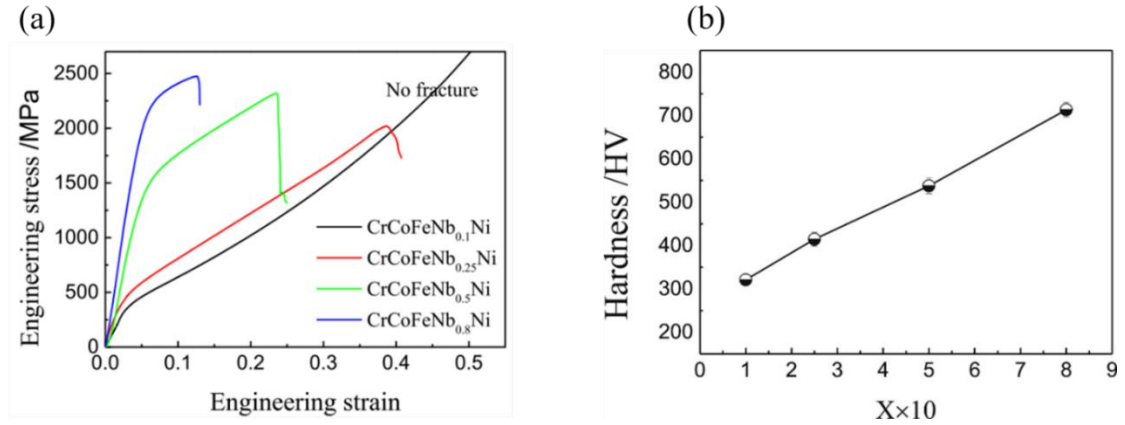


Figure 2.15: (a) Engineering stress-strain curve and (b) hardness of CoCrFeNiNb<sub>x</sub> EHEA with increasing Nb content [128].

Ultrafine grain of eutectic lamellar structured was discovered by Wani *et al.* that show promising strength-ductility combination having ultimate tensile strength of ~1200MPa and 12% elongation due to the presence of alternating bands consists of soft L1<sub>2</sub> and hard B2 phases in as-cast AlCoCrFeNi<sub>12.1</sub> [135]. The phase stability of alloys was then investigated by cold rolling up to 90% thickness reduction and annealing from 800°C to 1200°C [136]. The significant transformation can be seen in L1 phase after cold rolling, whilst B2 phase maintained the ordered structure. The mechanical properties of this alloy were studied by nanoindentation hardness mapping at specific lamellar structured area to see variation of hardness within the mapping area as in Figure 2.16. Clear hard and soft region can be seen in the hardness map and has been analysed carefully in the histogram as depicted in Figure 2.16 (c). The distribution of hardness values between the two phases in the histogram shows that the strain concentration to the softer L1<sub>2</sub> phase and the development of various shear band in the alloys.

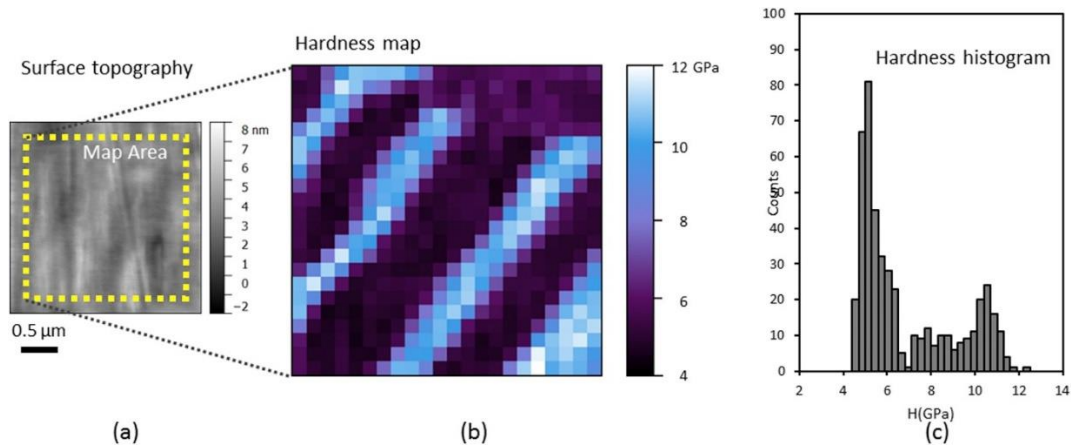


Figure 2.16 (a) Surface topography of as-cast AlCoCrFeNi<sub>2.1</sub> EHEA taken before nanoindentation mapping (b) hardness maps shows clear lamellar structure and (c) Histogram from the hardness values of the alloys.

Meanwhile, interesting studies by Li *et al.* has shown a deformation behaviour in dual phase HEA that can overcome strength and ductility trade-off [137]. In the paper, the multicomponent alloys were used to design a metastable alloy system of Fe<sub>80-x</sub> Mn<sub>x</sub>CoCr which owe good mechanical properties on the basis of two work hardening system that are, 1) dual-phase microstructure interface work hardening and 2) transformation-induced hardening. In contrast to general usage of HEA method, FeMnCoCr was designed to achieve a metastable condition of the alloy. So as to lead phase transformation during deformation process, hot rolling to 50% at 900°C and then cold rolling up to 60% reduction has been done. Subsequently, after 2h 1200°C solid solution treatment, the grain of the alloy has been refined to a satisfied scale. This can be explained by stacking fault act as nuclei for the formation of hcp phase which cause nano-size reinforced hcp phase generated, at meantime the increasing phase boundary density turn to create more obstacles for dislocation slip and contributing to another work hardening system. To prove, this the sample was examined with XRD ECCI and EBSD as in Figure 2.17.

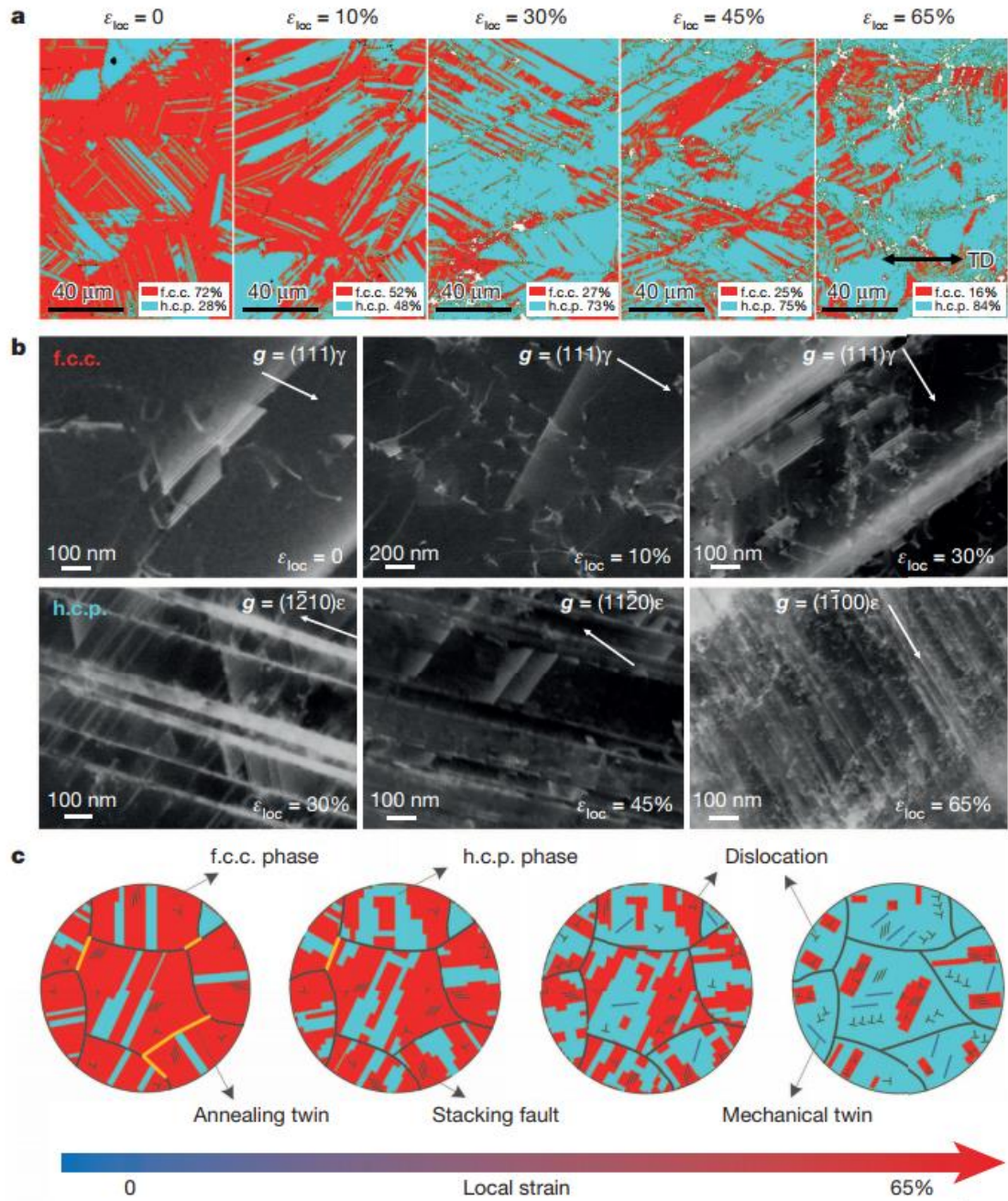


Figure 2.17: Mechanism of deformation in the TRIP-DP-HEA with increasing tensile deformation at room temperature. a), EBSD phase maps illustrating the deformation-induced martensitic transformation as a function of deformation where  $\epsilon_{loc}$  is the local strain and TD is the tensile direction. b), ECCI analyses presenting the evolution of defect substructures in the FCC. and HCP. phases where  $g$  is the diffraction vector,  $\gamma$  is the FCC phase and  $\epsilon$  is the HCP. phase. c), Schematic drawings demonstrating the arrangement of microprocesses in the TRIP-DP-HEA.

By test sample with different Mn content, the volume of hcp phase and FCC phase changing dramatically which indicate Mn is response for tuning phase stability to activate specific displacing transformation mechanism, transformation-induced plasticity (TRIP) and twinning-induced plasticity (TWIP). The best composition was confirmed by energy dispersive spectroscopy and atom probe tomography to show that all elements are distributed homogeneously which indicate both hcp and FCC phase benefit from solid solution strengthening.

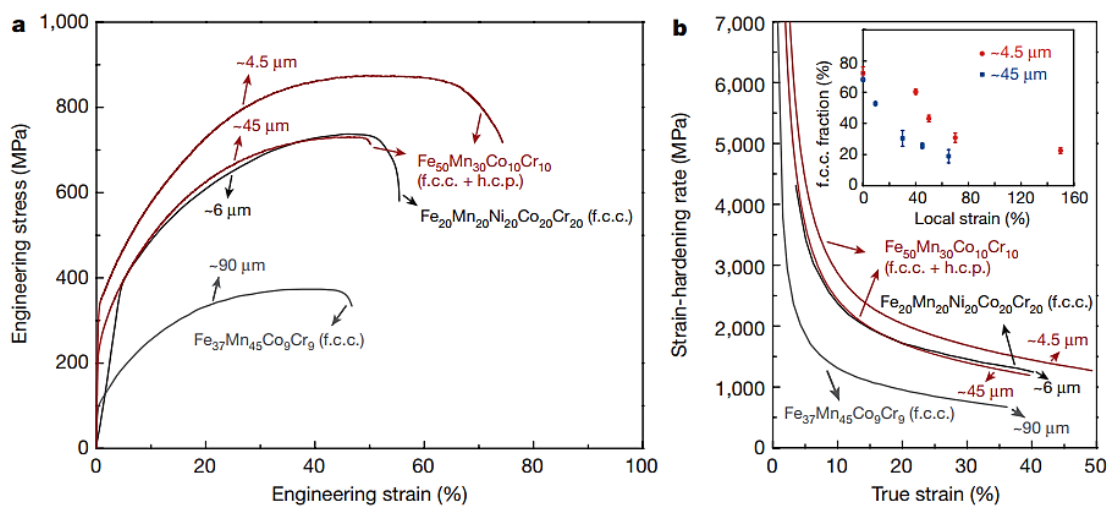


Figure 2.18: Mechanical properties TRIP-DP-HEAs compared to various single-phase HEAs [137]. a) The engineering stress-strain curve of DP- HEAs with respect to grain sizes, b) Strain-hardening response where the inset shows how the stability of the FCC. phase was improved upon grain refinement to increase the strain-hardening ability.

The observed stacking faults in the undeformed HEA are initial faults that do not sufficiently coalesce to form the thermally induced hcp phase but are likely to act as phase formation nuclei when subjected to externally applied loads. During deformation process, the phase transformation mechanism is working as primary activated module. Both dislocation plasticity and martensitic transformation plasticity are activated at this level. But with increasing strain the dislocation activity in FCC phases become more and more important. However, in late deformation stage the

mechanism induced in HCP phase started to play a more important role. Not only because most FCC phase transform to HCP phase but also because an increase of density of nano-twins and stacking faults in HCP. This contribute through dynamic Hall-Petch effect to strain hardening. So in late stage multiple deform mechanism is working in HCP phase (dislocation slip, twinning and the formation of stacking faults). This mechanism has been proved by compression test in Figure 2.18 (a) which show the mechanical response of DP-HEA with difference grain size where, as-homogenised shows a coarser grain size (45 $\mu$ m) which exhibit lower strength and ductility compared to recrystallized state (4.5 $\mu$ m). The graph also shows that the mechanical properties of DP-HEA is also striking before heat treatment as compared to single phase FCC Fe<sub>20</sub>Mn<sub>20</sub>Ni<sub>20</sub>Co<sub>20</sub>Cr<sub>20</sub> HEA while Figure 2.18 (b) shows strain hardening that occurred upon gran refinement.

## 2.5 Summary of literature review

Despite extensive research involving High Entropy Alloys (HEAs) and Bulk Metallic Glasses (BMGs) individually, little is reported about the formation of High Entropy Bulk Metallic Glasses (HE-BMG) especially the thermal stability and crystallisation kinetics of this alloys. Besides, the literature also merely highlighted a study on formation of High entropy alloys based on single solid solution with limited studies on the formation of secondary phases that can improve the properties of the alloys. Therefore, the knowledge gap and some areas that require further investigation are summarised as follow:

- Study on kinetics of phase transformation in conventional metallic glasses have been vastly reported. Amorphous HEAs with sluggish diffusion effect will give difference viewpoint on the crystallisation kinetics and metastability of the alloys. However, limited research has been published to understand the transformation kinetics of this alloys from thermodynamics viewpoint. Therefore, investigation on glass forming ability, thermal properties and crystallisation mechanism of the amorphous HEAs need to be established.
- HEAs have been reported as promising alloys for various applications. The majority of previous study are favour single-phase disordered solid solution as it can avoid precipitation of complex phases that can induce brittleness at high temperature. However, single phase HEAs can only be good to one property either good strength or excellent ductility. Therefore, design of new HEA composition with secondary phases with control of morphology can provide a strength-ductility balanced in the

alloys. Even though research on finding a new HEA composition to overcome strength-ductility trade-off has been growing recently, limited research has been published to understand the metastability of HEAs with the addition of secondary element into the base alloys. Therefore, a new design of HEAs with control morphology that can tune the properties of HEAs is needed along with the understanding of metastability on the undercooling state of the alloy.

- A comprehensive study on the change of mechanical properties on phase formation is required to understand the relationship of the structure-properties in the alloy. Besides, knowledge of the deformation behaviour is useful to reveal the failure mechanism in the designed alloys.

## **CHAPTER 3**

### **METHODOLOGY**

#### **3.1 Introduction**

This chapter emphasises the experimental techniques used in the research project in terms of sample preparation, characterisations, testing and analytical procedures. In this project, High Entropy Alloys (HEAs) were prepared using arc melting equipped with suction casting. In addition, melt spinning was also used for higher cooling rate. In the first part of this project, differential scanning calorimetry (DSC) was used as a means to assess the annealing process for crystallization kinetics studies in TiZrHfNiCu HE-BMGs. Next, a careful alloy design process was carried out based on systematic calculation of the thermodynamic and electronic parameters of candidate HEAs to obtain the lamellar structured high entropy alloys. The HEA composition of FeCoNi(Al<sub>0.1</sub>Si<sub>0.1</sub>) was chosen for modification with boron (replacing aluminium). The Rietveld refinement method was used to determine the volume fraction of each phases present from X-ray diffraction data. The designed alloys were then mechanically tested using various instruments to investigate the effect of phase changes upon boron addition on the mechanical properties of the alloys.

#### **3.2 Materials preparation**

##### **3.2.1 Arc melting and casting**

High entropy alloys were prepared using a MAM1 arc melter Edmund Bühler GmbH machine by melting bulk high purity elements (99.99% purity). Beforehand, the elements were cleaned with grinding paper to remove an oxidized surface or dirt that can be observed on the elements. The elements were then weighed using Precisa Series 320 XB mass balance according to the calculated masses by atomic percentage of the

constituent elements. The difference between calculated and measured masses of each element was ensured to be below 0.01g. The weighed elements were cleaned ultrasonically using isopropanol for 10 minutes in the bath of an ultrasonic cleaning machine containing clean water. The elements were dried before placed into the crucibles of the copper melting hearth with lower melting temperature elements placed underneath the higher temperature elements to optimize the initial melting of the mixture. A Ti-getter was placed in the middle of the crucible before the chamber was evacuated to 0.1 torr. Once the evacuation was achieved, the chamber was backfilled with argon to 0.3 bar and evacuated back to 0.1 torr. This was repeated 3 times before the chamber was further evacuated to the optimum vacuum below  $6.0 \times 10^{-5}$  torr. After that, the chamber was filled with argon to 0.7 bar and water was supplied through the small pipe into the copper hearth for cooling purposes. The melting procedure was started by melting the getter to remove residual oxygen within the chamber followed by melting the contents of each crucible for less than 10 seconds. Each ingot in the different crucibles was mixed in a single crucible and melted again forming an ingot. The ingot was flipped and melted again at least 5 times to ensure homogeneity. The chamber was de-evacuated and the ingot was removed. The ingot was weighed again to ensure the total loss is less than 0.1%. The image of MAM1 arc melting machine and the components in melting mode can be found in Figure 3.1(a) while schematic of melting process, the melting hearth component that attached to the arc melting machine, and sample of the ingot for 5g and 8g can be seen in Figure 3.1 (b),(c),(d) and (e) respectively.

Before the casting process, the ingot was cleaned again ultrasonically in isopropanol. The melting chamber in the arc melter was changed to the casting chamber (see figure 3.2 (a)) where moulds of different size can be placed in the middle of the hearth (see

figure 3.2 (d)). The procedure of evacuation was the same as for the melting process, except the tube of the casting needed to be opened throughout the evacuation process. This has been illustrated as in Figure 3.2 (b). Prior to final evacuation, the casting tube was closed at around  $3.5 \times 10^{-1}$  bar for the casting pressure. The chamber was evacuated again until  $6 \times 10^{-5}$  torr was reached by the aid of a turbo pump to accelerate the evacuation. The water was supplied and left for 3 minutes to ensure the chamber was cooled enough to obtain maximum cooling rate. The vacuum chamber was closed before the chamber was evacuated to 0.7 bar. The getter was melted first and the torch was then brought to the middle of the chamber where the mould was placed. The fully melted alloys were then suction casted once the casting chamber was opened. Finally, the cast was removed from the mould and was cleaned before it was sectioned using a minitom machine equipped with a silicon oxide blade for characterization and testing.

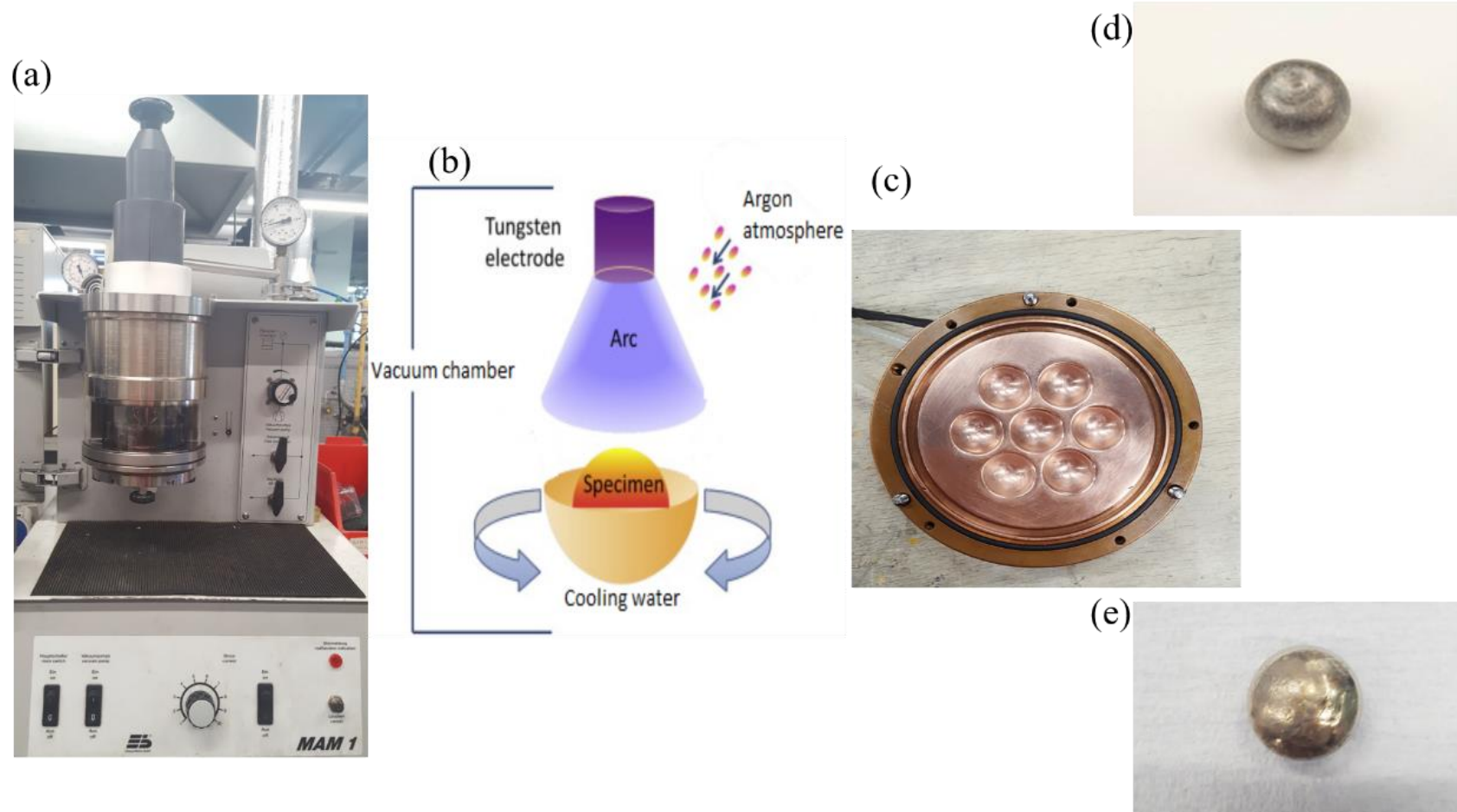


Figure 3.1: (a) MAM1 arc melting machine, (b) schematic of melting process (c) melting hearth attached to the arc melting machine, (d and e) ingot of 5g and 8g respectively.

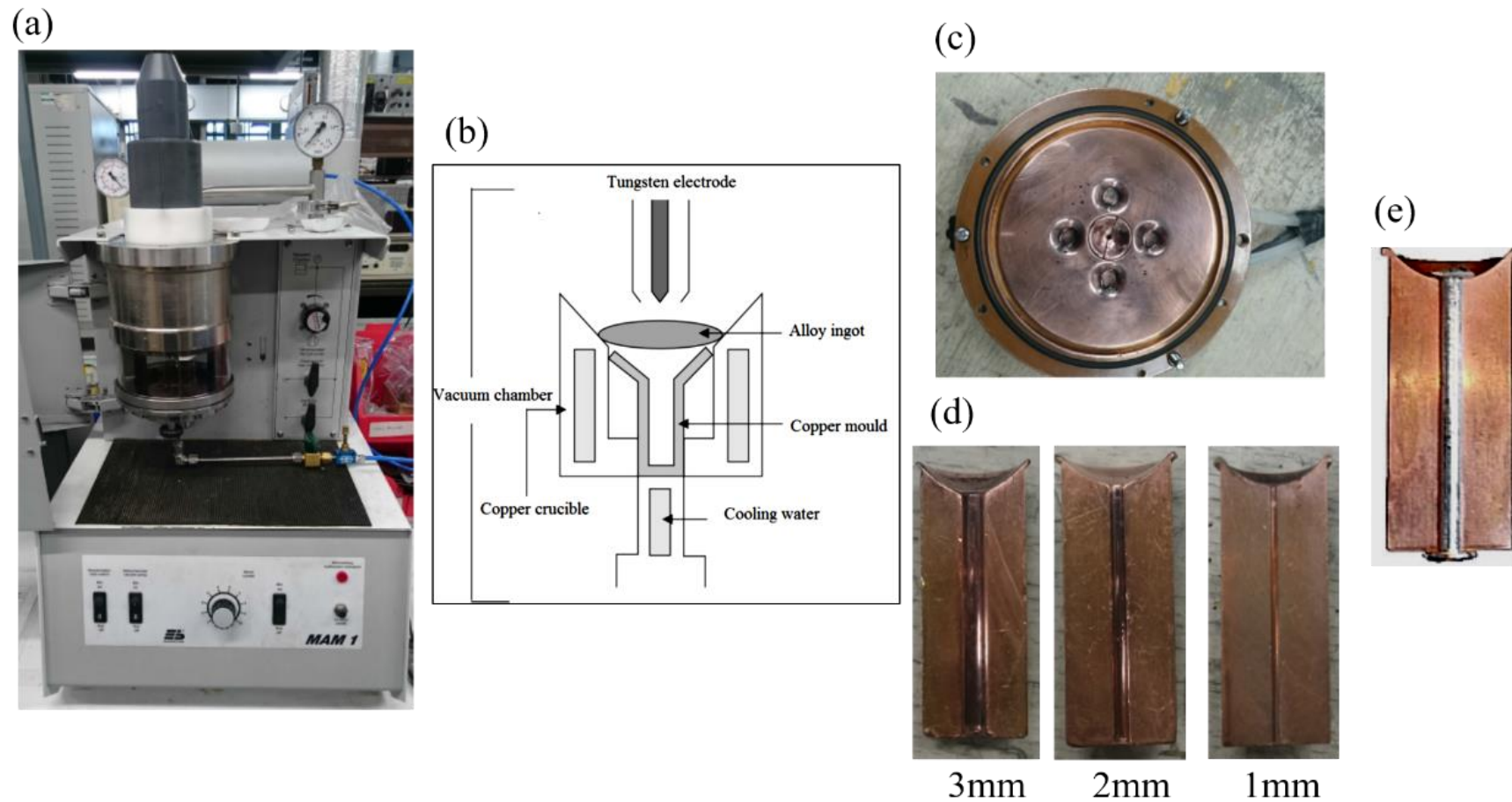


Figure 3.2: (a) MAM1 casting configuration, (b) schematic of casting process (c) casting hearth attached to the arc melting machine, (d) different size of mould used (e) sample after casting.

### 3.2.2 Melt spinning

Ribbon samples were produced by a melt spinner with a high cooling rate as in Figure 3.3. Ingot produced from the melting process as in Figure 3.1 (d and e) was used to produce ribbon samples. It was done by loading the ingot into a cleaned quartz crucible tube with 1 mm diameter hole at the end. The tube was put into an induction heater coil and connected to an argon supply pipe. A copper wheel, used for rapid cooling was cleaned with isopropanol and the chamber was sealed. The chamber was placed under vacuum using roughing and diffusion pumps. The roughing pump was opened until chamber pressure reached  $<1.5 \times 10^{-1}$  Pa before the backing pump was opened. The roughing pump and diffusion pump were connected in series at this stage. This is necessary for the roughing pump to support the diffusion pump. When the chamber pressure reached  $6.5 \times 10^{-5}$  Pa, the chamber was backfilled with the argon three times. After that, the argon was flushed through the argon supply line that connected to the glass tube. The flow of the gas was set to control the flow that will be sent to the top of the glass tube at the melt discharge stage. The water system was switched on and left for a few minutes to obtain the optimum quench rate condition. The voltage and hence the speed of the wheel was set up after turning the generator on. Then, the solenoid valve was turned on to heat the induction coil and subsequently melt the alloy in the quartz crucible. When the alloy melted, an over-pressure of 40 kPa was applied ejecting the melt onto the rotating Cu wheel with a surface velocity of 20m/s to 40m/s. The ribbon sample was collected and cleaned with isopropanol before characterisation. The size of the ribbon varied depending on the speed of the rotating wheel as can be seen in the figure below.

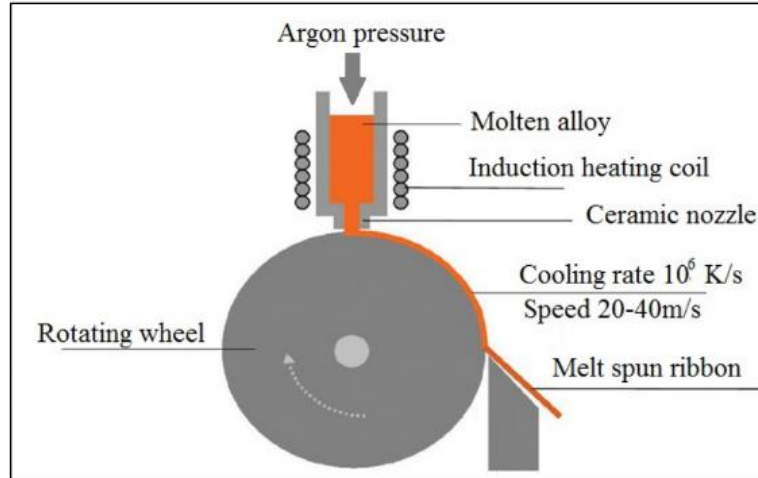
(a)



(b)



(c)



(d)



(e)



Figure 3.3: Figure (a) Melt spinning machine, (b) molten alloy inside the chamber during spinning process, (c) schematic process of melt spinning process, (d and e) melt spun ribbon at 20m/s and 40m/s speed respectively.

### 3.3 Annealing process

Annealing was carried out using DSC machine (Perkin Elmer Diamond DSC) under a high-purity argon atmosphere to determine kinetics of transformation such as the mechanism of nucleation and growth in glassy HE-BMG and to determine pertinent information such as incubation time, activation energy and crystallization fraction of the alloy. In this project, two types of annealing conditions were carried out; isothermal and non-isothermal annealing.

In isothermal annealing, the setup parameters were described as in Figure 3.4(a) where the sample was heated up rapidly at 100 K/min to a super-cooled liquid region (between  $T_g$  and  $T_x$ ) (684 to 704 K) below  $T_{x1}$  and holding for certain period of time until the alloy was fully crystallised.

On the other hand, in non-isothermal annealing or direct continuous heating, the process was performed at different heating rates ranging from 10 K/min to 80 K/min until before melting temperature to determine glass transition and crystallization temperature at different heating rate. The onset of each curve was defined as the tangent intersection of the DSC signal above and below the initial change in the baseline slope.

Before the experiment was carried out, an as cast sample of 1.5mm diameter TiZrHfNiCu HEBMG alloys was mechanically cut into ~20 mg each to avoid influence of sample mass and sample size during the experiment. The sample was then ground using 1200 grinding paper to remove surface oxidation prior to experiments. Finally, the disk samples were washed in ethanol in an ultrasonic cleaning machine. The sample was then weighted and recorded before it was put into the aluminium pan and encapsulated it with the aluminium lid. The sample was placed into the DSC machine with the other empty aluminium pan for reference. The specific heat capacity

measurements were performed by step-scan method and the data were calculated and corrected based on the specific heat calculations using a standard sample (sapphire). The parameter was set up and the experimental data was recorded using Perkin Elmer software.

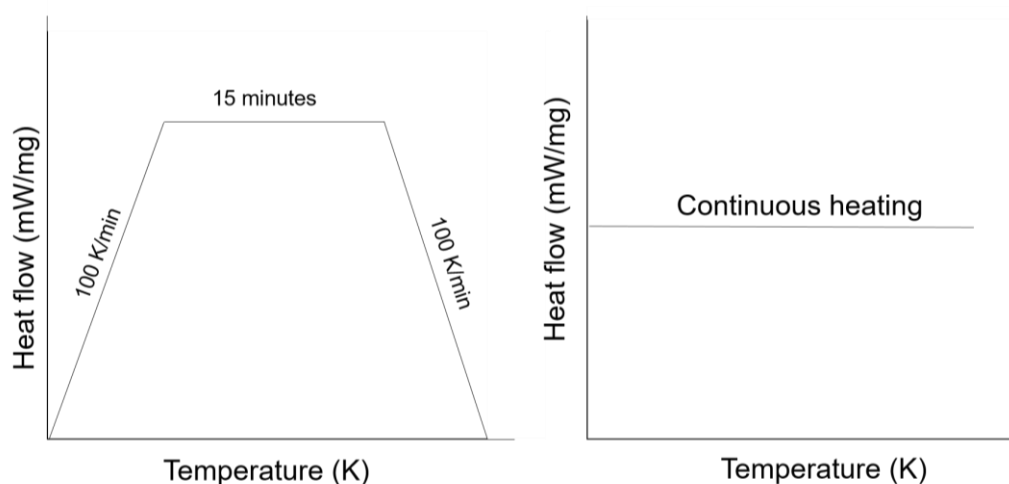


Figure 3.4: Parameter profile for (a) isothermal annealing (b) non-isothermal annealing process.

## 3.4 Characterisation techniques

### 3.4.1 Phase analysis

#### 3.4.1.1 X-Ray diffraction (XRD)

XRD analysis was performed using Siemens D5000 XRD machine with sample changer using  $\text{CuK}\alpha$  source in the range of  $20^\circ$  to  $90^\circ$  with a step size of  $0.01^\circ$  and scan rate of  $0.1^\circ/\text{min}$ . The sample was ground and polished before it was put it in the sample holder to avoid effect of crystal orientation during the experiment. During the experiment, the samples were rotated continuously to maximize the x-ray exposure

around the samples area. The peaks present were analysed using ICDD PDF4+ database and EVA software.

#### **3.4.1.2 Determination of Phase Fraction by Rietveld refinement**

Phase fraction in HEAs can be obtained by analysing the XRD peaks with accurate profile fitting by the Rietveld refinement technique using GSAS software [138] with EXPGUI interface [139]. The measured profile was refined to match the theoretical profile using the least squares method. The reliability of the refinement was assessed by the difference profile and goodness of fit parameters. Basically, the most common parameters that can be refined are:

1. Scale factor

To make sure that the observed and calculated phase diagram are on the equivalent scale. It is usually refined in each least square cycle.

2. Background

The background of the histogram is fitted using several mathematical functions with number of terms defined by the user (usually between 3 to 12) depending on the quality of fitting.

3. Lattice parameter

Lattice parameters are refined after the scale factor and background achieved convergence.

4.  $2\theta$  zero

The  $2\theta$  zero is only refined for the diffraction data that use transmission geometry. In Siemens D5000 instrument, Bragg-Brentano geometry is used where sample shifted and transparency parameters are refined instead.

5. Profile parameter (shape and peak function)

The factors that influence the peak profiles of the diffraction data are the sample and instrument. Typically, pseudo-Voigt function is used to model the peak profile of the XRD pattern which comprises of a fractional influence of Gaussian and Lorentzian component in both functions. The Full Width Half Maximum (FWHM) parameters are refined where the peak width is give as a function of diffraction angle,  $\theta$

#### 6. Atomic position

It is a position in fractional coordinates (x,y,z) of each atom in the unit cell

#### 7. Thermal parameters (Atomic displacement parameters)

These are a measure of vibrational frequency of each atom at the temperature of the experiment.

### **3.4.2 Thermal analysis**

#### **3.4.2.1 Differential Scanning Calorimetric (DSC)**

Glass transition temperature ( $T_g$ ) and crystallization temperature ( $T_x$ ) of the sample were assessed using a Perkin Elmer Diamond DSC at different heating rates from 20 to 80 °C/min under argon condition. The machine was calibrated beforehand to ensure the reliability of the data by using a zinc standard specimen. About ~20 mg samples were cut and weighed, and it was put in aluminium pans while the other empty alumina pan was used as reference. DSC will measure amount of energy input required to keep both pans at the same temperature. Another run with empty pan in both side was conducted for a baseline to get the real signal by subtracting it with the data from the sample. The onset and peak of each significant signal was taken for further analysis.

### **3.4.2.2 Differential Thermal Analysis (DTA)**

Perkin-Elmer DTA-7 machine was used for a higher temperature analysis such as melting temperature,  $T_m$  and liquidus temperature,  $T_l$ . Approximately 20 mg samples were weighed and placed in aluminum pans and heated at 20°C/min. Similar to DSC, DTA measures the difference in the amount of heat (heat flow) required to increase the temperature of the sample and reference under the same conditions. Therefore, any phase changes or thermal processes occurring in the alloy will cause a difference in temperature between the sample and the reference.

### **3.4.3 Microscopy**

#### **3.4.3.1 Scanning Electron Microscopy (SEM)**

The fracture morphology and phase difference in HEAs can be analysed using SEM (Siemens FEI Inspect F50) in secondary electron (SE) and backscattered electron (BSE) modes. Before the experiment was carried out, the samples were cleaned with acetone using an ultrasonic machine. The samples were then cold mounted using epoxy resin and hardener and cure for at least 6 hours before grinding and polishing until the samples had a mirror-like finish. During the experiment, the accelerating electron voltage of 15 to 20 kV was used depends on the clarity of the image required. Energy Dispersive X-ray Spectrometry (EDS) also carried out for qualitative (image mapping) and quantitative compositional (element composition) analysis.

#### **3.4.3.2 Transmission Electron Microscopy (TEM)**

The detailed microstructures of the alloys were examined by high resolution transmission electron microscope (TEM, Philips EM420). Sample preparation was carried out by electropolishing. This process was done by immersing the ~10µm thickness sample disc in 90% of ethanol and 10% of perchloric acid as electrolyte at

flow rate of  $12\text{m}^3/\text{s}$  at  $60\text{V}$ . This process took at least 10 minutes. Then the sample was looked at under the optical microscope to observe the existence of a small thin hole at the middle of the sample. After that, the sample was inserted into the TEM machine using double tilt specimen holder. The magnification was set up to  $>23,000\times$  and was operated at acceleration voltage of  $200\text{ kV}$ . The thin area was then identified and focused on. Before bright field images were taken, it is necessary to get the diffraction pattern of the sample by inserting a diffraction aperture at the magnification  $>6000$ . The bright field image was then taken to see the features by removing the diffraction aperture and inserting the objective aperture. Micrographs taken for further analysis.

### **3.5 Mechanical Testing**

#### **3.5.1 Compression testing**

Mechanical properties such as yield strength, Young's modulus, fracture strength and plastic strain can be evaluated using compression testing. Sample preparation was quite easy since the cast alloys are in cylindrical shape. Therefore, the sample needs to be flat and parallel in both side and the aspect ratio should be close to 2:1 [140].

The experiment was done at room temperature using a Zwick compression machine at a strain rate of  $5.0\times 10^{-4}\text{s}^{-1}$ . The experiment was carried out 3 times on different samples for each composition to ensure the results were consistent. Two platens of boron nitride (BN) were used to compress the sample. To reduce the friction between the sample and platens, the graphite grease was put on the sample before testing.

## 3.5.2 Hardness testing

### 3.5.2.1 Micro indentation tests

The cold mounted samples were ground with 2500 and 4000 grades SiC papers and polished with alcohol diamond suspension before hardness testing was carried out. A microhardness tester (Akashi Corporation Sagami Plant, model HM-101) with a load of 1 kg and dwell time of 15 s was used to perform hardness test. During the test, a square based pyramidal shape indenter made from hardened steel was applied to a sample at a given load and time and the resultant indentation diagonal area was then measured using a microscope. The result displayed on the screen was then converted to hardness value  $H_v$  according to the following equation:

$$H_v = \frac{1.854F}{d^2} \quad \text{Equation 3.1}$$

where  $F$  is kilogram-force (kgf) which is set at 1 kg in the experiment,  $d$  is the diagonal length of the indent in mm. Therefore the units are  $\text{kgf}\cdot\text{mm}^{-2}$  which also can be expressed HV1. The experiment was carried out at least 10 times for each sample at different locations to obtain accurate hardness results. However, micro indentation will give an average hardness value over the large area across the grain. Therefore, another technique is required to get a localised hardness value for a specified grain.

### 3.5.2.2 Nano indentation tests

A TI Premier Nanoindentation tester (equipped with scanning probe microscope) fitted with a Berkovich diamond tips was used to measure the local hardness and modulus in lamellar structure high entropy alloys consists of primary bcc/b2 phase, and lamellar structure of FCC and  $\text{Fe}_2\text{B}$  phases.

The ground and polished cold mounted samples with height less than 10 mm were placed into an automated sample platform in an acoustic chamber after cleaning

with isopropanol and compressed air. Before that, the indenter tip was calibrated using fused quartz at different loads until good fit was achieved with the expected load response as calculated for the tip area by the triboscope software. Meanwhile, the X-Y stage and optics were calibrated using a polycarbonate sample. Parameter profiles of the indentation such as loading time and indent test position were set up before the test was carried out. The 50  $\mu\text{m}$  sample area was first scanned by bringing the indenter tip in contact with the sample surface. Later, 3 x 3 indent arrays with 10  $\mu\text{m}$  indent separations were probed at load of 100  $\mu\text{N}$  at the edge of the 50  $\mu\text{m}$  sample scan area for a 10 sec dwell time. Illustration of the indentation array can be found in Figure 3.5. The result was then evaluated and the sample was taken for image analysis to specify the hardness at different region. The value of hardness and Young's modulus of each phase was evaluated based on the coordinate value taken from the nanoindentation measurement.

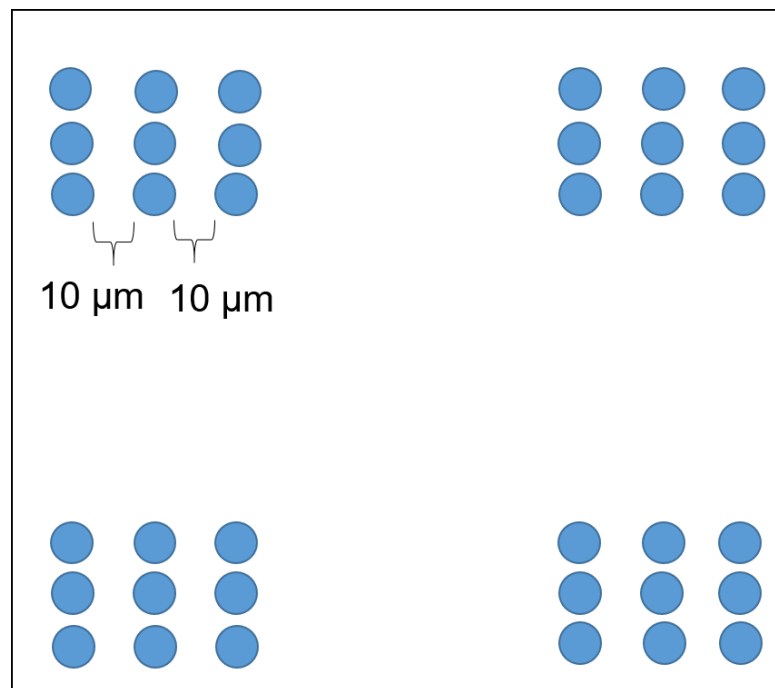


Figure 3.5: Illustration for indentation array region in 50  $\mu\text{m}$  sample area.

## CHAPTER 4

### Crystallisation Kinetics and Thermal Stability of TiZrHfNiCu High Entropy Bulk Metallic Glass by Differential Scanning Calorimetry (DSC)

#### 4.1 Abstract

TiZrHfNiCu high entropy bulk metallic glass (HE-BMG) alloy was produced using arc melting machine with critical diameter of 1.5 mm. The crystallisation kinetics and phase transformation mechanism of TiZrHfNiCu HE-BMG were investigated using differential scanning calorimetry (DSC) at single heating run under isothermal and isochronal conditions based on Johnson-Mehl-Avrami (JMA) theory. In isochronal heating, apparent activation energy for glass transition and crystallisation events were analysed by Kissinger, Ozawa and Augis and Bennett methods. Average activation energy value for crystallisation of TiZrHfNiCu amorphous alloys in isochronal modes was 226.41 kJ/mol for the first crystallisation and 297.72 kJ/mol for second crystallisation stages. The crystallisation mechanism of the first step was dominated by two and three-dimensional growth with increasing nucleation rate while the crystallisation mechanism in the second stage was dominated by two-dimensional crystallisation growth with constant nucleation rate. For isothermal condition, the,  $n$  value was less than 1.5 for all annealing temperatures, indicated that the crystallisation mechanism was diffusion-controlled growth of the pre-existing nuclei. The average activation energy was less than 280 kJ/mol with an increased crystallisation volume fraction.

**Keywords:** High entropy Bulk Metallic Glass; Crystallisation kinetics; Phase transformation; Sluggish diffusion

## 4.2 Introduction

High Entropy Alloys (HEAs) and Bulk Metallic Glasses (BMGs) are two type of novel materials that exhibit unique physical and mechanical properties [10, 12]. HEAs has been defined as a near equi-atomic ratio of multi-component alloys that form simple phases of body centered cubic (BCC), face centered cubic (FCC) or hexagonal closed packed (HCP) which is resulted from high entropy effect [12] while BMGs is an non-crystalline metallic alloys with a disordered atomic scale structure that produced by rapid cooling method [141]. High entropy bulk metallic glasses (HE-BMGs) have shown promising potential to express the advantages of HEAs and BMGs in tandem. High entropy effect in HE-BMGs result in low viscosity of the alloy melt thus it is expected to produce low glass forming ability (GFA) alloy. In contrast, it has been suggested that, the HE-BMGs may have a higher thermal stability and deliberate crystallization process due to its sluggish atomic diffusion [142, 143].

Since a development of HE-BMGs is a relatively new in research field, there is only a little investigation about crystallisation kinetics and thermal stability of this alloy up to now. Studies of kinetics of phase transformation in metastable nature of amorphous structure is very important to determine the thermal stability of this alloys since it tends to evolve towards more stable state when it is heated to a temperature higher than their glass transition temperature ( $T_g$ ). Therefore, the study of crystallization kinetics and mechanism of each phase is crucial in understanding the crystallization transformation kinetics and thermal stability of HE-BMGs.

In addition, studies of crystallization kinetics may provide routes of transformation of the alloys from randomly arranged structure into an ordered structure when the alloy is approaching equilibrium. The crystallisation of amorphous alloys upon heating can be performed in several ways. Generally, two basic methods are

considered, include isothermal and non-isothermal (isochronal). Previous works have highlighted a few methods for crystallisation kinetics studies for amorphous alloys [95, 103, 144]. It can be measured theoretically using Johnson-Mel-Avrami-Kolmogorov (JMAK) equation [111] by considering four assumptions: 1) isothermal crystallization state, 2) growth rate of new phases is controlled only by temperature 3) random and homogeneous nucleation of the second phase and 4) low anisotropy of the growing phase. Therefore, JMAK equation has been utilised in most research works for analysing crystallisation kinetics in isothermal conditions [104, 105, 109, 145, 146]

Moreover, JMAK equation can also be extended to be employed in non-isothermal condition with the assumption that overall nucleation process occur during early crystallization process and becomes neglected afterward [147]. This method is also widely used for non-isothermal crystallization kinetics studies in various amorphous alloys [148-152]. Different models have been proposed to measure the  $E_a$  for non-isothermal conditions includes Ozawa-Flynn-Wall method [119], Kissinger method [153] and Augis-Bennett method [154]. All of them are derived from Johnson Mehl Avrami (JMA) method having an Arrhenian temperature dependence.

To our best knowledge, to date, little studies has been focused on crystallisation kinetics particularly on HE-BMG in the scope of on similarities and differences between isothermal and non-isothermal crystallisation kinetics. Therefore, difference approaches were applied in this work to comparatively investigate the crystallization kinetics of TiZrHfNiCu HE-BMG, both isothermal and non-isothermal conditions using Differential Scanning Calorimetric (DSC) technique. The result obtained would determine the thermal behaviour of this alloy at elevated temperature.

### 4.3 Theoretical background

Apparent activation energy,  $E$ , local value of activation energy  $E(x)$  and local Avrami exponent,  $n(x)$  can be calculated from the DSC measurements.  $E_x$  and  $E_p$  are stand for to activation energy of nucleation and growth of crystal which is dependent on  $T_x$  and  $T_p$ . Energy,  $E$  in this study refers to the energy that required for each crystallisation step in the transformation process of amorphous to crystalline phase. Various methods have been proposed in order to evaluate the activation energy which are listed below:

Kissinger equation:

$$\ln \frac{T^2}{\beta} = \frac{E}{RT} + \text{const} \quad \text{Equation 4.1}$$

Ozawa equation:

$$\ln \beta = -\frac{E}{RT} + \text{const} \quad \text{Equation 4.2}$$

Augis-Bennett equation:

$$\ln \frac{T}{\beta} = \frac{E}{RT} + \text{const} \quad \text{Equation 4.3}$$

Kissinger-Akahira-Sunose (KAS) equation:

$$\ln \left[ \frac{T^2(x)}{\beta} \right] = \left[ \frac{E(x)}{RT(x)} \right] + \text{const} \quad \text{Equation 4.4}$$

where  $\beta$  is the heating rate,  $T$  denotes the characteristics temperatures at certain heating rate  $\beta$ ,  $R$  is the ideal gas constant,  $E$  corresponds the average apparent activation energy for each crystallisation events meanwhile  $E(x)$  represents the specific values of activation energy at certain crystallisation volume fraction which can be obtained from the KAS equation. In the KAS equation,  $x$  is the crystallisation volume fraction of each phase while  $T(x)$  is the temperature range from ( $0 < x < 1$ ) that varies with the heating rate  $\beta$ . The slope of each equation will represent the value of  $E/R$ .

Crystallized volume fraction as a function of temperature for isothermal and non-isothermal conditions can be deduced from the following equation:

$$\alpha = \frac{\int_{T_0}^T \left(\frac{dH_c}{dT}\right) dt}{\int_{T_0}^{T_\infty} \left(\frac{dH_c}{dT}\right) dt} = \frac{A_0}{A_\infty} \quad \text{Equation 4.5}$$

Where  $T_0$  and  $T_\infty$  are starting and ending temperature for the crystallisation process,  $dH_c/dT$  is the heat capacity at constant pressure while  $A_0$  and  $A_\infty$  are the area under the DSC curves where  $A_0$  is the area between  $T_0$  and any given temperature and  $A_\infty$  is the whole area between  $T_0$  and  $T_c$ .

Commonly, crystallisation kinetics of amorphous alloys is investigated in the frame of the Johnson-Mehl-Avrami-Kolmogorov (JMAK) theory. The value of Avrami exponent,  $n(x)$  describes the crystallisation mechanism which reflects the nucleation and growth behaviour in the alloys during the crystallisation process. In isothermal annealing,  $n(x)$  can be derived from JMAK equation:

$$x = 1 - \exp[-k(t - \tau)]^n \quad \text{Equation 4.6}$$

By taking ln on both side, this equation can be rewritten as:

$$\ln[-\ln(1 - x)] = n \ln(t - \tau) + \text{const} \quad \text{Equation 4.7}$$

where  $x$  is the crystallisation fraction at time,  $t$ ,  $\tau$  is a log of time or incubation time,  $n$  is the Avrami exponent and  $k$  is the kinetic coefficient as a function of absolute temperature. By plotting  $\ln[-\ln(1 - x)]$  versus  $\ln(t - \tau)$ , one can obtain the  $n$  value which is the slope of the curve as according to the following equation [155] :

$$n(x) = \frac{d \ln[-\ln(1-x)]}{d \ln(t-\tau)} \quad \text{Equation 4.8}$$

JMAK can be extended to be used in non-isothermal condition as suggested by Nakamura [156, 157].

Both equations of isothermal and non-isothermal annealing are shown below. For isothermal annealing, JMAK equation can be used directly as  $k(T)$  is a constant.

$$x = 1 - \exp \left\{ - \left[ \int_{t_0}^t k(T) dt \right]^n \right\} \quad \text{Equation 4.9}$$

However, for non-isothermal annealing where  $dT/dt=\phi$ , where  $\phi$  is the heating rate, it can be written as

$$x = 1 - \exp \left\{ - \left( \frac{1}{\phi} \right)^n \left[ \int_{t_0}^t k(T) dt \right]^n \right\} \quad \text{Equation 4.10}$$

By assuming  $\int_{t_0}^t k(T) dt = k'(T - T_0)$ , equation above can be rewrite as:

$$x = 1 - \exp \left\{ - \left( \frac{1}{\phi} \right)^n [k'(T - T_0)]^n \right\} \quad \text{Equation 4.11}$$

where  $k_0'$  is defined as a new kinetic coefficient as a function of temperature

$$k' = k_0' \exp \left( \frac{E_a}{RT} \right) \quad \text{Equation 4.12}$$

where  $k_0'$  is a constant, therefore, local Avrami exponent for non-isothermal condition can be deduced as follow:

$$n(x) = \frac{A d \ln[-\ln(1-x)]}{d \ln(t-\tau)/\phi} \quad \text{Equation 4.13}$$

Where  $A$  can be obtained from:

$$A = \frac{1}{1 + E_a/RT(1 - \frac{T_0}{T})} \quad \text{Equation 4.14}$$

#### 4.4 Experimental procedure

TiZrHfNiCu HE-BMG in equal atomic proportion (at.%) was prepared by arc melting under Ti-gettered argon atmosphere using highly pure elements which were above 99.5wt%. The alloys were melted for at least five times to ensure homogeneity. The alloy ingots were suction casted into a water-cooled copper mould with dimensions of 1.5 mm, 2 mm and 3 mm diameters and 30 mm length. Meanwhile, rapidly quenched ribbons form was prepared by re-melting the alloy ingots in quartz

crucible by induction melting while ejecting with a pressure of 40kPa through a nozzle onto a Cu wheel rotating with a surface velocity at 40m/s.

#### **4.4.1 Characterisations**

Structures of the as-cast and melt spun ribbons were examined by X-ray diffraction (XRD) using (Phillips D5000) Cu-K $\alpha$  radiation. It was then marked as S1, S2, S3 and S4 for ribbon, 1.5 mm, 2 mm and 3 mm respectively. Thermal analysis of the samples was carried out using (DSC, Perkin-Elmer Instruments, diamond) from 200-500 °C at 20 K/min to determine glass transition temperature ( $T_g$ ) and crystallization temperature ( $T_x$ ) using (DTA, Perkin Elmer STA 8000) machine from 400 to 1200 °C at 20 °C/min in argon atmosphere to determine the melting temperature. Both machines were calibrated using zinc standard. The morphology and chemical composition in each phase of the sample was investigated using scanning electron microscope (SEM Inspect F) equipped with energy-dispersive spectrometer (EDS).

#### **4.4.2 Crystallization kinetics experiments**

The experiments were conducted using a Perkin Elmer DSC-diamond, with a computerised data acquisition system. The DSC was set under the following conditions:

##### ***Non-isothermal Annealing***

The sample with 10 -20 mg in weight was put in the aluminium pan and heated from 200-500 °C with different heating rate at 20 K/min to 80 K/min. A purified argon gas was used throughout the experiment. The onset crystallization temperature was defined as the slope of tangent intersection in the DSC curve.

### ***Isothermal Annealing***

The sample was heated at high heating rate (100 K/min) to the specific temperature in supercooled liquid region (between glass transition and crystallization temperature) then held for 15 minutes until the crystallization process was completed.

## **4.5 Result and Discussion**

### **4.5.1 Alloys design**

The multicomponent high entropy alloys, TiZrHfNiCu HE-BMG alloys was reproduced from [79] based on the idea of forming glassy high entropy alloys from equal concentration of constituents element which did not contain any host element. The selection of the elements well in accordance with the three empirical rules described by Inoue *et al.* [35]. In order to determine the formability of solid solution in this alloy, thermodynamic and electronic parameters of the alloys include  $\Delta H_{\text{mix}}$ ,  $\Delta S_{\text{mix}}$ ,  $\delta$ ,  $\Delta\chi$ , VEC and  $T_m/T_c$  were calculated as shown in Table 4.1, where the relationship of enthalpy of mixing in each element pair is shown in Figure 4.1. These calculation has been used extensively for phase formation in predicting HEAs and BMGs [24, 37].

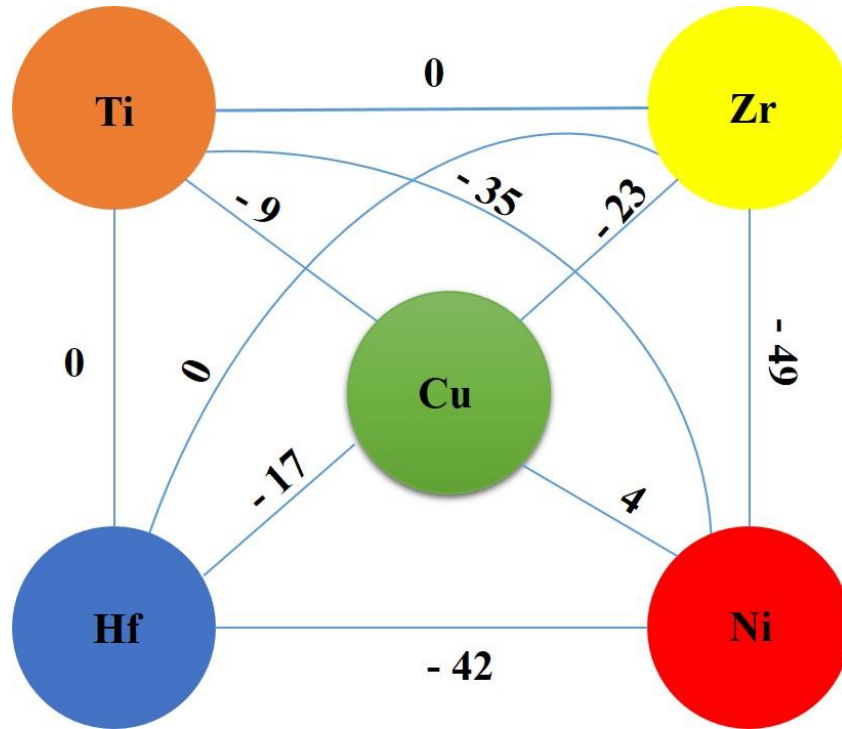


Figure 4.1: Relationship of heat of mixing among constituent elements in the TiZrHfNiCu HE-BMG alloy [79]

Table 4.1: Parameters of  $\Delta H_{\text{mix}}$ ,  $\Delta S_{\text{mix}}$ ,  $\delta$  and  $\Delta\chi$  for TiZrHfNiCu HE-BMG [79]

VEC	$\Delta\chi$	$\delta$	$\Delta H_{\text{mix}}$	$\Delta S_{\text{mix}}$
6.6	0.27	10.32	-27.36	13.38

Relationship of heat of mixing among the constituent elements in Figure 4.1 shows that Ni and Cu possessed negative heats of mixing against Ti, Zr and Hf. Obviously, Ni provided larger absolute values compared to Cu with Ti, Zr and Hf which resulted in strong attraction of interatomic forces between those elements that contributed to the formation of glassy phase in the alloys as calculated according to Miedema's model. On the other hand, Ni and Cu were located next to each other in the periodic table which result in positive enthalpy of mixing. Thermodynamic analysis revealed that the glass forming behaviour of Zr and Hf was similar, whereas it was different from that of Ti. The preferred formation of amorphous phases in the

system was attributed to high negative mixing enthalpy between the constituent elements.

The atomic size ratios in the present system were the secondary factor for the formation of the bulk glassy alloy. Table 4.2 has summarized the atomic size ratios among the elements in the present system. The atomic size ratios among Ti, Zr and Hf were less than 10%. While, the atomic size ratios for Ni and Cu with Ti, Zr or Hf were larger than 12%. Therefore, the larger negative heats of mixing for Ni with Ti, Zr and Hf might be suggested as the main reason for the formation of the bulk glassy while the atomic size ratio of Ni and Cu with Ti, Zr and Hf could be considered as additional factor that contributed to the glass formation in  $\text{Ti}_{20}\text{Zr}_{20}\text{Hf}_{20}\text{Cu}_{20}\text{Ni}_{20}$  alloy.

Table 4.2: Atomic size ratios for the elements in alloys system [158].

	Ti	Zr	Hf	Cu	Ni
Ti	X	10	9	15	18
Zr	10	X	1	27	30
Hf	9	1	X	25	28
Cu	15	27	25	X	2
Ni	18	30	28	2	X

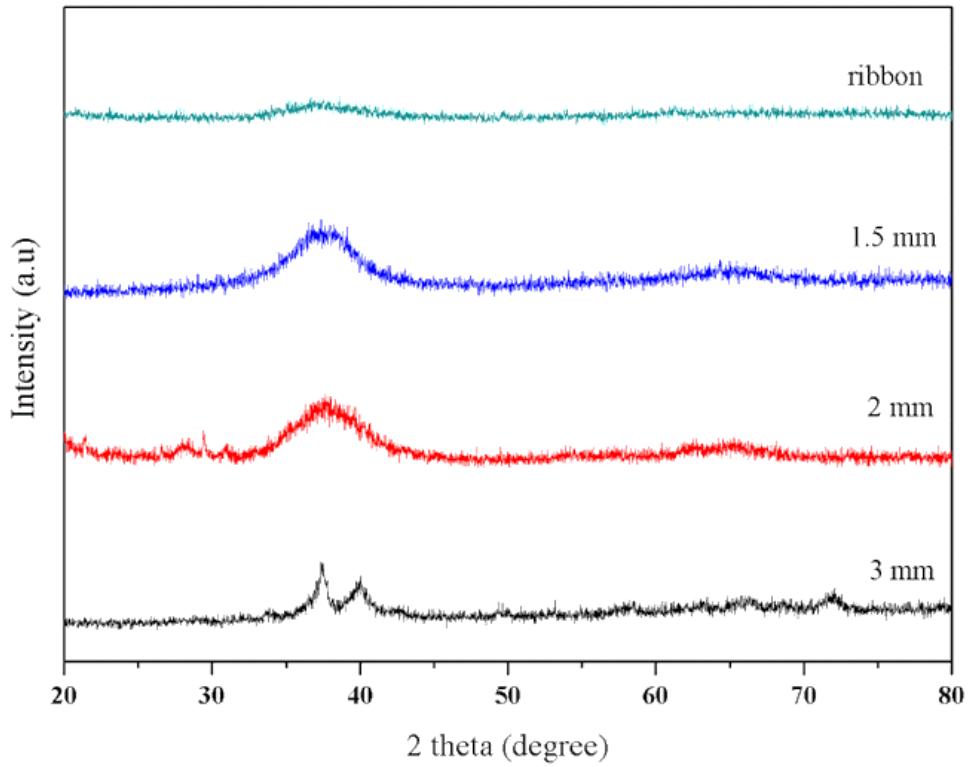


Figure 4.2: XRD patterns of the as prepared TiZrHfNiCu alloy at different casting diameter.

Table 4.3: Summary of sample diameter with phase identification from the XRD patterns.

Sample form	Phase Identification
3 mm rod	Crystalline
2 mm rod	Partly amorphous
1.5 mm rod	Amorphous
Ribbon 40m/s	Amorphous

Figure 4.2 shows the XRD patterns of the equi-atomic TiZrHfNiCu samples with cooling rate variations while Table 4.3 summarised the findings from the patterns. According to the diffractogram, it was clearly shown a broadened peak of 1.5 mm as-cast rod and 40 m/s melt spun ribbon at  $2\theta = 30-45^\circ$ , indicating that the alloy possessed fully amorphous structure. Partially amorphous structure could be observed in 2 mm rod due to existence of halo humps with some crystalline peaks at lower angle ( $2\theta =$

30-45°). Since the sample composes of mixture of amorphous and crystalline structure, the peaks are less intense and not clear at lower angle (20 to 30°). It may be because of the small sample size which need smaller step size and slower scan rate to get ideally sharp profile data particularly at lower angle. Figure 4.3 shows the XRD pattern of TiZrHfNiCu alloy with diameter of 2 mm produced by [79]. The alloy exhibited fully crystalline structure compared to the reproduced sample. It may be because of different cooling rate which might vary in different equipment.

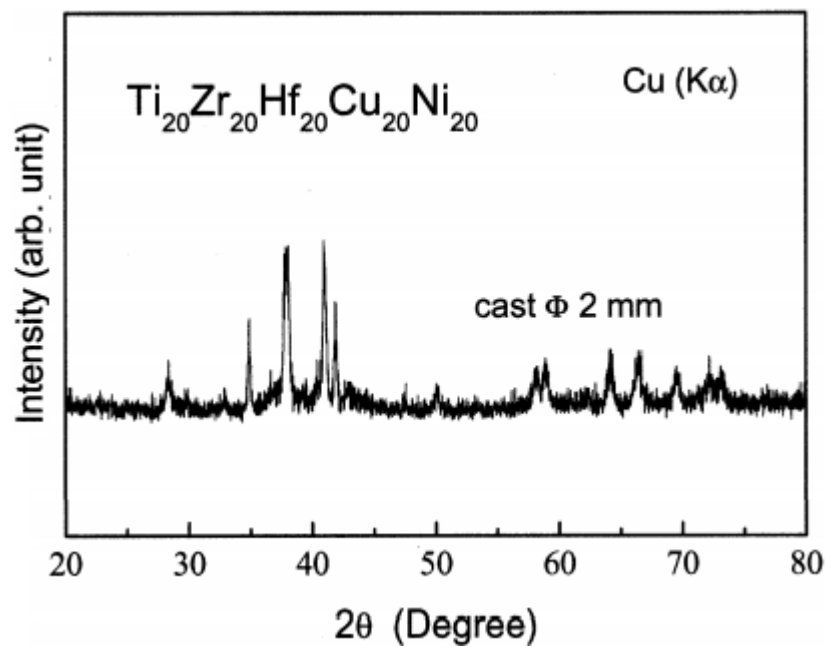


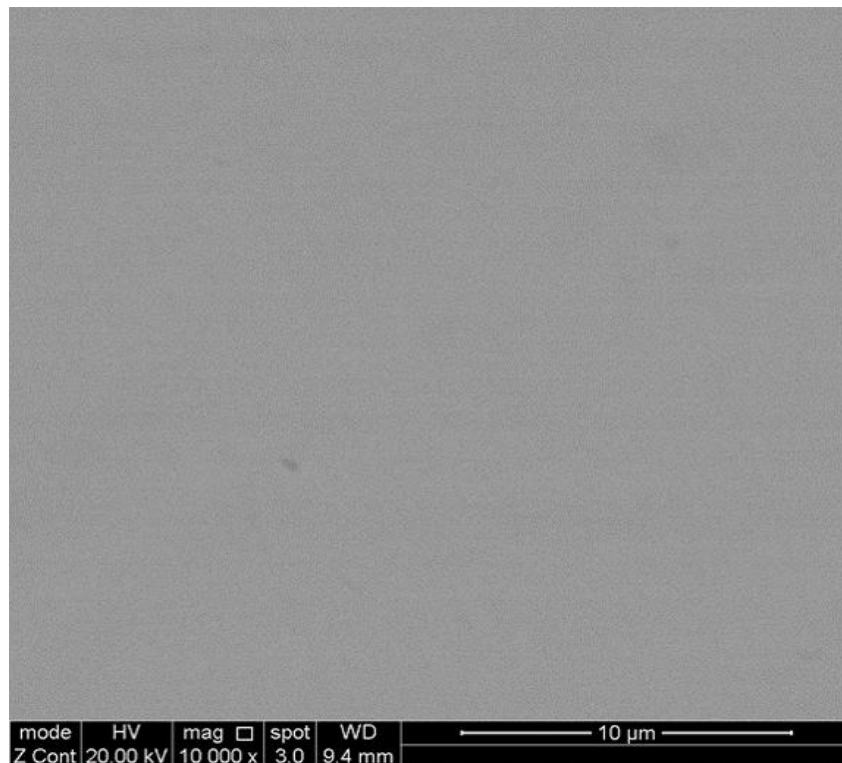
Figure 4.3: XRD pattern of fully crystalline TiZrHfNiCu alloy with diameter of 2 mm produced by [79] for comparison.

Meanwhile, 3 mm as-cast rod exhibited several sharp peaks, representing highly crystalline structure of the alloy. Thus, critical diameter for glass formation in equi-atomic TiZrHfNiCu high entropy metallic glass alloy laid between 1.5 to 2 mm diameters of casting size. Melt spun ribbon with 40 m/s wheel rotating velocity has high cooling rate compared to rod sample that undergo injection casting. Therefore,

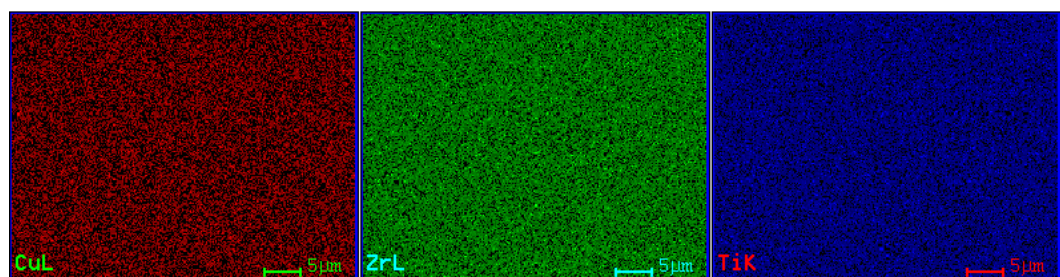
the atoms have limited time to re-arrange themselves in the crystal lattice thus forming an amorphous structure or short range ordered structure.

The backscattered SEM micrograph of the original microstructure and composition mapping of as-cast 1.5 mm TiZrHfNiCu HE-BMG specimen at 10,000 magnifications are shown in Figure 4.4 (a) and (b). The SEM microstructure displayed a typical featureless image indicated the glassy structure of the alloys. The composition mapping showed each of the constituent elements were distributed uniformly which indicated good chemical homogeneity in the alloy on a microscale.

(a)



(b)



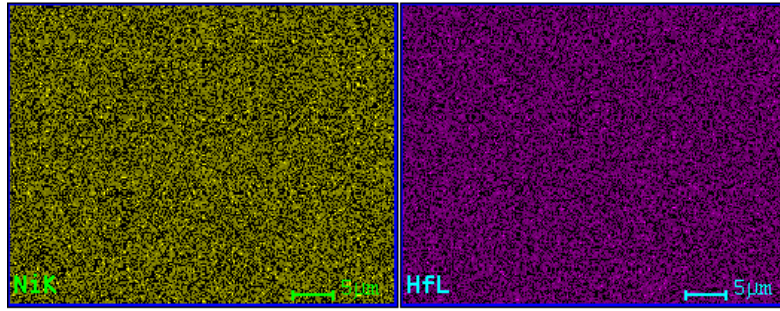


Figure 4.4: (a) SEM micrograph of the as cast TiZrHfNiCu HE-BMG and (b) Composition mapping of constituent elements Cu, Zr, Ti, Ni and Hf.

#### 4.5.2 Non-isothermal annealing

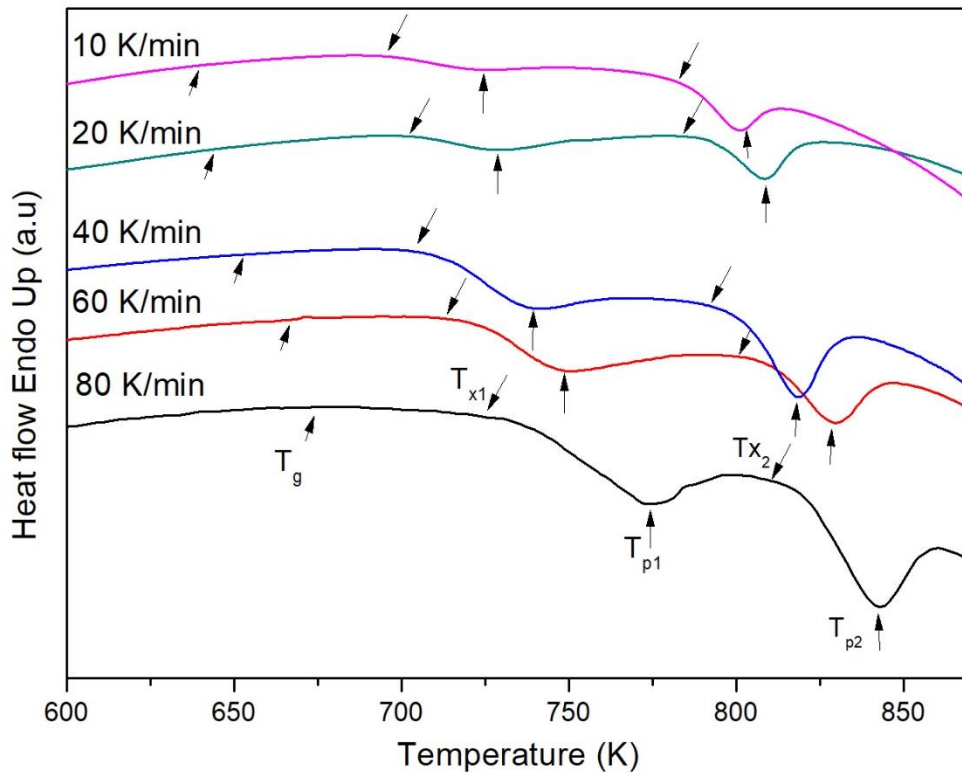


Figure 4.5: DSC curves of TiZrHfNiCu sample recording at various heating rates

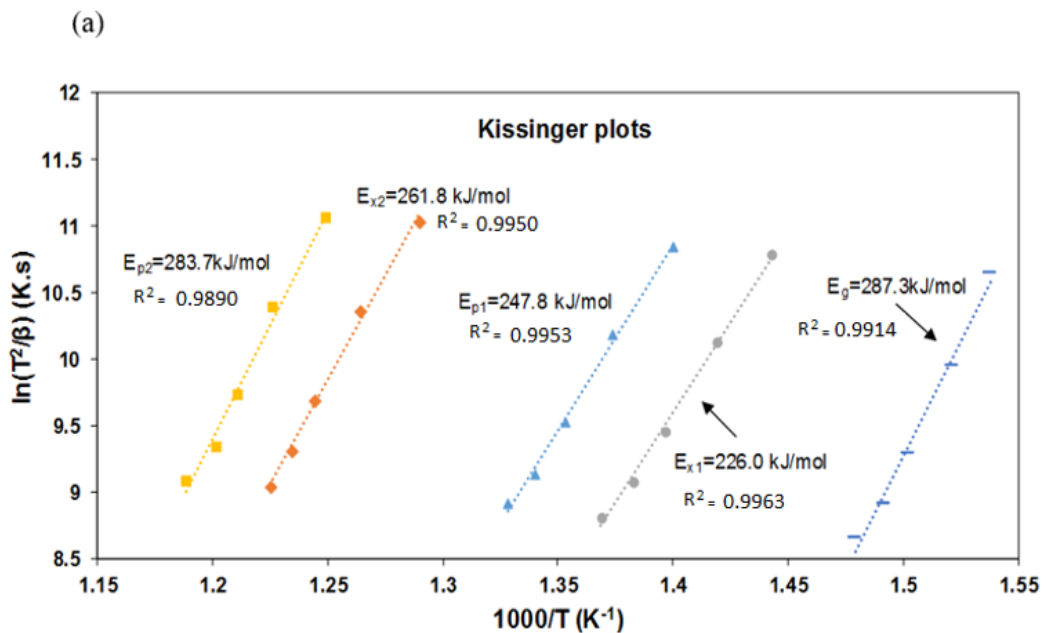
Table 4.4: Characteristic temperature ( $T_g$ ,  $T_{x1}$ ,  $T_{p1}$ ,  $T_{x2}$ ,  $T_{p2}$  and  $\Delta T_x$ ) for TiZrHfNiCu HE-BMG alloy at different heating rates

Heating rate (K/min)	$T_g$ (K)	$T_{x1}$ (K)	$T_{p1}$ (K)	$T_{x2}$ (K)	$T_{p2}$ (K)	$\Delta T_{x1}$ (K)
10	650.2	698.52	722.23	785.54	800.59	48.32
20	654.37	706.62	726.1	792.66	806.32	52.25
40	658.21	711.84	739.09	803.53	817.57	53.63
60	666.63	723.23	748.19	808.82	830.76	56.67
80	676.37	741.53	771.72	821.03	841.58	60.63

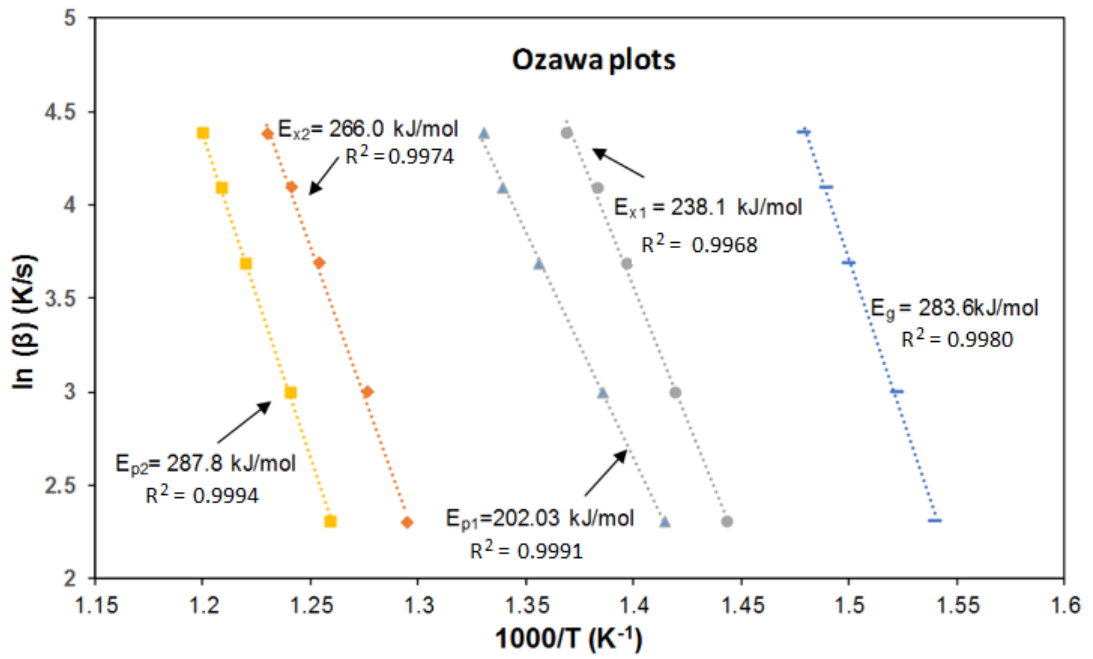
Figure 4.5 shows typical DSC curves for the amorphous TiZrHfNiCu HE-BMG alloy at five different heating rates (10,20, 40 60 and 80K min<sup>-1</sup>). All DSC curves in the temperature range of 650-850 K showed an endothermic event corresponding to the glass transition followed by two exothermic crystallisation peaks which indicated the multi-stage crystallisation process of the alloy. Therefore, the crystallisation process of this alloy was rather complex, in contrast to most of the conventional metallic glasses. It was suggested that, the multiple exothermic peaks was attributed to decomposition of the metallic bonding that lead to crystallisation process [159]. The onset of glass transition temperature,  $T_g$  and crystallisation temperature,  $T_x$  along with peak temperature for each crystallisation events and supercooled liquid region ( $\Delta T_x$ ) were listed in Table 4.4. Apparently, the temperatures of all peaks shifted to a higher temperature and the heat flow became larger with the increasing heating rate, which showed that the alloy possessed an apparent thermodynamic effect. This scenario also represented different thermal activation of each steps in the crystallisation process. Besides, it was also obvious that  $\Delta T_x$  increased from 48 K at 10 K/min to 60 K at 80 K/min which signified that nucleation was activated thermally, thus crystallisation was considerably dependent on the heating rate. Meanwhile, the glass transition temperature changed with heating rate due to relaxation process of the amorphous

alloy in the supercooled liquid region. Remarkably, TiZrHfNiCu HE-BMG possessed a larger supercooled liquid region of 50 K at 20 K/min heating rate as compared to Sr<sub>20</sub>Ca<sub>20</sub>Yb<sub>20</sub>Ma<sub>20</sub>Zn<sub>20</sub>; 36 K [160] but lower than TiZrHfNiBe; 66 K [103] and PdPtCuNiP; 65 K [89] at similar heating rate (20K/min), which indicated a relatively good thermal stability of this currently produced alloy among the other HE-BMGs.

In addition, thermal stability of the amorphous alloys can be evaluated using two important kinetic parameters which are, apparent activation energy of glass transition ( $E_g$ ) and crystallisation ( $E_x$ ).  $E_g$  can be described as energy for transformation from the glassy phase to the supercooled liquid,  $E_x$  is associated with the transformation energy of nucleation from the supercooled liquid state to crystallisation state. Another parameter,  $E_p$  is important to determine the energy for crystal growth. Therefore, a calculation of the apparent activation energy on each transformation event was conducted using three different equations; Kissinger, Ozawa and Augis-Bennett as shown in Figure 4.6.



(b)



(c)

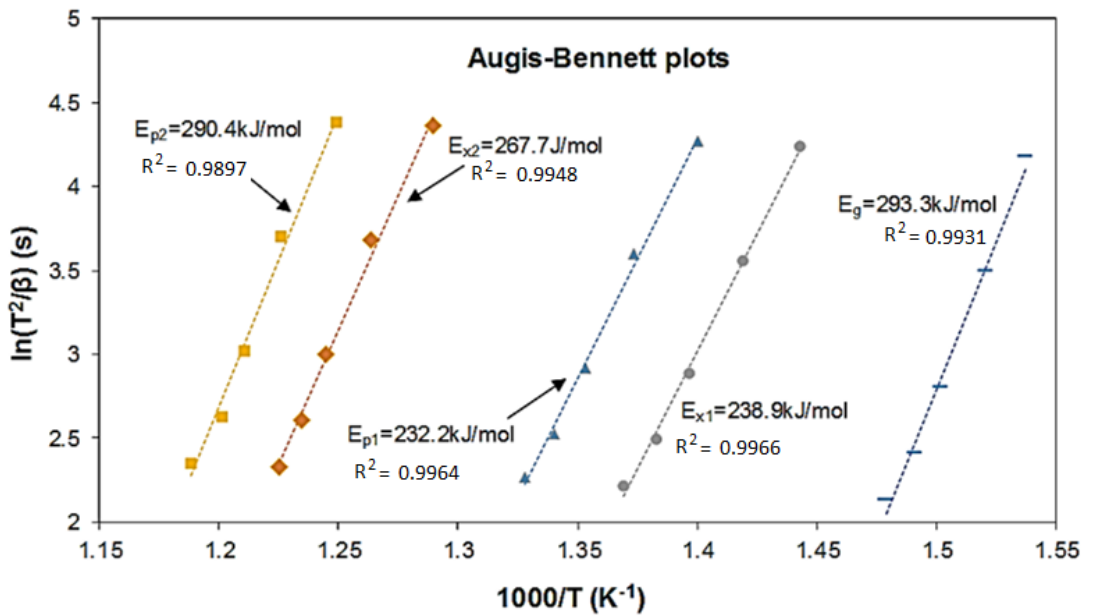


Figure 4.6: (a) Kissinger plot, (b) Ozawa plot and (c) Augis-Bennett plot of TiZrHfNiCu HE-BMG alloy

Table 4.5 Apparent activation energy for the glass transition and crystallization by Kissinger, Ozawa and Augis-Bennet method.

Alloy	Method	$E_g$ (kJ/mol)	First stage		Second stage	
			$E_{x1}$ (kJ/mol)	$E_{p1}$ (kJ/mol)	$E_{x2}$ (kJ/mol)	$E_{p2}$ (kJ/mol)
TiZrHfNiCu	Kissinger	287	226	247	261	283
	Ozawa	283	238	202	266	287
	Augis-Bennett	293	238	232	267	290
		$E_g$ (kJ/mol)	$E_{x1}$ (kJ/mol)	$E_{p1}$ (kJ/mol)	$E_{p2}$ (kJ/mol)	$E_{p3}$ (kJ/mol)
TiZrCuNiBe	Kissinger	317	307	296	347	374
[102]	Ozawa	312	303	284.6	343	369
Zr <sub>41.2</sub> Ti <sub>13.8</sub> Cu	Kissinger	535	162	203	271	301
<sub>12.5</sub> Ni <sub>10</sub> Be <sub>22.5</sub>						
[161]						

Activation energy can be defined as energy required for an atom before it become a part of activated cluster. The value of apparent activation energy for  $E_g$ ,  $E_{x1}$ ,  $E_{p1}$ ,  $E_{x2}$  and  $E_{p2}$  can be obtained by linear fitting method in Kissinger, Ozawa and Augis-Bennett plot in Figure 4.6 and the values were listed in Table 4.5. From the table, it was obvious that the apparent activation energy of glass transition and crystallisation estimated from Kissinger equation, Ozawa equation and Augis-Bennett equation are reinforcing each other. It was noticed that, for the first crystallisation event, the  $E_{p1}$  was smaller than  $E_{x1}$  in Ozawa and Augis-Bennett method which explained that, more energy was required for the nucleation than grain growth process. However, Kissinger value provided different result, where the value of  $E_{p1}$  was larger than  $E_{x1}$ . This phenomenon might result by large  $R^2$  value (0.878) of  $E_{p1}$  linear fitting in Kissinger plot. In addition,  $E_{x2} > E_{x1}$  shown in all analytical methods explained that, high energy barrier in second crystallisation compared to the first, implying that the first crystallisation stage was much easier for nucleation to occur. Therefore, the above

estimated data implied that nucleation and growth apparent energy for the first crystallisation stage gave almost similar value while the difficulties of growth process was much more significant in second crystallisation stage. The above statements was in agreement with the other crystallisation kinetics studies in metallic glass alloys [95, 102-104, 106].

The relatively high activation crystallization energy values in the second crystallisation stage showed that, significant number of atoms participated from the glassy alloys in the structural reorganization during the second stage of crystallisation process. Besides, this phenomenon might be attributed to a sluggish diffusion in high entropy alloys which resulted in difficulty for atomic diffusion [59]. It might also due to greater fluctuation of lattice potential energy that resulted in significant atomic traps and block which leading to high activation energy. Consequently, the nucleation and growth mechanism become slower due to reduction of nucleation rate that resulted from the sluggish diffusion. However, as compared to other reported HE-BMGs such as TiZrCuNiBe [103] and  $Zr_{41.2}Ti_{13.8}Cu_{12.5}Ni_{10}Be_{22.5}$  [161], the value of the apparent activation energy for TiZrHfNiCu was relatively small, indicated lower thermal stability of this alloy compared to the former alloys.

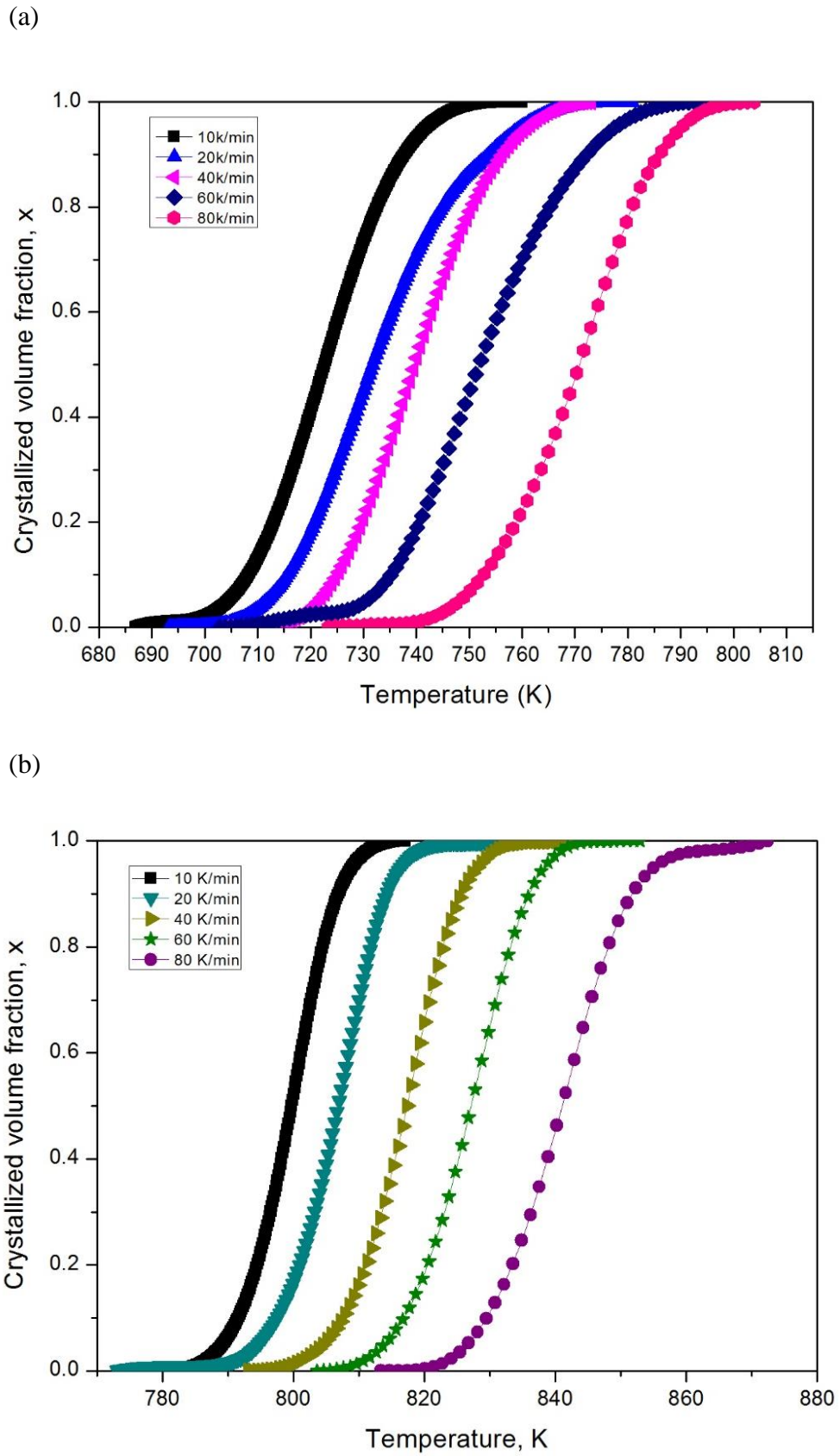


Figure 4.7: Plots of crystallized volume fraction  $x$ , versus temperature of TiZrHfNiCu HEBMG at different heating rates for (a) first and (b) second crystallization events

Table 4.6: List of local activation energy at different crystallisation fraction of the TiZrHfNiCu HE-BMG

x	$E_{x1}(x)$ (kJ/mol)	$E_{x2}(x)$ (kJ/mol)
0.1	245.33	323.5
0.2	250.64	307.2
0.3	260.95	297.8
0.4	258.07	295.23
0.5	264.38	301.04
0.6	261.55	293.73
0.7	260.39	296.89
0.8	246.09	284.0
0.9	223.33	280.09
Average	226.41	297.72

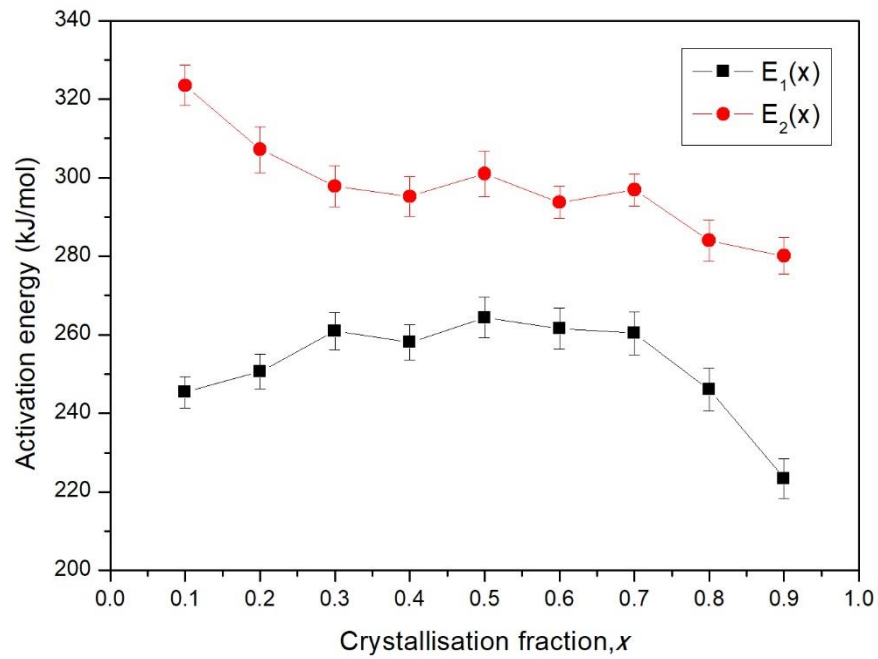


Figure 4.8: Plot of activation energy at difference crystallisation fraction for first and second crystallisation process

Figure 4.7 shows the crystallised volume fraction,  $x$  was for the first and second exothermic peaks was for TiZrHfNiCu HE-BMG with a dependence of temperature  $T$  at different heating rates while Table 4.6 shows the listed value of local activation energy at each crystallisation point. A sigmoid shape of the curves represented the difference of crystallisation rate at difference stages. In general, it was clearly shown that crystallisation occurred at a slower rate at the beginning ( $x < 0.2$ ), propagated at the middle ( $0.2 < x < 0.9$ ) and subsequently was slowed at the end of the process ( $x < 0.9$ ). Therefore, it was suggested that the transformation was divided into three stages; (i) the nuclei started to precipitate from the amorphous matrix slowly where the bulk crystallisation played an important role; (ii) subsequently increased the surface contact between nuclei and the amorphous matrix that caused the crystallised volume fraction to increase intensely and (iii) finally the surface between the crystalline phase and amorphous matrix decreased due to grain coalescence [162]. The higher activation energy values at the middle stage ( $E_{x1}(0.5) = 264.38\text{kJ/mol}$  and  $E_{x2}(0.5) = 301.04$ ) were due to the progressive crystallisation growth especially at the higher heating rate. This result was considerably consistent with the most isokinetics studies of amorphous alloys [95, 102, 110, 162]. Noticeably, the average value of local activation energy of  $E_{x1}$  was smaller than  $E_{x2}$  which was in a consistency with the result of apparent activation energy.

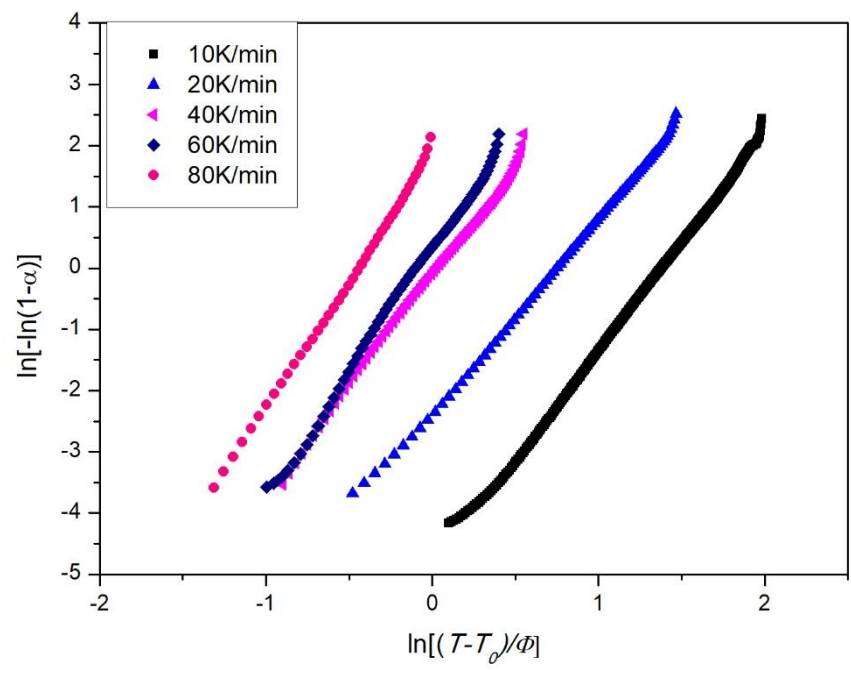
A trend of the activation energy at difference crystallisation point was plotted in Figure 4.8 for both crystallisation stages. The local activation energy trend for  $E_{x1}$  and  $E_{x2}$  was not similar at low crystallisation fraction ( $x < 0.5$ ), however the two plots show the highest local activation energy at  $x = 0.5$  and subsequently decreased with increase in crystallisation fraction. The higher value of  $E_{x2}(x)$  than  $E_{x1}(x)$  in the first crystallisation stage suggested the higher energy barrier which inhibited nucleation to

occur, thus resulted in reaction that occurred slowly which then reduced the rate of crystallisation fraction. The reduction of activation energy when  $x > 0.5$  owing to the decreasing nucleation rate that might be explained by local Avrami exponent,  $n(x)$ .

Local Avrami exponent,  $n(x)$  has been widely used in determining the nucleation and growth behaviours under isothermal condition. In order to utilise the JMA equation for non-isothermal crystallisation process, several conditions need to be satisfied [147]. It was suggested that, the crystallisation peak temperature,  $T_p$  of the alloy must be occurred at 0.60 to 0.63 range of crystallisation volume fraction,  $x$  [147]. For the present studies, the value of  $x_p$  at  $T_p$  were found in the range of 0.60 to 0.63.

By plotting  $\ln [-\ln (1-x)]$  versus  $\ln [(T-T_0)/\beta]$  following Equation 4.13, the  $n$  values might be obtained from the slope of the graphs as displayed in Figure 4.9. The values of the slope were listed in Table 4.7. The plot was found to be linear over most of the temperature range, but slightly deviated at higher temperature for all heating rates. The deviation could be due to saturation of nucleation at the final stages of crystallisation process. Besides, this situation was also resulted by crystal growth constraint for the small particles that restricted the nucleation process [163].

(a)



(b)

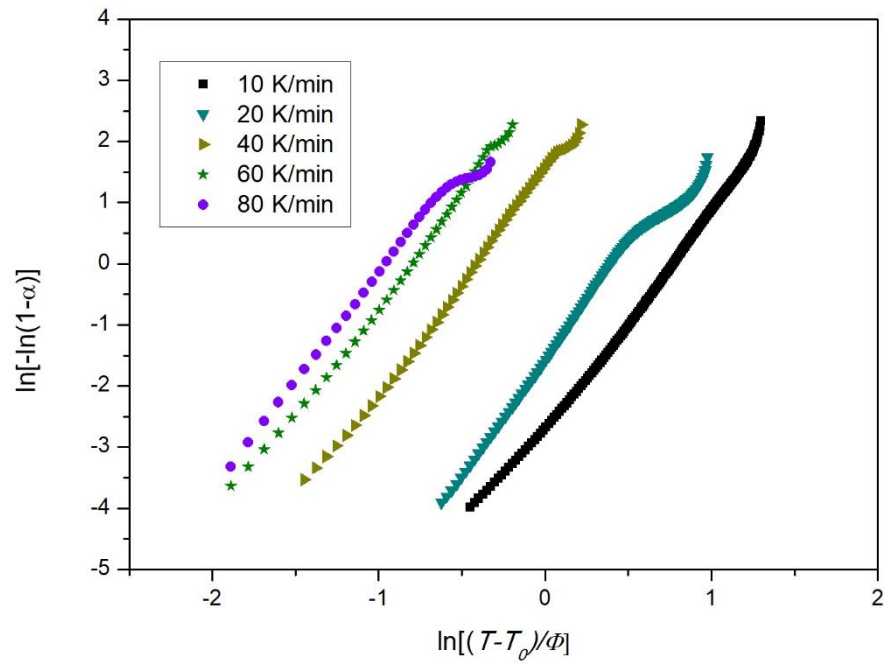


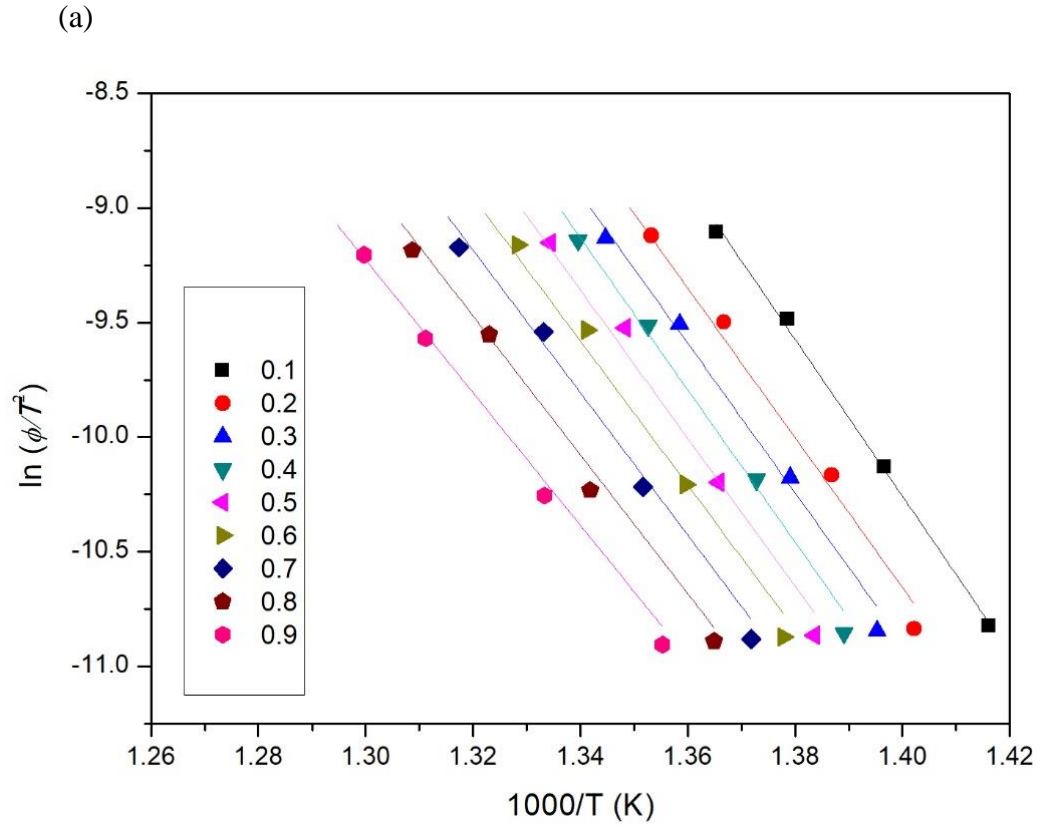
Figure 4.9: JMA plots of TiZrHfNiCu HE-BMG at different heating rates for (a) first and (b) second exothermic peaks.

Table 4.7: The value of  $n$  and  $m$  of Avrami exponent to determine nucleation modes and crystallisation mechanism in the alloy respectively.

<i>First crystallisation stage</i>		
Heating rate	$n$	$m (n=m+1)$
10	3	2
20	3	2
40	3	2
60	4	3
80	4	3
<i>Second crystallisation stage</i>		
10	3	2
20	3	2
40	3	2
60	3	2
80	3	2

From the calculated JMA exponent,  $n$  the value (which was the nucleation mode of the alloy) was proportionally increased as a function of heating rate in the first crystallisation stage where it was initially greater than 3 and subsequently increased to 4. The  $n$  value was not an integer and it was considered to be equal to  $n = m+1$ . Therefore, the value of  $m$  (which was an indicator of crystallisation behaviour) was equal to 2 but then increased to 3 at 60 K/min. The finding suggested that, the growth mechanism changed from the interface-controlled two-dimensional growth to the diffusion-controlled three-dimensional growth with increasing heating rate for the first crystallisation process. In contrast, for the second stage, the  $n$  values were constant ( $n = 3$ ) with increasing heating rate which signified that the growth of crystallisation two-dimensional growth with increasing nucleation rate at all heating rates. It is also found that, the  $n$  values increased in the first stage, but then became constant in the second stage as a function of heating rate. This is because, the sluggish atomic diffusion of this alloy at higher temperature (second stage) result in lower mobility of atomic

diffusion, leading to lower nucleation rate compared to first crystallisation stage for all heating rates.



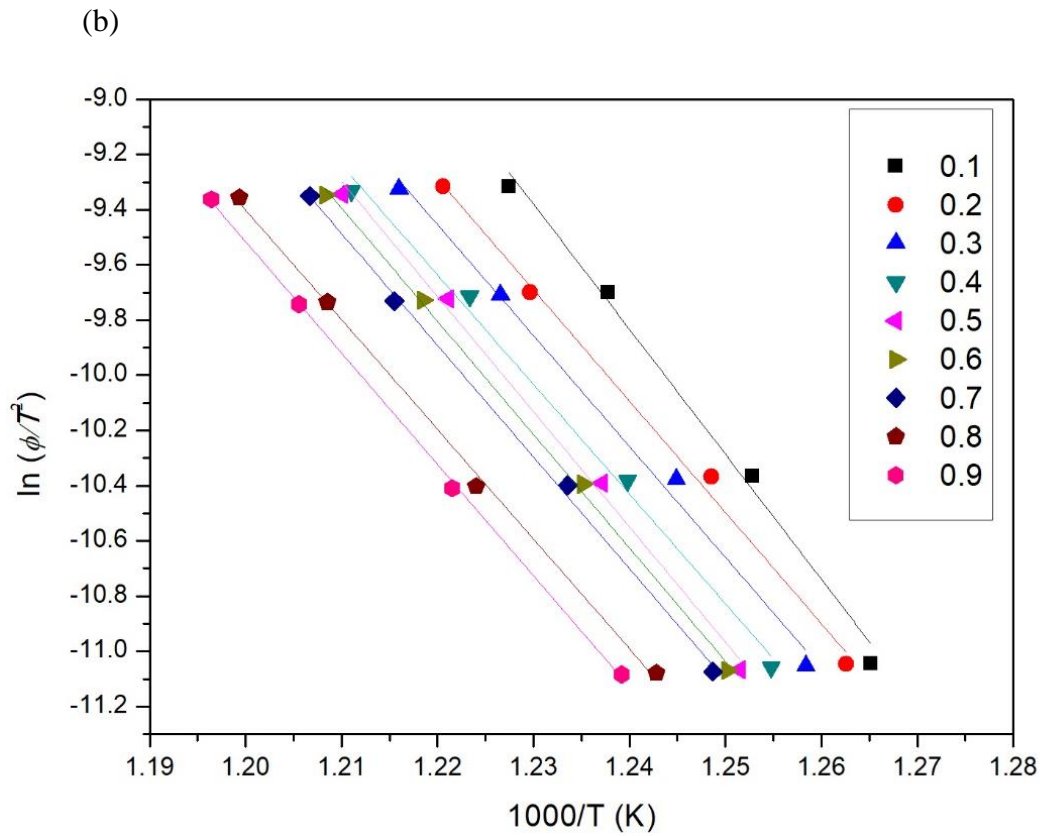


Figure 4.10: Kissinger-Akahira-Sunose (KAS) plots for different crystallization volume fractions  $x$  at (a) first and (b) second exothermic peaks.

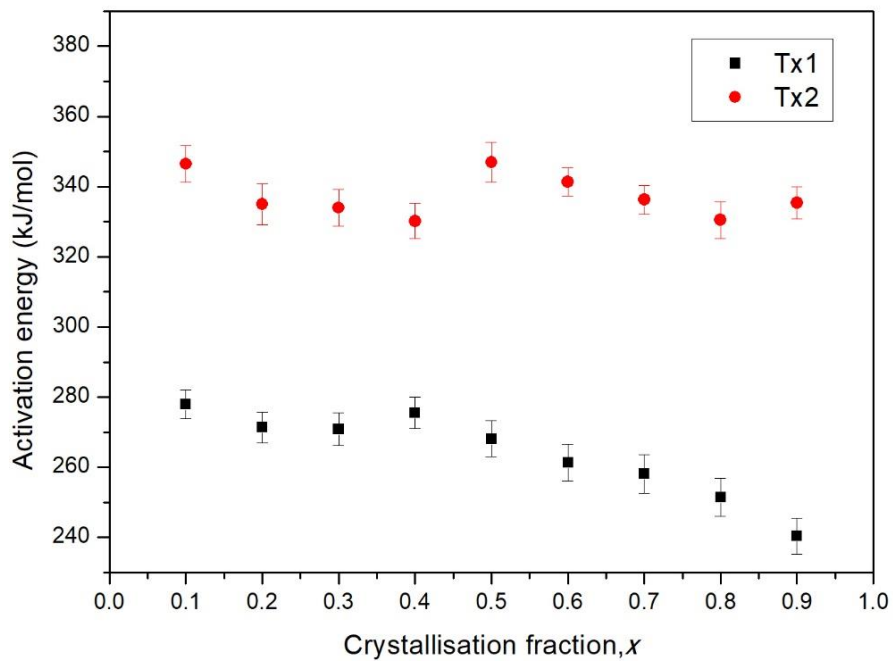


Figure 4.11: Local activation energy ( $E_a$ ) on the degree of crystallization volume fraction

In the KAS method, the variation of the crystallization temperature with heating rate,  $\beta$  was defined as shown in Equation 4.4. The activation energy calculated using KAS equation for TiZrHfNiCu HE-BMG at different states of transformation is shown in Figure 4.10. The local activation energies for different volume fractions of crystallization could be estimated by linear fitting slope of  $\ln(\beta/T^2)$  with respect to  $1000/T$ . Figure 4.11 shows the plot of the effective activation energies at different volume fractions for TiZrHfNiCu HE-BMG. Remarkably, the activation energy reached a maximum value of 280 kJ/mol when  $x = 0.4$  and 350 kJ/mol when  $x = 0.5$  for  $T_{x1}$ , and  $T_{x2}$  respectively. Subsequently, the activation energy decreased until the end of crystallization process. This occurrence was likely attributed to a typical mechanism of crystallisation where a maximum energy barrier must first be overcome to continue the crystallization process. From the current finding, it can be summarised that, the average value of activation energy for the first and second crystallisation stage from the KAS method was 225.97 kJ/mol and 261.80 kJ/mol respectively which was in a good agreement with the above statements.

### 4.5.3 Isothermal annealing

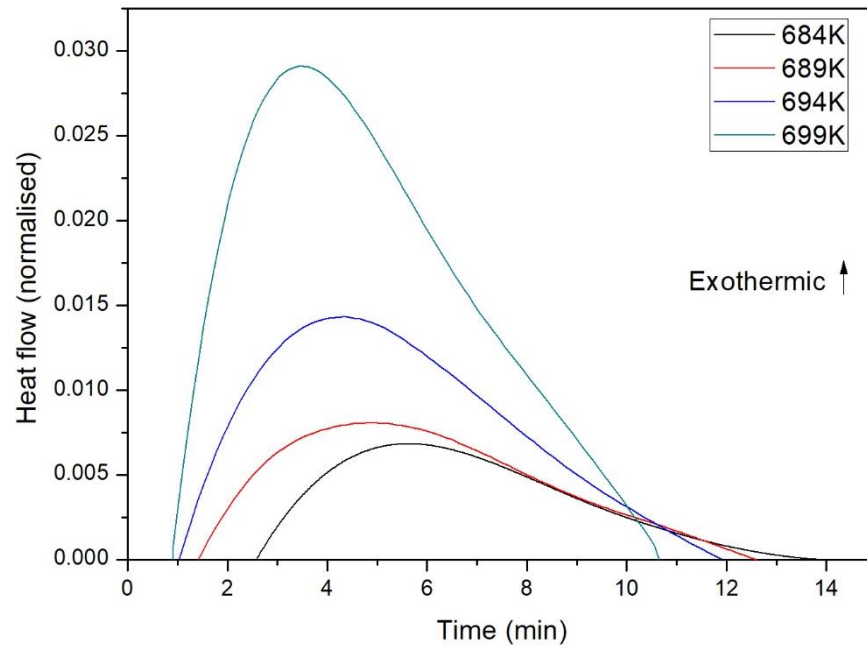


Figure 4.12: Isothermal DSC curves at various annealing temperature.

The isothermal crystallisation kinetics of TiZrHfNiCu HE-BMG was investigated by DSC at different temperatures between 684 K to 699 K (within supercooled liquid region). The DSC plots correspond to 684, 689, 694 and 699 K were shown in Figure 4.12. A single exothermic peak was observed in each curve, indicated a single crystallisation process after a certain incubation time where it is the time elapsed between the sample reaching annealing temperature and the beginning of the transformation. According to the graph, the width of exothermic peak became narrow and the incubation time decreased significantly with the increasing annealing temperature. This scenario implied that, slower diffusion occurred at lower annealing temperature where longer time was required for the nucleation to get started. However, at higher annealing temperature, atomic mobility facilitated concentration fluctuations required for the whole crystallisation process [164]. These conditions were in good agreement with previously reported studies in Zr-based metallic glasses [145], Cu-based metallic glasses [165] and Pd based metallic glasses[166]. In addition, the

incubation time for TiZrHfNiCu was higher compared to TiZrHfNiCuBe HE-BMG, yet the time range for completing the crystallisation process was much faster compared to the former.

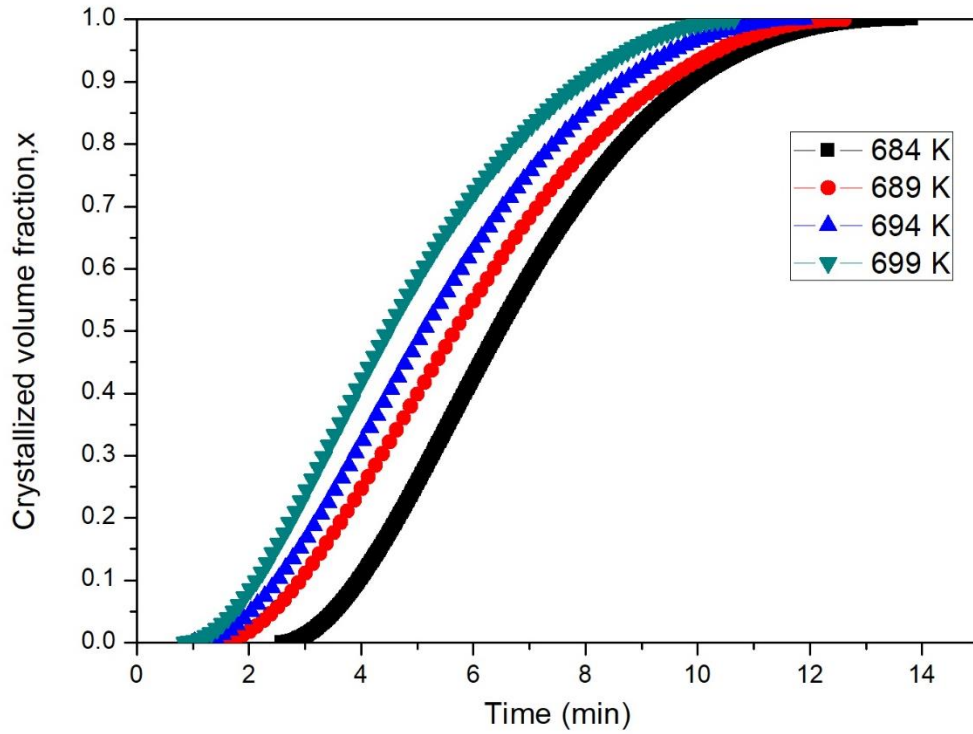


Figure 4.13: Crystallisation volume fraction,  $x$  as a function of annealing time for various annealing temperatures.

The crystallisation volume fraction with respect to time ( $t-\tau$ ) can be determined by measuring the fractional area of the exothermic peak in each annealing temperature as shown in typical sigmoidal curve as in Figure 4.13. Therefore, the crystallisation fraction at any time can be obtained by measuring the partial area of the exothermic peak.

The JMA model was employed to find the Avrami exponent,  $n$  that reflects the characteristics of nucleation and growth of the alloys during crystallisation, while  $k$  is a reaction rate constant which respect to annealing temperature. It can be obtained by plotting  $\ln[-\ln(1-x)]$  against  $\ln(t-\tau)$  as illustrated in Figure 4.14. The slope of the curve

was employed in order to determine the  $n$  value while  $k$  is the intercept of the straight line fitted by the least square method. The value of  $n$  and  $k$  were listed in Table 4.7. The data shows, the value of Avrami exponent varied from 1.5 to 1.7 with increasing annealing temperature which implied that the crystallisation process was governed by diffusion controlled of one-dimensional growth of pre-existing nuclei with decreasing nucleation rate. No indication of two-dimension progressive nucleation was found, however the Avrami exponent value was a bit lower at higher annealing temperature indicated that relatively low progressive of nuclei at higher temperature even though the nucleation was started earlier than the other sample. This is proved as that the nuclei created instantaneously (took shorter incubation time) during the relaxation time at higher annealing temperature.

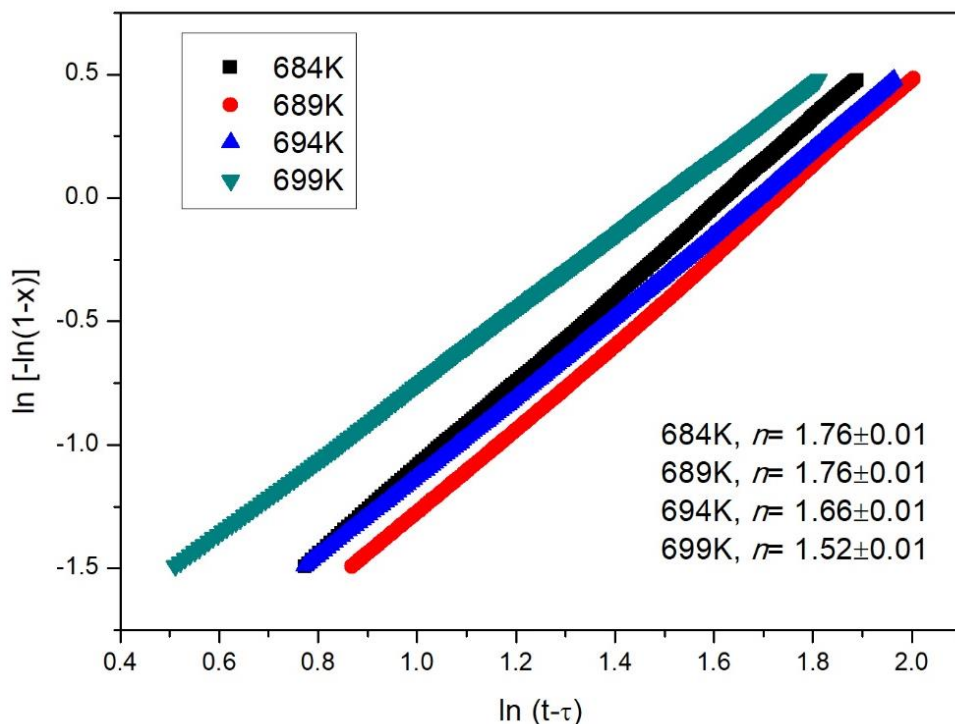


Figure 4.14: Crystallisation volume fraction as a function of annealing time for different annealing temperature.

Table 4.8: The kinetic parameters of TiZrHfNiCu HE-BMG under isothermal annealing conditions.

Annealing Temperature (°C)	Incubation time, $\tau$ (min)	Avrami exponent, $n$	Reaction constant, $k$ (min <sup>-1</sup> )
684	2.58	1.77	1.05
689	1.39	1.76	1.11
694	1.03	1.66	1.03
699	0.85	1.52	0.81

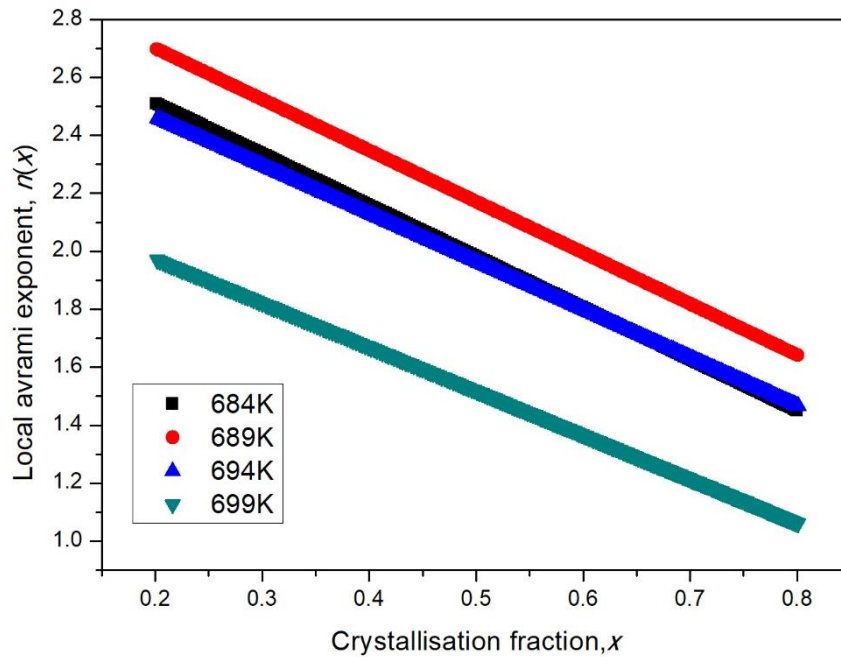


Figure 4.15: Local Avrami exponent as a function of crystallisation fraction at different annealing temperature.

The nucleation and growth during the whole crystallisation process in the current studies do not remain constant, yet has different behaviour at different stages.

Therefore, the variation of the  $n(x)$  with crystallisation fraction,  $x$  at different annealing temperature was plotted as displayed in Figure 4.15. The value of  $n(x)$  varied around 2.8 to 2.0 at initial stage of crystallisation for all annealing temperature and continuously decreases towards the completion of crystallisation process. As far as diffusion-controlled growth theory was concerned [164], it has been described that,  $n = 1.5$  corresponds to the growth of particles with nucleation rate close to zero;  $1.5 < n < 2.5$  reflects growth of particles with decreasing nucleation rate;  $n = 2.5$  indicates growth of particles with constant nucleation rate while  $n > 2.5$  shows the growth of small particles with an increasing nucleation rate. From this theory, it can be summarised that, the mechanism of crystallisation process in this alloy was varied at different crystallisation fraction. It was started by particles growth with increasing nucleation rate at  $x = 0.2$  towards zero nucleation rate which gradually became close to saturation at the final stage of crystallisation process,  $x = 0.8$ . Interestingly, at annealing temperature of 699 K, the  $n$  value was the lowest ( $< 2.0$ ) among the others at the starting stage of crystallisation ( $x = 0.2$ ) which indicated decreasing of nucleation rates with one dimensional growth of crystal.

The low crystallisation process that was observed in this alloy at high annealing temperature provided the evidence for the sluggish diffusion kinetics. This finding was associated with the theory of sluggish diffusion in HEA principles. The theory states that the sluggish diffusivity of atomic movement could slow down the phase transformation particularly at elevated temperature [48, 167]. However, this result was contradicted to the conventional alloys where the atomic diffusion increased with increasing annealing temperature. Yet, the result is in agreement with the value of avrami exponent in TiZrHfNiCuBe HE-BMG where the nucleation rate decreased at higher annealing temperature [103].

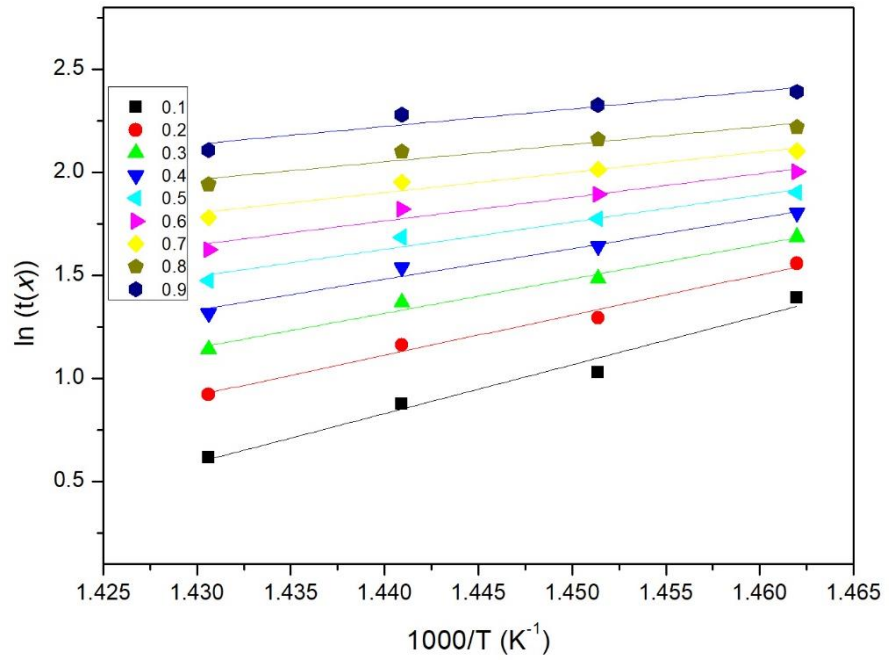


Figure 4.16: Plots for activation energy determination for isothermal annealing in TiZrHfNiCu HE-BMG

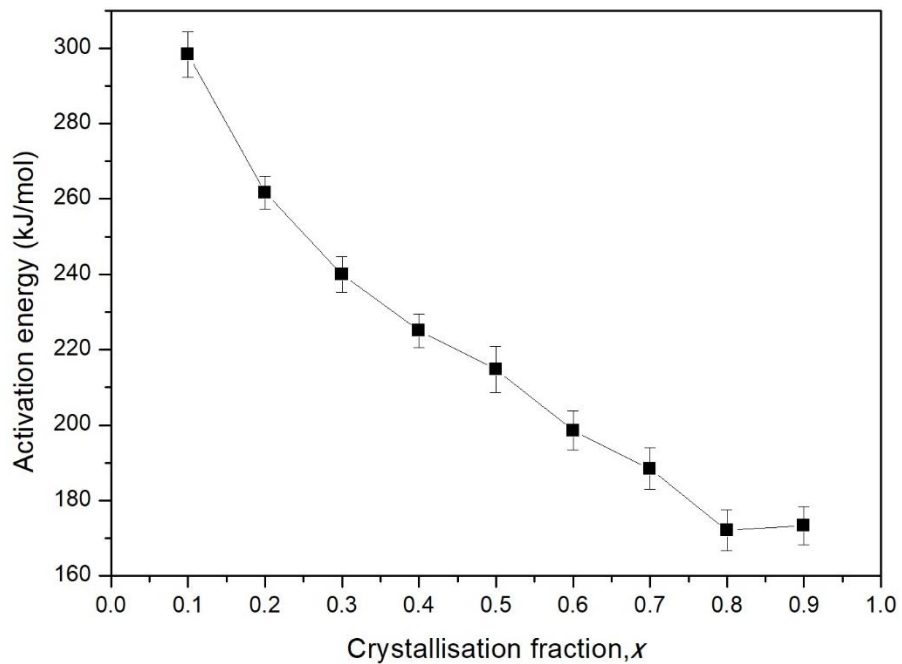


Figure 4.17: Activation energy as a function of crystallisation volume fraction,  $x$  in isothermal mode

The difference of nucleation and growth behaviour during crystallisation process can be reflected with the variation of activation energy at different

crystallisation phases. Arrhenius equation (Equation 4.12) can be used to calculate the activation energy in isothermal condition for amorphous alloy at different crystallisation stage as shown in Figure 4.16. By using the experimental data of crystallisation fraction ( $x$ ) as a function of annealing time (Figure 4.14), the plot of  $\ln(t(x))$  with respect to  $1/T$  can be fitted linearly given a slope of  $(E_a/R)$ . Subsequently, the local activation energy,  $E_a(x)$  at different crystallisation stages can be obtained and demonstrated as illustrated in Figure 4.16. From the figure, it was shown that the  $E_a(x)$  decreases as the proceeding of crystallisation.  $E_a$  decreased rapidly from the initial crystallisation stage where  $x < 0.2$  until the middle of the process where  $x > 0.6$ . Moreover, the  $E_a$  showed an almost constant value when  $x > 0.8$  which indicated the saturation of nucleation sites in the alloys system.

The average activation energy in isothermal condition calculated using Arrhenius equation was smaller compared to the value in non-isothermal conditions calculated by Kissinger equation (see Figure 4.11). This phenomenon was exceptional for most of reported conventional amorphous alloys. For example  $\text{Cu}_{52.5}\text{Ti}_{30}\text{Zr}_{11.5}\text{Ni}_6$  (Cu-based metallic glass) [165] and  $\text{Zr}_{65}\text{Cu}_{27}\text{Al}_8$  (Zr-based metallic glass) [168] that showed a larger value of activation energy in isothermal mode compared to non-isothermal mode. It has been claimed that, continuous heating involves higher temperature that induces crystallisation process compared to isothermal heating mode (heating in supercooled liquid region). Therefore, higher energy is required for the transformation process from metastable to the stable state. In contrast, in this study, the average activation energy in isothermal annealing was smaller than non-isothermal annealing. This scenario might be due to the entropic effect in HEA where TiZrHfNiCu HE-BMG possessed a lower thermal stability at lower temperature while the atomic diffusion become more sluggish at higher temperature. However, there is

no evidence to date for this hypothesis since very little studies reported for crystallisation kinetics HE-BMG. In fact, some of the conventional alloys especially Ti-based [169], Cu-based [104] and Zr-based [170] amorphous alloys crystallised at relatively higher temperature during isothermal heating process indicates a better thermal stability as compared to HE-BMG.

#### 4.6 Conclusions

Kinetics of crystallisation in TiZrHfNiCu HE-BMG was investigated by DSC method in both isothermal and non-isothermal conditions. The information regarding activation energy and crystallisation mechanism reflect the resistance of crystallisation during heating. From the finding, a few summaries can be drawn as:

1. Two stages of crystallisation process was found under non-isothermal condition. It was shown that TiZrHfNiCu has higher apparent activation energy ( $E_{x1}$  and  $E_{p1}$ ) compared to conventional Zr-based alloys but lower than TiZrCuNiBe HE-BMG.
2. The average value for activation energy in isothermal condition was lower than non-isothermal condition. Therefore, the kinetics reaction barrier in non-isothermal condition was higher than isothermal annealing mode.
3. The Avrami exponent values,  $n$  was increased in the first crystallisation stage and became constant in the second crystallisation stage for non-isothermal annealing. Meanwhile, in isothermal annealing the  $n$  value was constant at 1.5, implies that diffusion-controlled growth with decay nucleation rate.
4. It is suggested that, high mixing entropy in TiZrHfNiCu alloy successfully retard lattice diffusion at higher temperature in non-isothermal condition and at high annealing temperature in isothermal condition, lead to a sluggish crystallisation process.

## CHAPTER 5

### Design of Lamellar-structured High Entropy Alloys with the Addition of Boron Content

#### 5.1 Abstract

A methodology for design of lamellar-microstructure high entropy alloy systems through the addition of boron was presented. The BCC/B2 microstructure of well-characterised FeCoNi(Al<sub>0.1</sub>Si<sub>0.1</sub>) was changed into a multi-phase system, consisting of FCC and BCC/B2, and Fe<sub>2</sub>B type intermetallic phases by substitution of boron as shown by XRD. The volume fraction of each phase was determined by Rietveld refinement. The microstructures of as-cast alloys were observed to be a lamellar structure comprised of nanostructured lamellae with alternating Fe<sub>2</sub>B and FCC phases and was confirmed by SEM and TEM. Thermodynamic studies were performed by calculating the value of  $T_m$ ,  $T_c$ , and  $T_\Omega$  of the alloys as a function of boron content. Based on the calculated interfacial energy values, the highly-disordered structure was attained at low boron content, which has higher interlamellar spacing, possesses high interface energy.

**Keywords:** High entropy alloys; Microstructure; Interfacial energy; Phase transformation.

## 5.2 Introduction

The field of High Entropy Alloys (HEAs) has recently attracted global attention. HEAs reportedly can offer a capacity to form a simple solid solution (here, the simple solid solution is defined as a phase that are derived from FCC, BCC, or HCP) over that of complex structures (non-simple phases that are also referred to as intermetallics in other fields) despite containing more than 4 near-equimolar components [20]. It has been proposed that the formation of intermetallic compounds is suppressed through the reduction of the Gibbs free energy by entropy, thus stabilising the simple solid solution, especially at elevated temperatures [17, 167] which is dominated by entropy. Consequently, a material with desirable properties at these temperatures, such as excellent wear resistance, high mechanical strength, good creep and softening resistance deriving from their severe lattice distortion and sluggish diffusion kinetics can be produced. It must of course be acknowledged that the universality and origin of these effects in HEAs has been questioned [60].

Due to the changes of alloy designs from corners to centers of phase diagrams, unique microstructures that can provide excellent properties for alloys improvement has been developed. For instance, the development of in-situ composites, eutectic HEAs (EHEAs) has been found to be a good candidate for high temperature alloys, balanced mechanical properties of ductile and brittle phases and good quality castability in outsized scale [171, 172]. Various EHEAs have been developed to date with the idea of combining a ductile phase (e.g: FCC solid solution) with a hard phase (e.g: BCC solid solution or intermetallic phase) [128, 135, 136, 172-174]. The phase transformation may occur with an increase of element addition in alloy compositions from the hypoeutectic, the eutectic to the hypereutectic alloy [69, 175-178] and

subsequently change the mechanical and other properties include electrical, magnetic, wear and electrochemical.

Most of the reported EHEAs described effects of the element addition on microstructures to their properties [69, 135, 172, 173, 179, 180]. For example, Tong *et al.* [69] prepared a series of  $\text{Al}_x\text{CoCrFeNiCu}$  and found the eutectic microstructures of FCC and BCC mixtures were attained at  $x$  between 0.8 and 2.8. A unique sunflower-like eutectic cluster microstructure was reported in  $\text{Al}_2\text{CrCuFeNi}_2$  EHEA which was a primary phase that solidified spherodically or ellipsoidally and grew in a radial manner following the eutectic phases [180]. A fine lamellar structure of FCC and B2/BCC phases in  $\text{AlCoCrFeNi}_{2.1}$  provided an excellent balance between strength and ductility [135]. Moreover, after undergoing cold rolling and annealing process, a remarkable mechanical properties with ultimate tensile strength of  $\sim 1.2$  GPa and  $\sim 12\%$  elongation to failure has been observed resulting from the ultrafine granular grain structure of the alloy [135].

However, the reported literatures on EHEAs were commonly focused on the microstructure without providing a detail explanation on the metastability of the alloy system. Besides, most of the articles not able to provide the theoretical evidence such as phase diagram in order to prove the formation of eutectic phase in the alloy system. A consideration of physical properties alone such as morphology of the phases presented was considerably insufficient to claim the alloy as is EHEAs but a eutectic-like structure instead. Tan *et al.* [181] raised a concern on the formation of EHEA in their report since the alloy exhibited a two-phased microstructure even though it has obeyed the design rules for a single phase solid solution of HEA.

The HEA composition of  $\text{FeCoNi}(\text{Al}_{0.1}\text{Si}_{0.1})$ , has been reported as BCC/B2 structure [182], thus in this study the composition was chosen for a modification with

boron (replacing aluminium). There is a clear scope for improving the desired properties of HEAs through a development of an understanding of patterns which affects HEA microstructure. In addition, the effect of element additions on thermodynamic stability of the alloy was presented in this work. This current work was not only focussing an enrichment of current lamellar structure-type HEAs (eg: EHEA) but also including an importance to the metastability of the alloys design. This also will be correlated to the previous studies in Chapter 4 where the phase transformation occurred in the alloy with the addition of boron. Therefore, this chapter investigated the interdependence between HEA crystal structures, morphology and metastability of the alloy as a function of boron content.

### 5.3 Experimental procedure

A series of alloy ingots with nominal composition of equi-atomic  $\text{FeCoNi}(\text{B}_x \text{Al}_{1-x})_{0.1}\text{Si}_{0.1}$  (where  $x = 0, 0.2, 0.4, 0.5, 0.7, 0.9$  and  $1.0$ ) were denoted as B0, B0.2, B0.4, B0.5, B0.7, B0.9 and B1.0 respectively. The alloys were synthesised by arc-melting using high purity starting elements in a Ti-gettered under argon atmosphere, and subsequently suction-casted into a water-cooled copper mould with dimensions of 3 mm diameter and 60 mm length.

The microstructure of the as-cast sample was examined through X-ray diffraction using Phillips D5000 diffractometer with  $\text{Cu-K}\alpha$  radiation scanning from  $20^\circ$  to  $90^\circ$  of diffraction angle. The XRD data were then analysed using the GSAS [138] Rietveld refinement with EXPGUI [139] as a graphical interface. The analysis was performed based on crystal structure data in PDF 4+ [183]. A number of parameters were carefully refined including (1) the phase scale factors and the background of the patterns, (2) the lattice parameters, (3) the Pseudo-Voight profile functions parameters and anisotropic lattice strain parameter for each phase and (4) atomic positions of each

phases. The maximum spherical harmonic order of 12 was selected after the refinement with 14 and 16 showed high  $\chi^2$  value. Finally, the quantitative analysis of the phases volume fractions were performed as described by [184]. The surface morphology of the samples was investigated using backscattered electron imaging, conducted by SEM FEI Inspect F machine. Higher resolution studies of the alloys were performed using TEM, Philips EM420 machine in which the specimens were prepared by mechanically grinding and electropolishing technique using ethanol and perchloric acid as an etchant.

## 5.4 Results and Discussion

### 5.4.1 Predictions of phase formation using empirical rules of HEA formation

**Table 5.1** Parameters of  $\Delta H$ ,  $\Delta S$ ,  $\delta$  and  $\Delta X$  for  $\text{FeCoNi}(\text{B}_x \text{Al}_{1-x})_{0.1}\text{Si}_{0.1}$  alloys.

Designation	Nominal composition	$\Delta H_{\text{mix}}$ (kJ/mol)	$\Delta S_{\text{mix}}$ (J/mol)	VEC	$\Omega$
B0	$\text{Fe}_{0.27}\text{Co}_{0.27}\text{Ni}_{0.27}\text{B}_{0.00}\text{Al}_{0.10}\text{Si}_{0.1}$	-19.21	12.62	7.90	1.10
B0.2	$\text{Fe}_{0.27}\text{Co}_{0.27}\text{Ni}_{0.27}\text{B}_{0.02}\text{Al}_{0.08}\text{Si}_{0.1}$	-19.64	13.04	7.90	1.13
B0.4	$\text{Fe}_{0.27}\text{Co}_{0.27}\text{Ni}_{0.27}\text{B}_{0.04}\text{Al}_{0.06}\text{Si}_{0.1}$	-20.07	13.18	7.90	1.14
B0.5	$\text{Fe}_{0.27}\text{Co}_{0.27}\text{Ni}_{0.27}\text{B}_{0.05}\text{Al}_{0.05}\text{Si}_{0.1}$	-20.28	13.20	7.90	1.14
B0.7	$\text{Fe}_{0.27}\text{Co}_{0.27}\text{Ni}_{0.27}\text{B}_{0.07}\text{Al}_{0.03}\text{Si}_{0.1}$	-20.71	13.12	7.90	1.14
B0.9	$\text{Fe}_{0.27}\text{Co}_{0.27}\text{Ni}_{0.27}\text{B}_{0.09}\text{Al}_{0.01}\text{Si}_{0.1}$	-21.14	12.89	7.90	1.10
B1.0	$\text{Fe}_{0.27}\text{Co}_{0.27}\text{Ni}_{0.27}\text{B}_{0.10}\text{Al}_{0.00}\text{Si}_{0.1}$	-21.36	12.62	7.90	1.07

Guo *et al.* [33] used 2D maps to plot the data for  $\delta - \Delta H_{\text{mix}}$  on some of HEAs and BMGs. It was reported that a solid solution was more frequently formed at the enthalpy of mixing was between  $-11.6 < \Delta H_{\text{mix}} < 3.2$ , suggested that the base B0 composition as listed in Table 5.1 might be considered an outlier. However, by employing the empirical VEC, calculated as a weighted average of the nominal composition [185]

showed that the VEC of all compositions studied were constant at 7.9 (as boron and aluminium, which it replaced, were both located on the same period of the periodic table). This phenomenon might lead to different stabilities which is due to very different electronic level as the elements are in the same period but on different rows. Indeed, the recent work showed the actual VEC (which was derived from first-principles calculations) might be used as a better predictor of HEA phase stability [186] in comparison to the empirical VEC.

Thermodynamically, a ratio of the melting temperature (here, the melting temperature was approximated as a weighted average of all alloying components) to the ratio of the enthalpy of mixing to the entropy of mixing,  $\Omega = \frac{T_m}{T_\Omega} = \frac{\Delta H_m T_m}{\Delta S}$  [37] was used as a predictor of phase formation. For HEAs, values of  $\Omega > 1$  were considered to stabilise the solid solution phase. Following this criterion, compositions of B0.4 to B0.7 were expected to be closest to a HEA-forming composition.

#### 5.4.2 Determination of phase presence by XRD characterisation

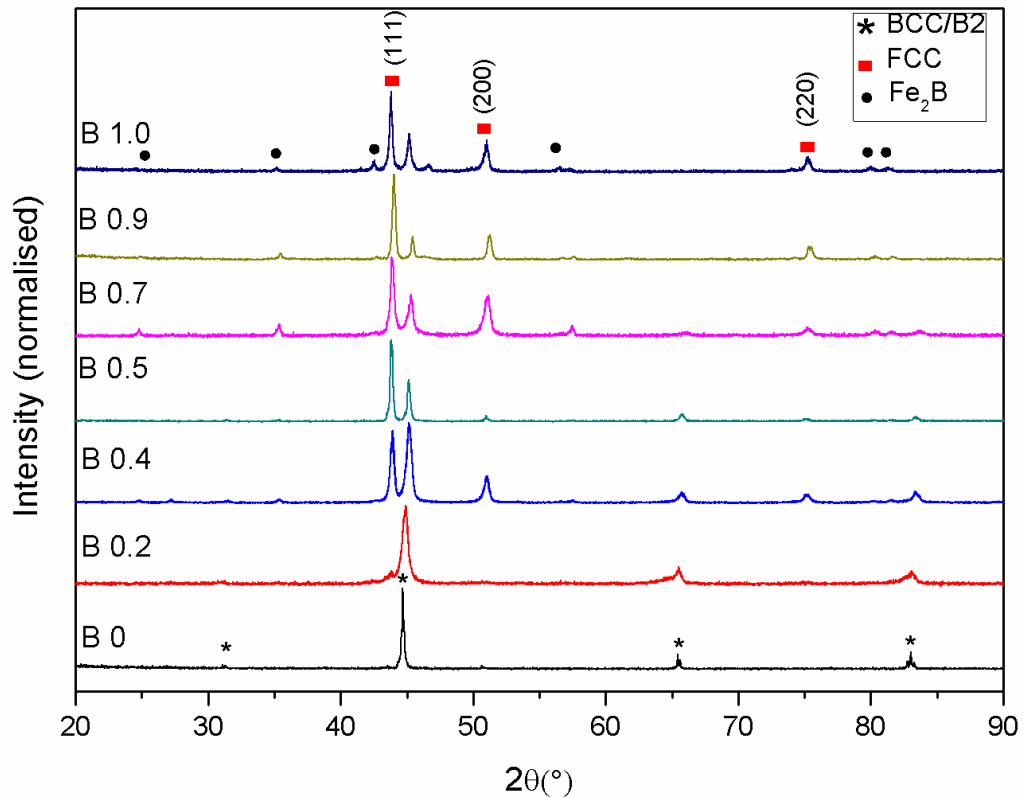


Figure 5.1: XRD patterns of  $\text{FeCoNi}(\text{B}_x\text{Al}_{1-x})_{0.1}\text{Si}_{0.1}$  with increasing boron content

XRD patterns of  $\text{FeCoNi}(\text{B}_0\text{Al}_{1.0})_{0.1}\text{Si}_{0.1}$  in Figure 5.1 showed that as-cast samples possessed a BCC/B2 phase. However, the introduction of boron induced the formation of secondary phases (presented in FCC and the  $\text{Fe}_2\text{B}$  intermetallic structure). As boron addition increased, the BCC/B2 diffraction peaks weakened, whilst the intensity of peaks corresponding to the FCC and  $\text{Fe}_2\text{B}$  structure increased. This phenomenon signified that the substitution of aluminium with boron suppressed the formation of BCC/B2 while promoting the formation of the  $\text{Fe}_2\text{B}$  phase.

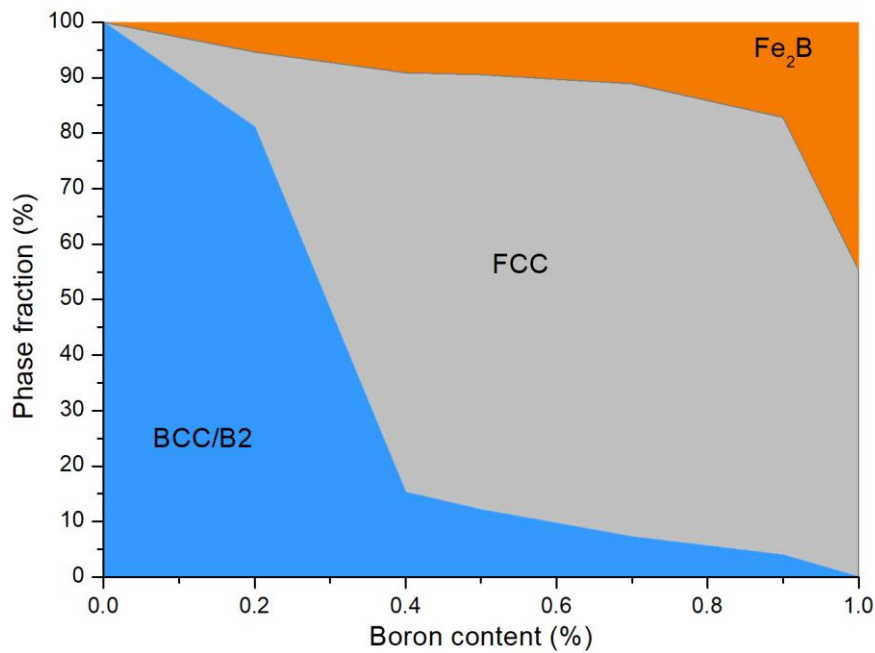


Figure 5.2: Phase fraction of each composition determined from experimental XRD data by Rietveld refinement

Rietveld refinement of the XRD peaks was performed in order to obtain the phase fractions of each composition, and these results were presented in Figure 5.2. The values given can be considered as mostly accurate with the quality of fitting and lower value of  $\chi^2$ . From the graph, it was observed that the volume fraction of BCC/B2 phase decreased from 99.7% to 81.1% when boron is replacing 0.2 mol% of aluminum from the base alloy composition. The addition of 0.2 mol% boron reduced the stability of the BCC/B2 phase, leading to the precipitation of the other two phases which were FCC (13.44%) and Fe<sub>2</sub>B (5.42%). However, at 0.4 mol% boron, the volume fraction of FCC phase increased significantly to 75.5%. This situation might be related to the higher configurational entropy and  $\Omega$  as shown in Table 5.1 which indicated the higher stability of the solid solution at this composition as compared to the others. As boron increased from 0.7 to 1.0 mol%, the volume fraction of FCC and B2 gradually decreased while the Fe<sub>2</sub>B phase content grew. This phenomenon was

attributed to a depletion of Al below 30% reduced the configurational entropy required to form a random HEA solid solution phase which was considerably in good agreement with  $T_m/T_\Omega$  thus resulted in the reaction of Fe and B in forming  $Fe_2B$  intermetallic phase. Besides, this finding suggested that the difference in enthalpy between simple phases and more complex phases could also be the reason for decreased in the volume fraction of FCC and BCC/B2.

It appeared in the table that the parameter  $\Omega$  was not distinguish between the stability of the FCC and BCC/B2 structure for predictions of stability between B0.2 – B0.7. Furthermore,  $\Omega$  values for B0.9 and B1.0 were 1.10 and 1.07, respectively. This phenomenon suggested that the phase stability for B0.0 ( $\Omega = 1.10$ ) and B0.9 ( $\Omega = 1.10$ ) was found to be similar. This scenario was not in accordance to the observed XRD characterisation results (*c.f.* Figure 5.1), where three phases were observed to exist in B0.9, in contrast to the single phase B0. Previously, it has been reported that the B2 phase is always coherently present with the BCC phase in a similar Al containing HEA,  $CrFeCoNiAl_x$ , which is attributed to spinodal decomposition [72]. This situation suggests that the BCC/B2 structure is partially ordered and may be considered to be a metastable structure, explaining the increase in predicted stability using the calculated values of  $\Omega$ .

In order to understand the effect of metastability, the effect of B addition on the undercooling of the alloy was taken into consideration. The critical undercooling,  $\Delta T_C$  is defined as the temperature below the melting temperature at which metastability is lost and is used as an additional parameter in conjunction with  $T_\Omega = \frac{\Delta H}{\Delta S}$  to determine phase stability in HEAs. The critical undercooling can be used to determine the minimum temperature at which metastable phases may form by subtracting the critical

undercooling from the melting temperature,  $T_c = T_m - \Delta T_c$ . It may be obtained from the following expression [191]:

$$\Delta T_c = 0.5 X^{3/2} (\Delta s_e/k)^{1/2} T_m \quad \text{Equation 5.1}$$

where  $X$  is the parameter of proportionality from the Stefan-Skapski-Turnbull formula which is reported to be between  $0.3 < X < 0.6$  [191, 192]. Values of  $(\Delta s_e/k)^{1/2} \approx 1$ . Using values of  $\Delta s_e = \Delta s_{mix}$  returns values between 1.22 – 1.26, which range is in relatively good agreement with  $(\Delta s_e/k)^{1/2} \approx 1$ . [191]. Schmelzer and Abyzov reported a simplified expression of the Stefan-Skapski-Turnbull formula (for non-equilibrium melt-crystal states) for as a function of the critical cluster size as:

$$X_{2d} = \tau(36\pi)^{-1/3} = 0.2 \text{ to } 0.6 \quad \text{for} \quad \tau = 1 \text{ to } 3 \quad \text{Equation 5.2}$$

where  $\tau$  is a measure of the thickness of the cluster surface (or the number of monolayers in the surface) [192],  $\Delta s_e$  is the difference in entropy at phase equilibrium (approximated as the mixing entropy of an ideal HEA solid solution),  $k$  is the Boltzmann constant, and  $T_m$  is the melting temperature (approximated from the rule-of-mixtures). From their analysis it was found that  $0.2 < X_{2d} < 0.6$  (for values of  $1 < \tau < 3$ ), which was in good agreement with  $X$ . Therefore,  $X_{2d}$  was substituted for  $X$  in this work.

Average  $\tau$  values of 2 corresponded to  $X = 0.41$ ; a  $\tau$  value of 1 corresponded to the smallest possible cluster size required for the formation of a metastable structure, while larger  $\tau$  values corresponded to larger cluster sizes and may correspond to

reduce stability of the metastable structure as a larger cluster size is required. This relation will be further discussed below.

For the B2 structure various alloy compositions, the semi-ordered (0.5 0.5 0.5) atom is surrounded by 8 closest neighbours. Here, the highest enthalpy of mixing pairs, Al-Ni, Al-Co, and Al-Fe ( $\Delta H = -22, -19, \text{ and } -11 \text{ kJ/mol}$ , respectively) may be considered to be dominant at the nearest neighbour distances in a BCC-like structure [186, 193]. Therefore, only one of the eight atoms are needed to form an Al-X pair with the (0.5 0.5 0.5) atom in our representative BCC structure, and the minimum thickness is calculated as  $\tau = 1 + \frac{1}{8} = 1.125$ , which corresponds to  $X = 0.23$ .

It was emphasised that, the above approximation was used as an initial estimate to study the metastability of this composition, as obtaining exact values is a non-trivial problem, and further detailed study will be required to obtain exact values. To confirm validity of obtained phase stabilities, the theoretical phase stabilities predicted from this assumption were compared to the current experimental results.

Substituting  $X$  into Equation 5.1 then allowed the critical undercooling temperature to be calculated for the range of the  $\text{FeCoNi}(\text{B}_x\text{Al}_{1-x})_{0.1}\text{Si}_{0.1}$  compositions studied in this work. Figure 5.3 shows a plot of the melting temperature,  $T_m$ , the critical undercooling temperature,  $T_C = T_m - \Delta T_c$ , and the parameter  $T_\Omega$ , the temperature at which  $\Delta H$  was balanced by  $T\Delta S$ .

In order to verify the use of the value  $\tau = 1.125$ , corresponding to  $X = 0.23$ , two separate plots are presented. Figure 5.3(a) represents a plot for values of  $X=0.41$ , which corresponded to the average values of  $X$  [31].  $T_m > T_\Omega$  (denoted by the blue-highlighted region), corresponded to the temperature at which the HEA solid-solution was stabilised (near  $\Omega > 1.1$ ).  $T_\Omega < T_m$  (denoted by the grey-highlighted region), corresponded to the temperature at which the temperature for a stability of solid

solution.  $T_{\Omega} = \Omega T_m$  remained higher than that of the critical undercooling temperature, implying that the solid solution might be able to sustain a metastable semi-ordered state. Comparing Figure 5.3(a) with Figure 5.3(b), apparently, at  $X = 0.23$ ,  $T_c$  was shifted to higher temperature, and a region at which  $T_{\Omega} > T_c$  (denoted by the orange-highlighted region) now existed. Since a given phase reached the thermodynamic limit for metastability (here the HEA solid-solution was approximated as a pseudo single-component phase) at  $T_c$  [31], a disordered solid solution was not possible below this temperature, and the region corresponded to an area where ordered structures were anticipated to form. This phenomenon explained that values of  $T_c > T_{\Omega}$  were considerably indicative as a partial ordering of the solid solution since  $T_c$  might be taken to be an indicative of the spinodal point if it existed [31]. The grey-shaded region suggested the possibility of B2 presence in  $\text{FeCoNi}(\text{B}_x \text{Al}_{1-x})_{0.1}\text{Si}_{0.1}$ , which was in good agreement with Ma *et al.* [30].

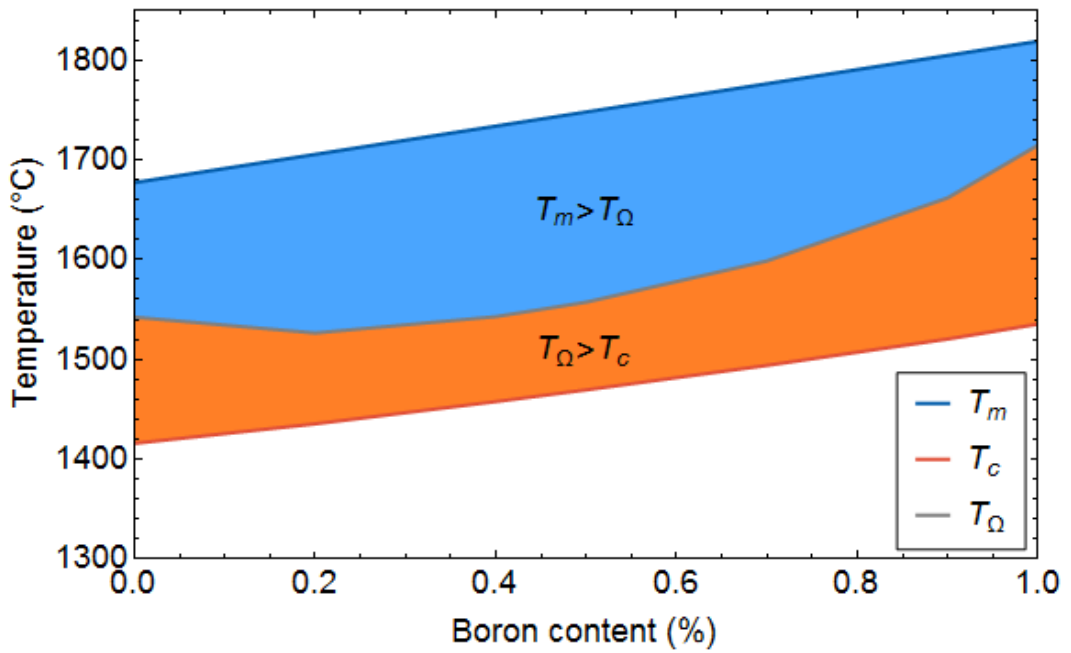
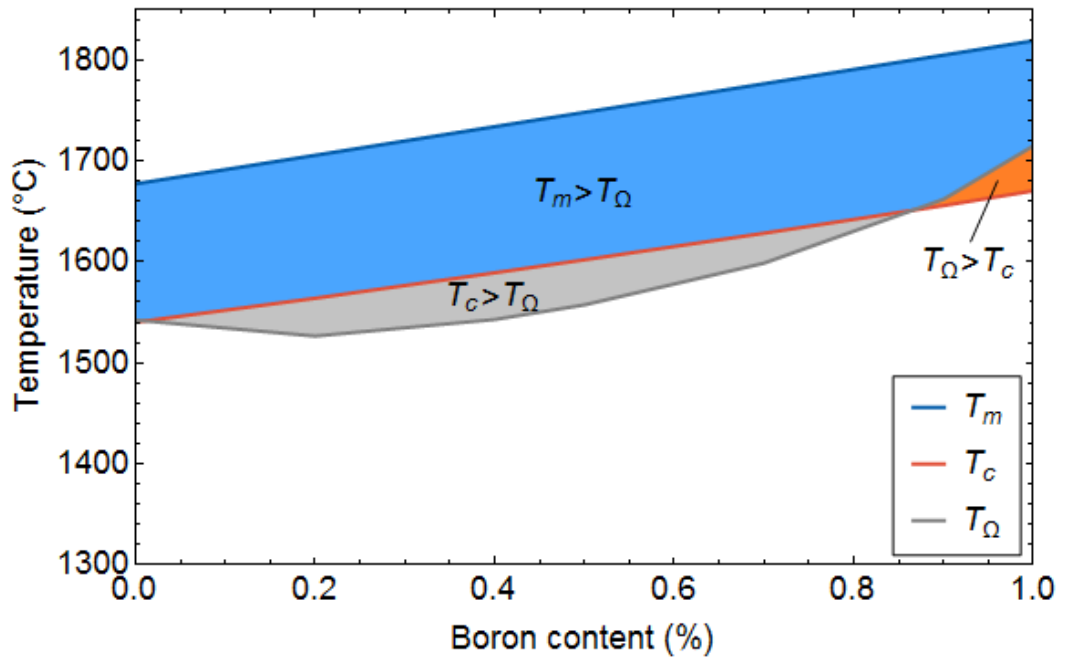


Figure 5.3:  $T_m$ ,  $T_c$  and  $T_\Omega$  for the range of  $\text{FeCoNi}(\text{B}_x\text{Al}_{1-x})_{0.1}\text{Si}_{0.1}$  compositions where the blue, orange and grey regions indicate areas where  $T_m > T_\Omega$ ,  $T_\Omega > T_c$ , and  $T_c > T_\Omega$  respectively. Values of  $T_c = T_m - \Delta T_c$  are obtained via Equation 5.1. (a)  $T_c$  values calculated based on  $X = 0.4$ , (b)  $T_c$  values calculated based on  $X = 0.23$ . Blue regions indicate the preference for formation of disordered structures, gray regions indicate the increase stability of metastable semi-ordered structures, while orange regions indicate the preferred formation of ordered structures. Figure 5.3 (b) is in better agreement with the XRD characterisation in Figure 5.2 compared to Figure 5.3 (a), and is suggestive of the increased metastability of HEAs

Comparing Figure 5.3(a) and Figure 5.3(b) with the experimental results as shown in Figure 5.2 suggested that Figure 5.3(b), which was plotted for values of  $X=0.23$  was in agreement with the experimental XRD results. This result validated our preliminary consideration where the binary Al-X pairs were considered to be dominant contributors to B2 stability.

From Figure 5.2, it was observed that the change in  $Fe_2B$  was constant a function to boron addition, but experienced a rapid change at higher alloying additions (which may be attributed to a possible segregation due to cooling effect of the as-cast alloy); the point at which this occurrence may be found by obtaining the inflection point for the change in volume fraction of the  $Fe_2B$  phase, which corresponded to 0.68%. Following the above discussion (*cf.* Figure 5.3), it can be proposed that  $T_c$  was equivalent to  $T_\Omega$  when the disordered structure was stabilised. This situation can be corresponded to the inflection point at boron content of 0.68%. Therefore, it was suggested that,  $X$  can be solved using a graphical solution, by changing values of  $T_\Omega(X)$  so that  $T_\Omega$  was equivalent to  $T_c$  at a boron content of 0.68%. Substituting the  $T_\Omega$  value into Equation 5.1 returns  $X = 0.25$ , which was in very good agreement with the approximated value of  $X = 0.23$ .

The reduction of the  $X$  value from the typical value at which  $X=0.4$  was correlated to a decrease in nucleation cluster size, which might be resulted by the inherent metasability of the HEA structures (since for the near-ideal solid-solution of each individual atom may still be preferred to form bonds with other atoms that may not be its immediate neighbours, and the cluster thickness which is required to initiate nucleation will be smaller than that of a one-component phase).

In Figure 5.3 (b) at which  $X=0.23$  was plotted for  $T_c$ , it can be seen for the B0 composition that as the solid cooled down, solidification started to occur once the

temperature reduced to lower than  $T_m(B0) = 1677K$ . Since  $T_c(B0) = 1548K$  and  $T_\Omega(B0) = 1542K$ , there was insufficient driving force for the precipitation of a secondary structure.

However, for the B0.5 composition, once the molten cooled and passed the melting temperature where  $T_m(B0.5) = 1706K$ , values of  $T_c(B0.5) > T_\Omega(B0.5)$  at 1576K and 1611K, respectively. This result signified that the metastability limit was higher than the temperature at which the contribution from the mixing entropy was equivalent to the enthalpy of mixing. Therefore, it was suggested that a secondary metastable phase (that was still partially in partially solid solution) could be formed due to the stabilising effect of entropy above the metastability limit. This finding was confirmed with the presence of the B2 structure in B0.5 alloy.

Finally, for the B1.0 composition, the metastability limit,  $T_c(B1.0) = 1678K$  was lower than  $T_\Omega(B1.0) = 1714K$ , which described that below  $T_\Omega$ , a secondary structure may still form since the limits of  $T_c$  was not reached. However, without the stabilising effect contributed by  $T_\Omega$ , the secondary structure formed was unlikely to be a solid solution. This prediction was also supported by observed characterisation results, where the  $Fe_2B$  phase existed. The existence of the  $Fe_2B$  phase in small quantities for the compositions between B0 – B0.7 may be explained by the possible segregation due to cooling effects of the as-cast alloy.

### 5.4.3 Refinement of lamellar microstructure through boron addition

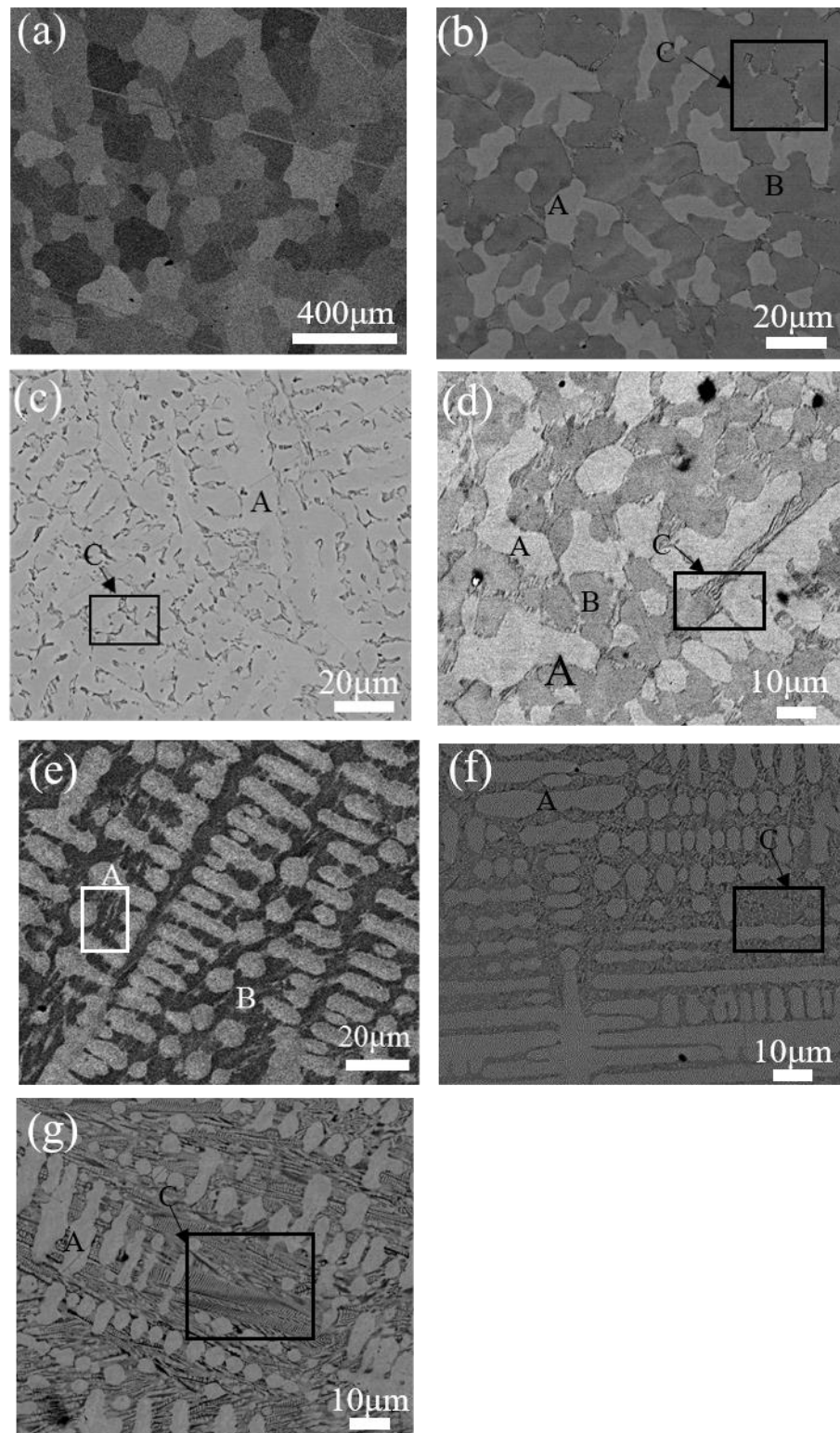


Figure 5.4: SEM images (backscattered mode) of  $\text{FeCoNi}(\text{B}_x\text{Al}_{1-x})_{0.1}\text{Si}_{0.1}$  lamellar structured HEA; (a)  $\text{FeCoNi}(\text{Al}_{0.1}\text{Si}_{0.1})$  HEA alloys, (b)  $\text{FeCoNi}(\text{B}_{0.2}\text{Al}_{0.8})_{0.1}\text{Si}_{0.1}$ , (c)  $\text{FeCoNi}(\text{B}_{0.4}\text{Al}_{0.6})_{0.1}\text{Si}_{0.1}$ , (d)  $\text{FeCoNi}(\text{B}_{0.5}\text{Al}_{0.5})_{0.1}\text{Si}_{0.1}$  and (e)  $\text{FeCoNi}(\text{B}_{0.7}\text{Al}_{0.3})_{0.1}\text{Si}_{0.1}$  (f)  $\text{FeCoNi}(\text{B}_{0.9}\text{Al}_{0.1})_{0.1}\text{Si}_{0.1}$ , and (g)  $\text{FeCoNi}(\text{B}_{1.0})_{0.1}\text{Si}_{0.1}$

The SEM backscattered electron images of the as-cast samples in Figure 5.4 (a) shows a polycrystalline structure composed of a simple BCC/B2 solid solution with grain size around 200-250 $\mu\text{m}$ . In order to clearly observe the morphology of the BCC/B2 which were coherently distributed in the FeCoNi(Al<sub>0.1</sub>Si<sub>0.1</sub>) alloy system, a higher magnification was used as shown in Figure 5.4(a).

Substitution of boron with aluminium in the B 0.2 composition in Figure 5.4 (b) showed a segregation of FCC and BCC/B2 phase, whilst the primary phase remained that of BCC/B2 solid solution. Regions marked as A and B in the figure represented the FCC solid solution and BCC/B2 phase while those regions marked as C represented the typical lamellar (eutectic like structures) that composed of the FCC solid solution and Fe<sub>2</sub>B-type intermetallic compound (as determined by XRD). However, a small volume fraction of lamellar microstructure was observed to nucleate and grow between the interdendrite (ID) regions. With increasing boron content from  $x= 0.2$  to 1.0, the volume fraction of this lamellar structure increased whilst lamellar spacing reduced. At  $x= 1.0$ , the solid solution (A) and the lamellar structure (C) dominated, while BCC/B2 phase was diminished. It can be summarised that the introduction of boron changed the morphology of the alloy system from single BCC/B2 phase ( $x = 0$ ) to lamellar structure consisting of FCC and Fe<sub>2</sub>B ( $x=1.0$ ) as a function of boron content. The micrographs of FeCoNi(B<sub>0.9</sub>Al<sub>0.1</sub>)<sub>0.1</sub>Si<sub>0.1</sub> and FeCoNi(B<sub>1.0</sub>)<sub>0.1</sub>Si<sub>0.1</sub> in Figure 5.5 corresponded to  $x = 0.9$  and 1.0 respectively showed unique herring-bone like pattern of fine lamellar structure.

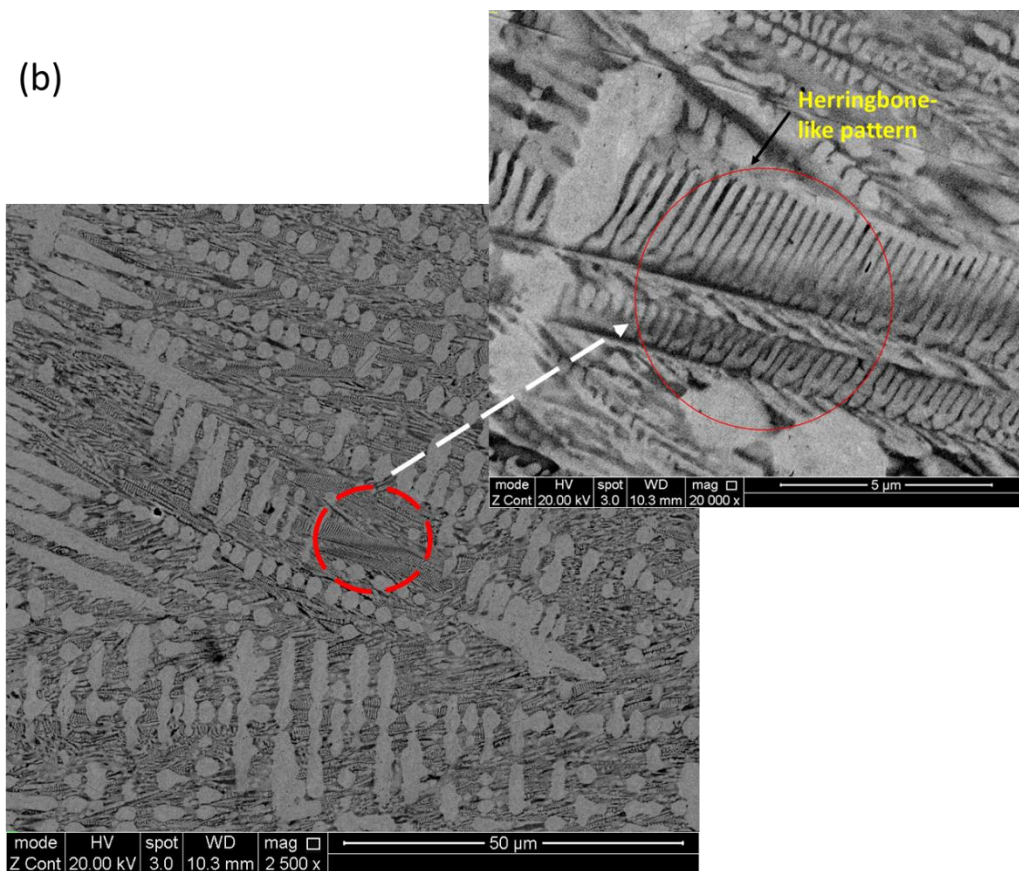
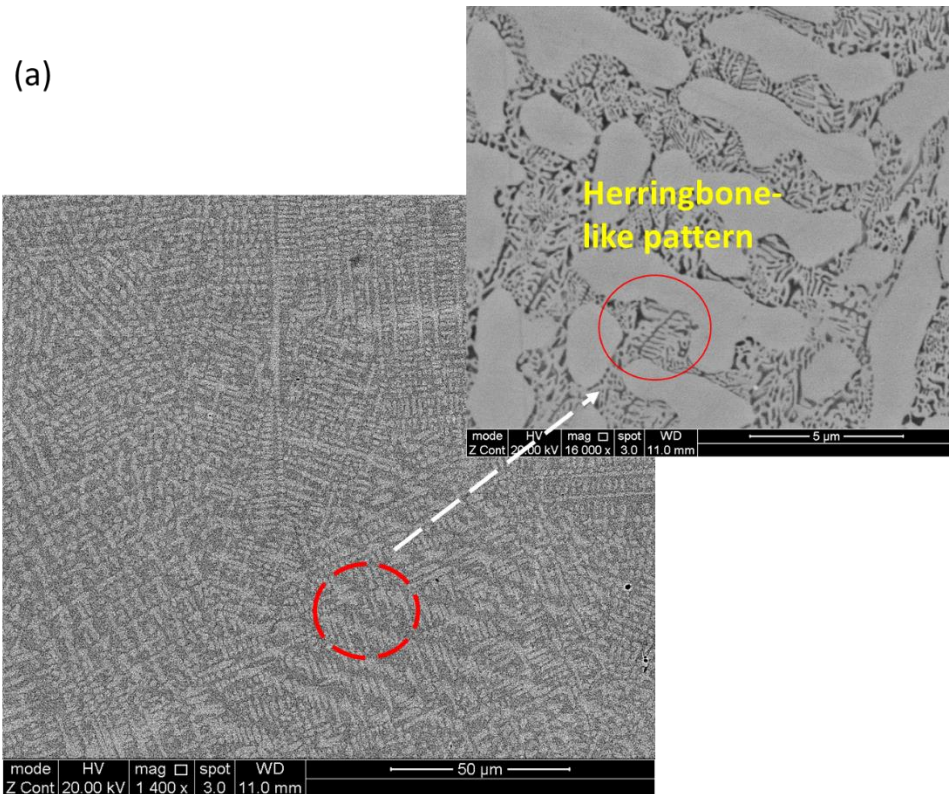


Figure 5.5: Herringbone-like pattern in (a)  $\text{FeCoNi}(\text{B}_{0.9}\text{Al}_{0.1})_{0.1}\text{Si}_{0.1}$  (b)  $\text{FeCoNi}(\text{B}_{0.1})_{0.1}\text{Si}_{0.1}$  HEA

Almost similar like pattern was observed in EHEAs studies of  $\text{CoCrFeNiMnPd}_x$  which mentioned as seaweed eutectic dendritic pattern [181]. It has been claimed that, the pattern was formed due to enrichment of the solute in front of the interface, resulted in instability of eutectic interface. Moreover, the sluggish diffusion effect in HEAs changed the interface significantly from the local non-equilibrium condition and the alternating pattern could result in weak interface energy anisotropy [174]. The formation of the coarse-grain structure corresponds to the BCC/B2 phase along with an alternating lamellar arrangement of FCC and  $\text{Fe}_2\text{B}$  phase, following a eutectic-dendritic-like pattern, as observed in the alloys.

Furthermore, the formation of coarse grain structure signifying the BCC/B2 phase along with the alternating lamellar arrangement of FCC and  $\text{Fe}_2\text{B}$  phase, namely a eutectic-dendritic pattern occurred during the alloy solidification process. During arc melting, the solidification of the alloy molten alloy started from the wall of cold copper crucible and continued inward. Normally, in the undercooled molten situation, the growth velocity was in the same direction as heat diffusion. However, the heat diffusion might result in instability of interface for the eutectic-dendritic structured formation [194]. In the current study, a depletion of solid solution which formed dendritic pattern in front of the interface resulted in instability of the lamellar structure. This depletion is correlated to the substitution of aluminium with boron induced the competition between two cooperative phases which leads to the formation of the observed microstructure.

#### **5.4.4 Interfacial energy of the alloy systems**

The formation mechanism in EHEAs has been reported by a number of previous works [174, 181] which was found to be related to the interfacial energy from the alternating structure arrangement. The energy used for chemical reordering in any

system (previous correlated to the formation of the lamellar-like microstructure) cannot exceed the driving force of the system. As such, it is expected that the formation of certain microstructural features should link clearly with this interfacial energy term. In the present work, the interfacial energy,  $\sigma$  (the excess energy in the system that is associated with the formation of an interface between two co-existing phases) could be assessed from the lamellar spacing data. The energy might be calculated according to the following equation [195, 196]:

$$\sigma = \frac{D\Delta H_v\Delta T}{4T_E} \quad \text{Equation 5.3}$$

where  $D$  is defined as the combined width of interlamellar spacing of FCC and Fe<sub>2</sub>B lamellae,  $T_E$  is equilibrium temperature in K (in this work it was defined as melting temperature),  $\Delta H_v$  is change in enthalpy per unit volume of each phases, and  $\Delta T$  is the undercooling temperature.  $\Delta T$  values were obtained from Equation 5.1 as discussed previously. Figure 5.6 shows a graph of interlamellar spacing and boron addition as function of the interfacial energy. The fine lamellar spacing and the grain sizes were measured by the Image J software.

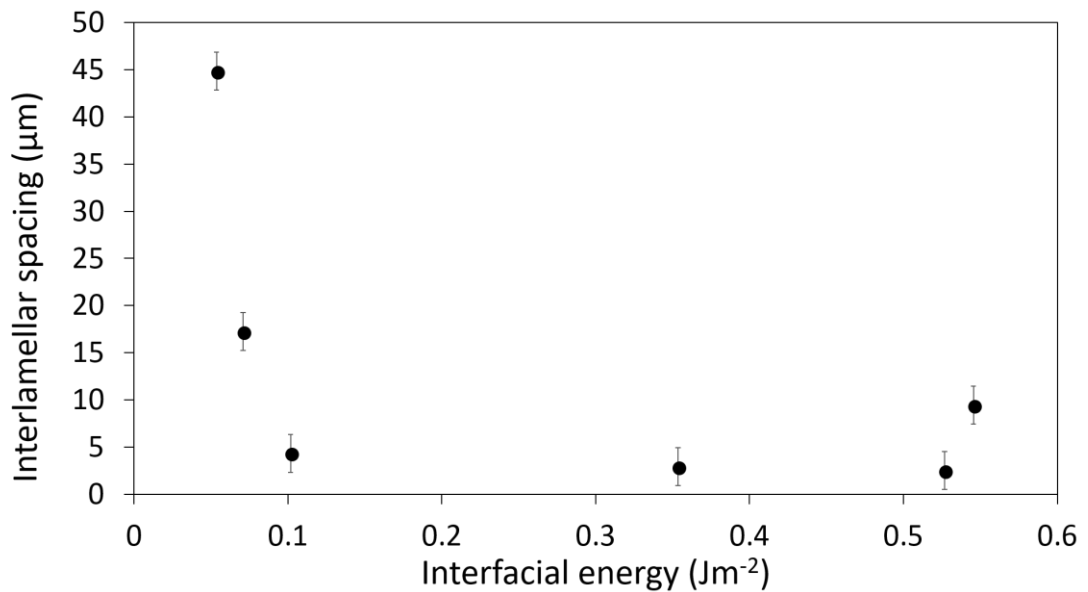


Figure 5.6: Interfacial energy as a function of boron addition

Figure 5.6 shows a graph of interlamellar spacing and boron addition as function of the interfacial energy, and calculated values of the interfacial energy are found to be similar in magnitude to those reported in the literature [43, 44]. As shown in Figure 5.6, interfacial energy decreases with increasing boron addition (which also corresponds to a decrease in the lamellar spacing). Theoretically, the interfacial energy comes from chemical and structural (strain) components, which result in distinct types of interfaces: coherent, semi-coherent and incoherent between a secondary phase and the matrix. Interfacial energies associated with incoherent phases are typically greater than semi-coherent and coherent structures, which are also attributed to disordered structures [45].

Higher values of interfacial energy may be associated with an increase in disorder in the structure. The precipitation of the ordered Fe<sub>2</sub>B structure on boron addition is in agreement with this, and suggests that the precipitation of an ordered structure in HEA alloys may act as a pathway for the reduction of the energy in the system that may result from the addition of many principal components as the interface plane may possess very different atomic configuration in any two adjacent solid-solution phases [46]. This is in good agreement with the XRD results, where the disordered BCC solid solution is completely present in the B0 composition, with Fe<sub>2</sub>B and FCC structures appearing with increasing boron addition. Additionally, a transition point may be correlated to the change in gradient of the interfacial energy, corresponding to boron addition of 0.7 which is in excellent agreement with the analysis obtained using T<sub>c</sub> as outlined above. It must be noted that both previously experimentally and theoretically determined stability points (0.68 and 0.71 boron addition, respectively) lie within this range.

The change in interfacial energy also leads to the formation of lamellar-like structures which widths might be controlled through the addition of B. As the various criteria used to derive the interfacial energy might be obtained from analysis of the critical metastability temperature of the compositions, this analysis may lead to a pathway for the design of HEAs with lamellar-like structures that can be used to tune their mechanical properties.

## 5.5 Conclusions

In current work, a new  $\text{FeCoNi}(\text{B}_x\text{Al}_{1-x})_{0.1}\text{Si}_{0.1}$  HEA was designed and produced. The lamellar structured solidification pattern was experimentally characterized and theoretical analysed. Furthermore, the metastability of undercooling HEA and interfacial energy correlated to interlamellar spacing of the alloy with boron addition were discussed. Our main conclusions were drawn as followed:

1. XRD analysis showed a substitution of boron with aluminum reduced the BCC/B2 phase and increased FCC phase up to a certain point after which the microstructure which was significantly dominated by FCC and  $\text{Fe}_2\text{B}$  phase.
2. SEM images showed the distribution of the lamellar structured HEA with the addition of boron that originated from the single-phase BCC/B2. With the increase in boron content, the volume fraction of lamellar spacing increased while the lamellar spacing decreased. The unique herring-bone like solidification pattern was clearly observed at  $x = 1.0$ .
3. Interfacial energy calculated for the disordered structures was found to be higher than the ordered structures, which was in agreement with the XRD result and high interlamellar spacing, resulted in high interface energy.

4. The metastability studies of this alloy composition indicated that the addition of boron reduced the stability of solid solution thus promoted the formation of secondary phase in the alloy.

## CHAPTER 6

### Mechanical properties of Lamellar-structured High Entropy Alloys

#### 6.1 Abstract

In the present work, effects of phase constitution on the mechanical properties of  $\text{FeCoNi}(\text{B}_x \text{Al}_{1-x})_{0.1}\text{Si}_{0.1}$  (where  $x = 0, 0.2, 0.4, 0.5, 0.7, 0.9$  and  $1.0$ ) are denoted as B0, B0.2, B0.4, B0.5, B0.7, B0.9 and B1.0 respectively) high-entropy alloys (HEAs) was investigated by various characterisation methods. It was found that, boron-free alloy which composed of solid solution BCC/B2 phase provided the highest yield strength (1800 MPa) and hardness (HV 682) but limited plasticity (2.8%). The substitution of boron changed the phase constitutions which then improved the mechanical properties of this alloy. The lamellar structured HEA possessed the highest yield strength of 1600 MPa and plastic strain of 5% at B1.0. However, the largest plasticity of this alloy might be attained at B0.4 which exhibited 24.9% of ductility that trade-off the yield strength (680MPa). The microhardness reduced from HV681.65 to HV630.15 with the addition of boron content. The solid-solution strengthening of the FCC and BCC/B2 matrix and the  $\text{Fe}_2\text{B}$  phase hardening were the two main factors that strengthened the alloys. Nanoindentation measurements along with the indents morphologies distinguished the hardness of different phases in the alloy by measuring the effect of the indentation size. Evidences from the results supported that the addition of boron into the single phase HEA with the formation of lamellar structure could provide a balance in strength-ductility in this alloy.

**Keywords:** Mechanical properties; Microhardness; Nanoindentation; Strength-ductility

## 6.2 Introduction

Conventionally, numerous common alloys including Fe-based, Ti-based or superalloys with addition of minor alloying elements have been commercially used in many advanced applications. However, the properties will always rely on the main elements. An alternative way in alloys development has been emerged since an interest in exploring a central phase region of the phase diagram where alloys with different components in equal atomic proportion was investigated by Cantor and Yeh. Based on thermodynamic concept, a maximum value of configurational entropy obtained when all elements involved are in equal atomic proportion ( $\Delta S_{\text{conf}} = -R(X_A \ln X_A + X_B \ln X_B)$ ) and subsequently increase with increasing number of elements in the system ( $\Delta S_{\text{conf}} = R \ln N$  where  $N$  is the number of elements). Interestingly, instead of predicted complex alloy, a simple solid solution alloy was obtained with improved properties compared to conventional alloys. Thus, a term of high entropy alloys has known as a new class of materials have shown promising potential for applications such as in structural, transportation, tool and coating.

Most of the reported studies on HEAs have mainly been focused on successful formation of single phase solid solutions [14, 130, 199]. HEAs with FCC structure mostly possess good ductility but lower strength, while BCC-types exhibit higher strength with limited plasticity [126]. To that end, extensive studies have been targeted to improve a balance of mechanical behaviours of HEAs. For example, Borkar *et al.* noted a balance of strength and ductility for HEAs with a composite structure comprised of a disordered solid solution phase and ordered precipitate phase [200]. In addition, previous studies have reported that eutectic HEA alloys with alternating soft FCC and hard BCC have an exceptional combination of high fracture strength and excellent tensile ductility at both room and elevated temperatures [201]. Moreover, the

lamellar nature of these eutectic structures also requires low energy phase boundaries, and implies high temperature creep resistance, better castability and controllable microstructure [173].

To develop multiple phase HEAs for optimised mechanical behaviour, a detailed understanding of microstructure formation and evolution is crucially required. One approach that has been employed for this work is through computer-aided thermodynamic calculations. He *et al.* [128] used this method to design a eutectic high entropy alloy (EHEA), where a modification of a single phase HEA composition into the eutectic alloy was performed via a careful selection of alloying elements. Binary phase HEAs can be designed by selecting an alloying element with a low enthalpy of mixing and large difference in atomic size, in order to induce precipitation of a secondary phase, resulting in alloy strengthening [177, 202]. This condition follows a manipulation of microstructure requires a measured change in processing parameter, or chemical composition.

Boron is one of commonly used micro-alloying elements in steels for improving hardenability [203]. Boron possesses a well-known grain-refinement effect when used as an alloying addition to several systems and also have a potential to provide a strengthening effect on the grain boundaries, which can increase ductility and reduce intergranular fracture [204]. Furthermore, boron addition is acknowledged in stabilising the lamellar microstructure that has been shown to be desirable in HEAs [128, 173]. Introducing boron which is classified as a metalloid element can be considered as a promising strategy in order to tune the mechanical properties through microstructural modification and refinement.

As subsequent studies from chapter 5, this chapter investigated the mechanical properties of the lamellar structured HEA and the effect of the phase and morphology

on the properties of the alloy. The lamellar structure of the studied FeCoNi(B<sub>0.05</sub>Al<sub>0.05</sub>)Si<sub>0.1</sub> demonstrated a combination of high yield strength of 1550 MPa with good ductility (20% in compression). As expected, the mechanical properties of these alloys are strongly affected by the microstructure and phase present.

### 6.3 Experimental procedure

The series of lamellar structured HEA of FeCoNi(B<sub>x</sub>Al<sub>1-x</sub>)<sub>0.1</sub>Si<sub>0.1</sub> (where x = 0, 0.2, 0.4, 0.5, 0.7, 0.9 and 1.0 at%) denoted as B0, B0.2, B0.4, B0.5, B0.7, B0.9 and B1.0 respectively) were produced using vacuum arc melting.

Compressive tests were carried out by Zwick compression machine using 3 mm x 6 mm cylindrical samples at room temperature at a strain rate of  $1.6 \times 10^{-3} \text{ s}^{-1}$ . Hardness measurements were conducted by a Mitutoyo HM-101 microhardness indenter under a load of 1 kg for 15s of dwell times. The hardness measurement was repeated for 10 readings of each sample. Nanoindentation was carried out using TI Premier Nanoindentation tester (equipped with scanning probe microscope) fitted with a Berkovich diamond tip to determine the hardness for each phase in the alloys. The test method was performed in an array of 3 x 3 indents within 50 $\mu\text{m}$  x 50 $\mu\text{m}$  sample area, each performed to a peak force of 4mN. The indented samples were then cleaned using acetone and were observed under optical microscope for image analysis.

## 6.4 Mechanical properties

### 6.4.1 Strength and ductility change with boron addition

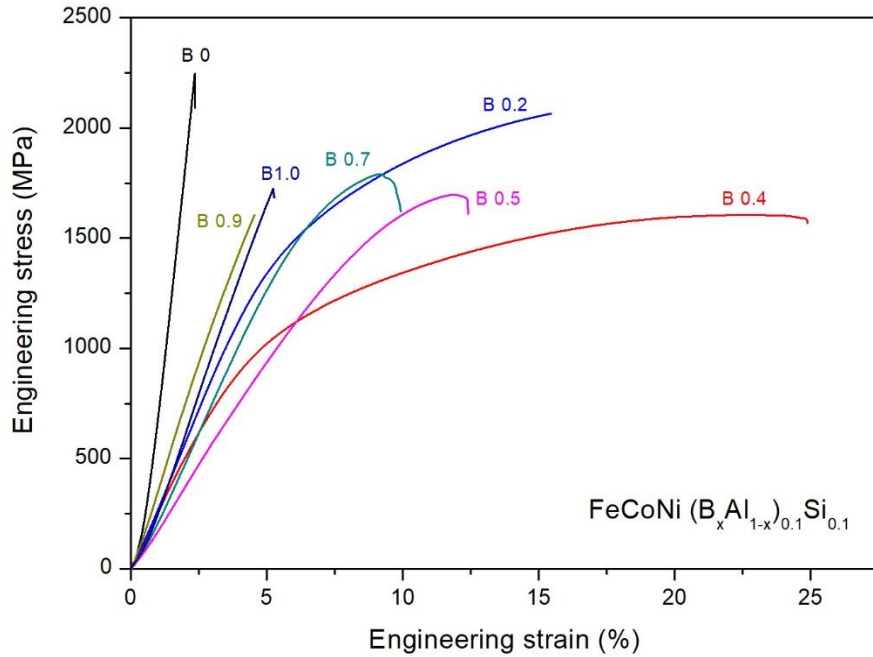


Figure 6.1: Engineering stress-strain curves of FeCoNi (B<sub>x</sub>Al<sub>1-x</sub>)<sub>0.1</sub>Si<sub>0.1</sub> alloys at room temperature, obtained from compression testing

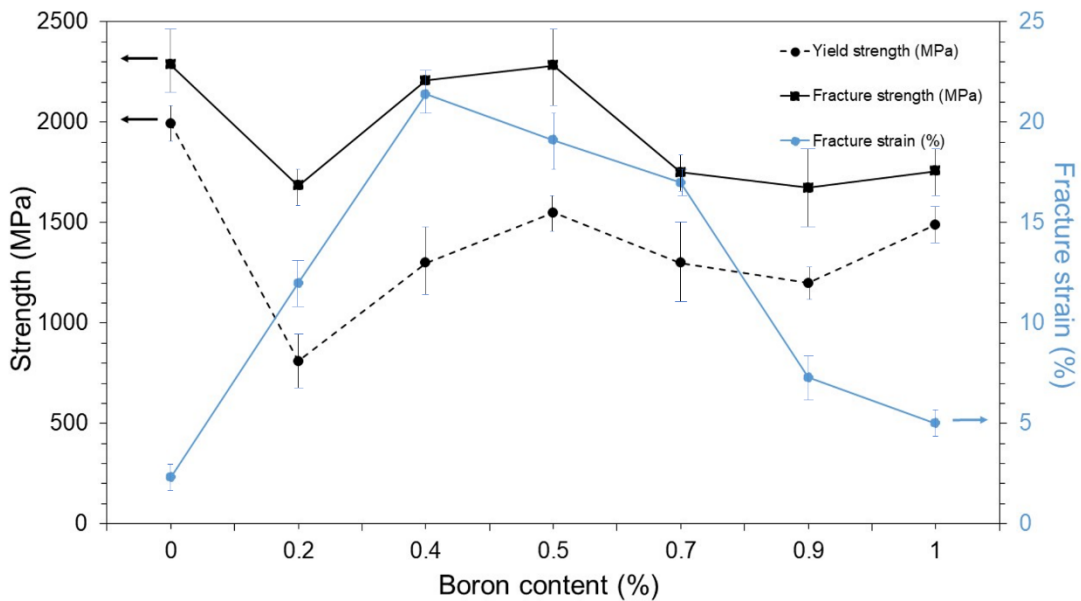


Figure 6.2: Compression engineering stress-strain curves of FeCoNi (B<sub>x</sub>Al<sub>1-x</sub>)<sub>0.1</sub>Si<sub>0.1</sub> alloys at room temperature

Lamellar structured HEAs, composed of alternating Fe<sub>2</sub>B and FCC structures were proposed in this work to tailor the mechanical properties of BCC/B2 structure in FeCoNi(Al<sub>0.1</sub>Si<sub>0.1</sub>) HEA. Results for compressive strength performed at room temperature for the alloy systems can be seen in Figure 6.1 and the results was then plotted in Figure 6.2 to perceive a correlation of corresponding yield strength, fracture strength and fracture strain for all compositions. As shown in Figure 6.2, the boron-free alloy showed a highest yield and fracture strength yet a very low plastic strain which indicated a typical behaviour of fully intermetallic (IM) phase (good strength but poor ductility). As boron content increased up to 0.4, the yield strength significantly decreased from 1800 MPa to 1080 MPa; however, plastic true strain to failure increased significantly from 2.4% to 24.9%. This behaviour might be explained by the change in structure from single BCC/B2 phase to lamellar phases composed of hard and brittle intermetallic B2 phase and strong and ductile FCC solid solution phase. Interestingly, a maximum compressive ductility was attained at x = 0.4 which were considered as a trade-off the yield and compressive strength of the alloy. This stimulating phenomenon might be attributed by two reasons: on one hand, volume fraction of FCC phase in the alloy was the highest among all compositions of alloys involved (as shown in Figure 5.2) which became a primary phase replacing the brittle BCC/B2 phase. Besides, the combination of adjacent large dendritic structure formed long FCC dendrites (as shown in Figure 5.4). Therefore, the reduction of volume fraction of BCC/B2 and Fe<sub>2</sub>B phases decreased the yield and fractured strength of the alloy, meanwhile the increasing of FCC phase fraction resulted in increasing in plasticity in the FeCoNi(B<sub>0.4</sub> Al<sub>0.6</sub>)<sub>0.1</sub>Si<sub>0.1</sub> alloy.

A further increase in boron content from x = 0.4 to x = 0.7 resulted in increasing pattern of yield and fracture strength. However, both of the yield strength and fracture

strength suddenly decreased at  $x = 0.9$  which occurred due to complete replacement of the B2 phase with a  $\text{Fe}_2\text{B}$ -type structure. Moreover, the ductility of the alloys continuously decreased from 24.9% at  $x = 0.4$  to 4.55% at  $x = 0.9$ . This scenario was resulted by the large volume fraction of  $\text{Fe}_2\text{B}$  phase, promoting brittleness in this alloy. It was proven that a particular amount of boron provided different phases for certain composition thus offered a balance of ductility and strength for this alloy.

The compression strength and plastic strain of some reported HEAs with typical eutectic microstructure was summarised in Figure 6.3. Most of these alloys composed of FCC phase and intermetallic compound (for example Laves or  $\mu$  phase) that is promising to provide high strength and good ductility that depending on the microstructure of the alloy. Meanwhile, alloy which shown fully eutectic microstructure was denoted as 'Eutectic' in the Figure 6.3. Besides it was found that, most of EHEAs could reach a maximum compression strength and compression strain around  $\sim 2400$  MPa and  $\sim 20\%$  respectively (located in circle region in the figure). On the other hand, not all EHEAs possessed excellent mechanical properties. For example,  $\text{CoFeNiVMo}_x$  [205] and  $\text{CoFeNi}_2\text{V}_{0.5}\text{Nb}_x$  [206] EHEAs possessed high strength but poor ductility which might be caused by low solid solution strengthening effect in the alloy.

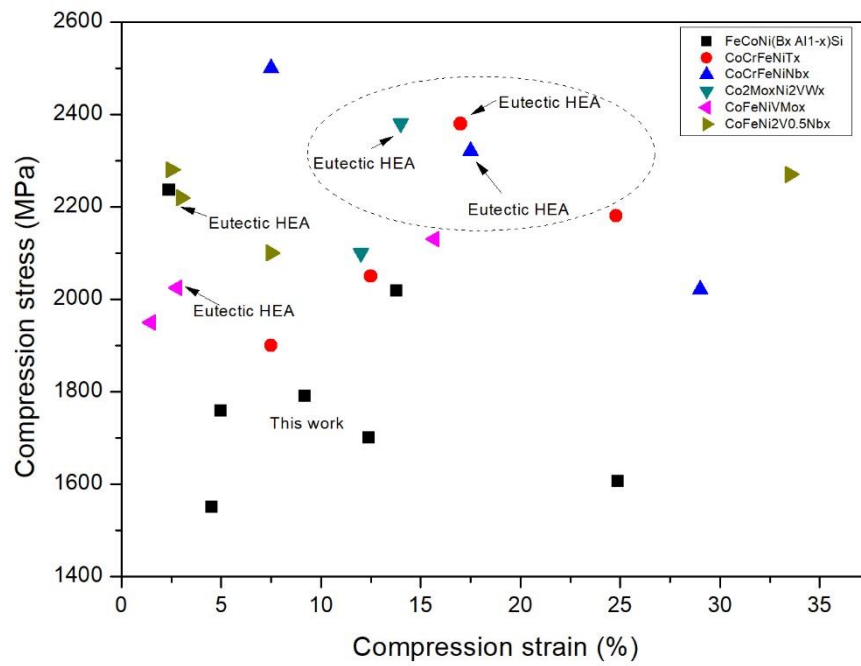


Figure 6.3: Compression strength and plastic strain of typical EHEAs under various strain rate: FeCoNi(B<sub>x</sub> Al<sub>1-x</sub>)<sub>0.1</sub>Si<sub>0.1</sub>, CoCrFeNiTa<sub>x</sub> [207], CoCrFeNiNb<sub>x</sub> [208], Co<sub>2</sub>Mo<sub>x</sub>Ni<sub>2</sub>VW<sub>x</sub> [205], CoFeNiVMo<sub>x</sub> [205], CoFeNi<sub>2</sub>V<sub>0.5</sub>Nb<sub>x</sub> [206]

#### 6.4.2 Deformation behaviour of lamellar structured HEA

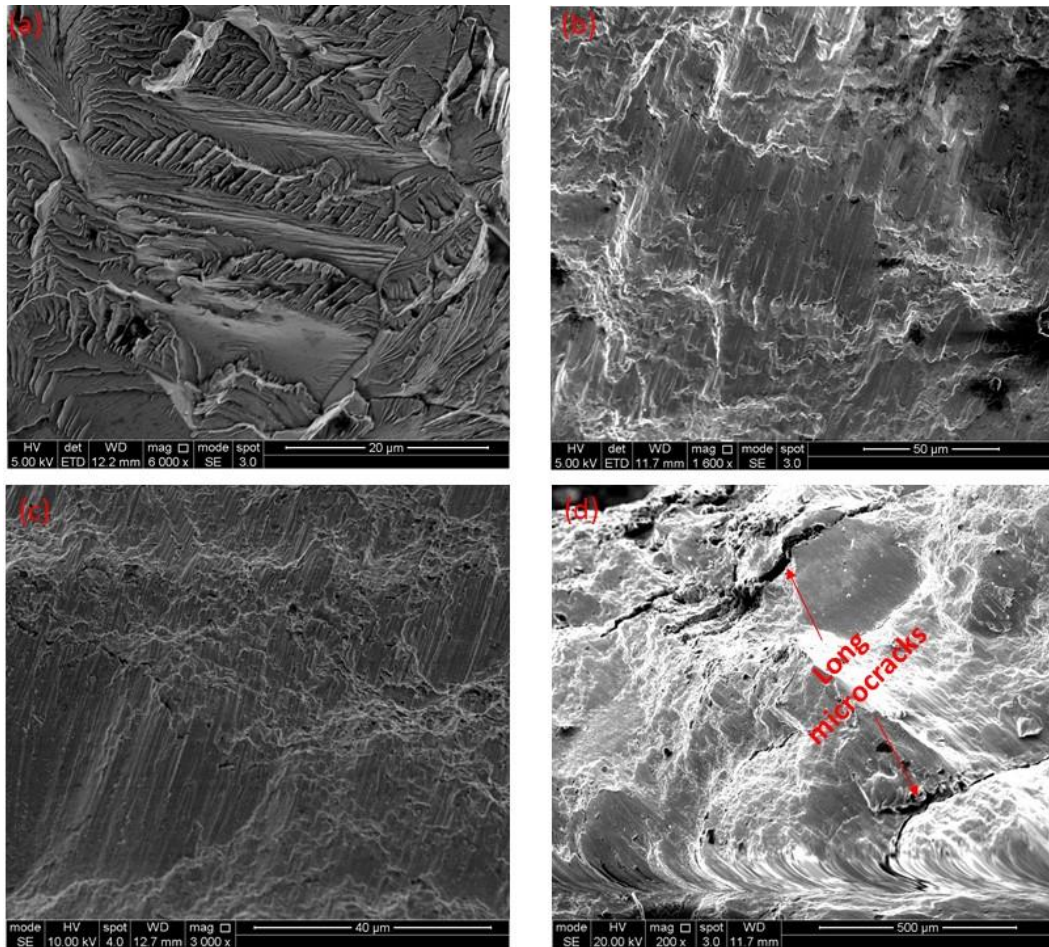


Figure 6.4: SEM images of compression fractured surface of  $\text{FeCoNi}(\text{B}_x\text{Al}_{1-x})_{0.1}\text{Si}_{0.1}$  (a)  $B = 0$ , (b)  $B = 0.2$ , (c)  $B = 0.4$  (d)  $B = 0.9$  at room temperature

Figure 6.4 shows the compression fracture morphology of the as-cast  $\text{FeCoNi}(\text{B}_x\text{Al}_{1-x})_{0.1}\text{Si}_{0.1}$  alloys at (a)  $B = 0$ , (b)  $B = 0.2$ , (c)  $B = 0.4$  (d)  $B = 0.9$  at room temperature. A boron-free alloy showed a typical river pattern of radiating parallel lines features, caused by a cleavage fracture mode which was absolutely a characteristic of a brittle fracture. The deformation of  $B = 0.2$  and  $B = 0.4$  alloys as in Figure 6.4 (b and c) showed a similar characteristics of quasi-cleavage fracture and torn edges with some shear band, indicated a mixture of brittle and plastic behaviour in the alloy. For the  $B = 0.9$  alloy, obvious cracks (marked with arrows) propagated along the lamellar phase, indicated that the alloy had a rather limited plastic strain

during the compression process, as shown in Figure 6.4 (d). The same deformation mechanism was observed in commonly reported EHEAs where the primary phase was dominated by hard and brittle phase such as IM (for example: Laves or  $\mu$  phase) or high strength solid solution phase (BCC/B2) [207, 209, 210]. This observation of different compression fracture surfaces of  $\text{FeCoNi}(\text{B}_x\text{Al}_{1-x})_{0.1}\text{Si}_{0.1}$  alloys was in agreement with the compressive test results as shown in Figure 6.2.

### 6.4.3 Hardness change with boron addition

As previously discussed, the  $\text{FeCoNi}(\text{B}_x\text{Al}_{1-x})_{0.1}\text{Si}_{0.1}$  alloys were composed of high strength phase (BCC/B2 and IM phase with  $\text{Fe}_2\text{B}$  structure) and high plasticity phase (FCC structure). The mechanical properties of each sample were different based on x value. Therefore, the mechanical properties of experimental alloys depended on the volume fraction and composition of each phase.

Microhardness testing was carried out and the result was listed in Table 6.1. It was predicted that the B0 alloy possessed highest hardness that was attributed by the fully BCC/B2 solid solution phase. The transformation of phases from BCC/B2 to FCC and  $\text{Fe}_2\text{B}$  phase at  $x = 0$  to  $x = 0.4$  resulted in a decrease in hardness from  $681 \pm 10$  Hv to  $527 \pm 5$  Hv. Nevertheless, with higher boron content from  $x = 0.4$  to  $x = 1.0$ , the hardness started to increase as FCC and  $\text{Fe}_2\text{B}$  lamellar structure took place while BCC/B2 structure reduced. In addition, this situation was also affected by a reduction in lamellar spacing. The trend of microhardness values with the increasing of boron addition was illustrated in Figure 6.5 (denoted with square black filled marker).

Table 6.1: Vickers hardness values for FeCoNi(B<sub>x</sub> Al<sub>1-x</sub>)0.1Si<sub>0.1</sub> with increasing boron content

Alloy	Hardness (HV)
B0	681±10
B0.2	597±8
B0.4	527±5
B0.5	546±3
B0.7	572±7
B0.9	600±8
B1.0	630±9

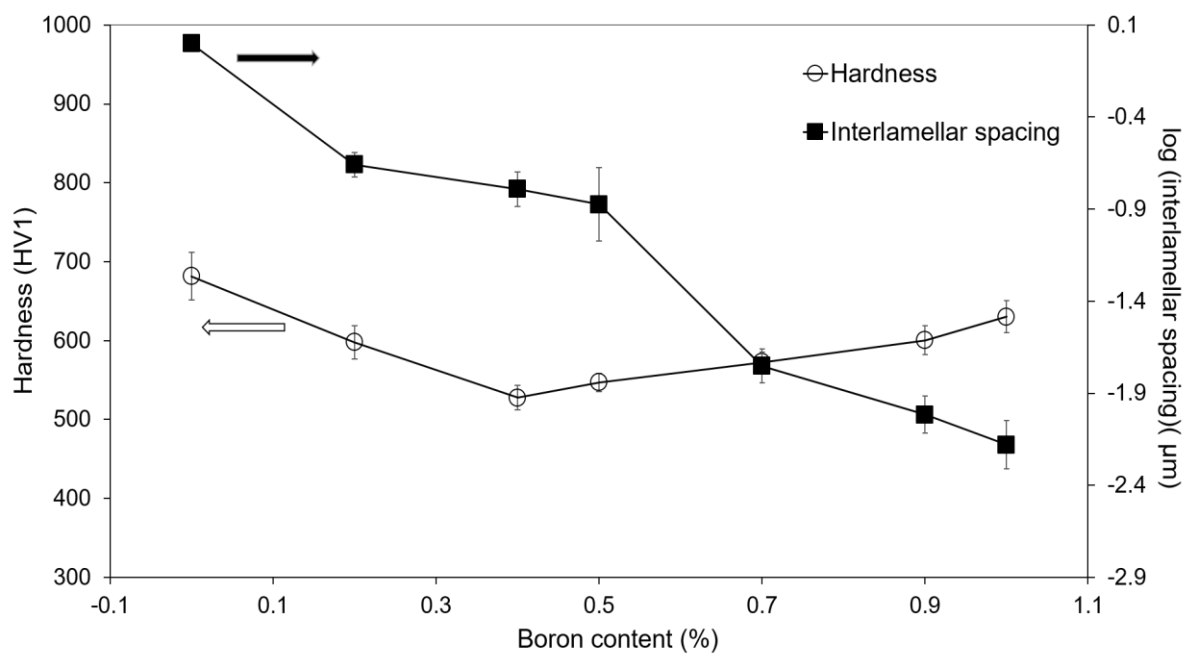


Figure 6.5: Effect of interlamellar spacing and boron content on the hardness of the alloys

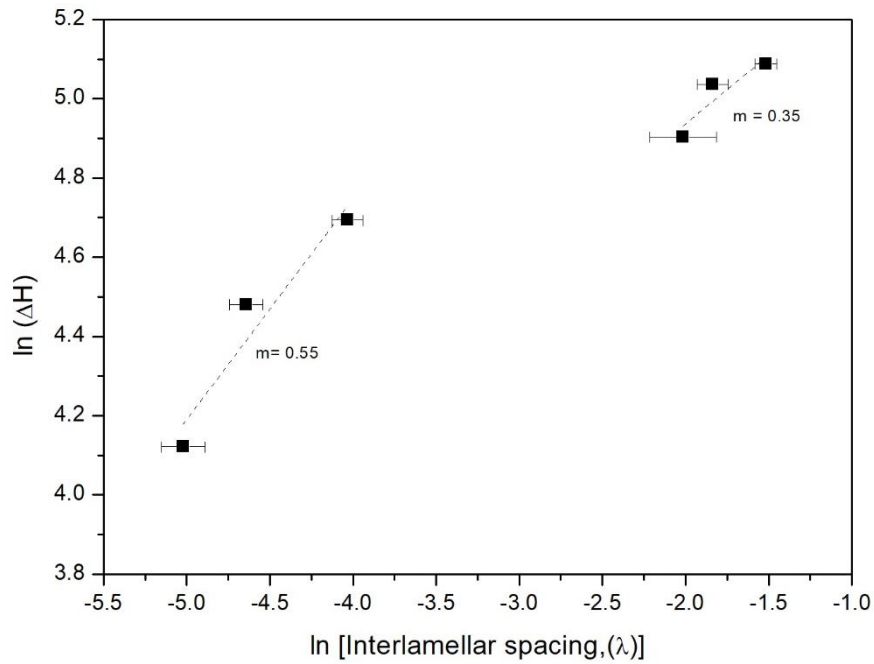


Figure 6.6: Hall-Petch plot of ln changed in hardness vs ln interlamellar spacing,  $\lambda$

The interlamellar spacing,  $\lambda$  were taken from 10-15 different regions of the samples in order to investigate the effect of interlamellar spacing with the increasing hardness of this alloy. The variation of microhardness as a function interlamellar spacing,  $\lambda$  and boron content was presented in Figure 6.5. Likewise, as boron content was increased, the interlamellar spacing decreased which resulted in an increase in microhardness. The Hall-Petch equation [211, 212] might be applied to relate the hardness with the lamellar spacing,  $\lambda$  from the alloy's microstructure as shown in Equation 6.1:

$$H_v = H_0 + k_1 \lambda^{-1/2} \quad \text{Equation 6.1}$$

where  $H_v$  is the hardness,  $H_0$  is a materials constant for the initial hardness at room temperature,  $k_1$  is the strengthening coefficient, and  $\lambda$  is the lamellar spacing. It was

reported that decrease in lamellar spacing of the alloys structure leads to an increasing in the microhardness [213, 214].

The equation was modified to perceive the relationship of the parameters with respect to the slope,  $m$  as summarised in equation 6.2:

$$\ln \Delta H = k - 1/2 \ln(\lambda) \quad \text{Equation 6.2}$$

where  $\Delta H$  is change in hardness. A linear regression analysis was performed with the changed in hardness and interlamellar spacing as illustrated in Figure 6.6.

As can be seen in Figure 6.6, two trend lines were developed in the graph which showed different hardness characteristics in the alloy. The slope of the graph from B0.2-B0.5 ( $m = 0.35$ ) indicated a significant difference with the theory of Hall-Petch equation ( $m = 0.5$ ) which indicated that the lamellar spacing was not the only key parameter that promoted the increase in hardness trends. This finding suggested that the hardness was also significantly influenced by the phases presented in the structure. In this case, the contribution of strong and brittle phase of secondary phases BCC/B2 and Fe<sub>2</sub>B phases also effected the hardness particularly at the turning point of  $x = 0.5$ - $0.7$ . This phenomenon was also supported by the interfacial energy analysis as shown in Figure 5.8 which related to the ordered disordered structure in the alloy in which the turning point from disordered to ordered structure occurred at  $x = 0.5$ . However, as boron was increased to B0.7, the interlamellar spacing became a dominant factor that contributed to the increase in hardness of the alloy. This scenario was in accordance with the slope value which was virtually similar to the theory of Hall-Petch ( $m = 0.5$ ).

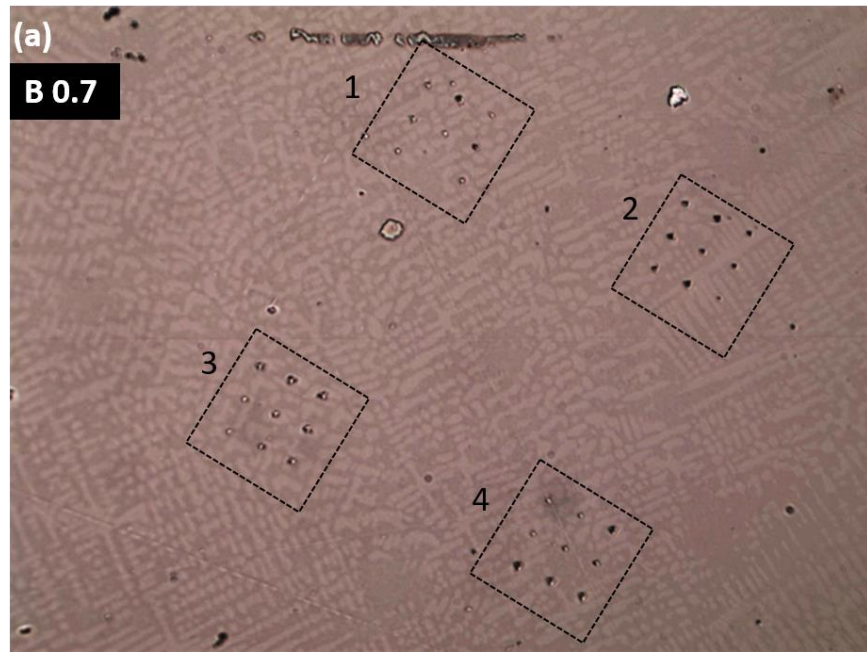
It was noteworthy that the load of microhardness in this study was 1 kg, indicated that the size of indentation was much larger than primary FCC phase, primary Laves

phase and lamellar structure. Besides, it was known that the microhardness reflected the average hardness of all phases in microstructure. Therefore, more accurate testing was carried out in the next section to know the average hardness of each phase in the microstructure.

#### **6.4.4 Nanoindentation and indentation size effect of different phases in the alloy**

In order to better investigate the relationship between boron content and mechanical properties of each phase, nanoindentation method was used to distinguish the hardness of the primary phase (BCC/B2 or FCC) and the lamellar structured phases (FCC + Fe<sub>2</sub>B). It was noted that the lamellar spacing in the alloy was relatively low (i.e. 0.1 - 4 μm). Therefore, the primary and lamellar phases was characterised by conventional nanonindentation method (using optical microscope as an observation technique). For this measurement, the B0.7 and B1.0 alloys were chosen due to the existence of all phases (BCC/B2, FCC and Fe<sub>2</sub>B phases) in B0.7 and only two phases (FCC and Fe<sub>2</sub>B) in B1.0 alloy.

Figure 6.7 (a) and Figure 6.8 (a) show the optical microscope image of the surface for the whole sample area (bound by 4 black rectangles) after the indentation test for B0.7 and B1.0 respectively. It can be seen that, the colour of dendritic FCC phase was lighter while the lamellar space containing FCC and Fe<sub>2</sub>B phases was much darker. However, the BCC/B2 phase in the B0.7 sample was hard to be distinguish using optical microscope due to low volume fraction which was only (7.12%) and low image contrast. The image of indented area (each rectangle) was then magnified to observe the indented marks that located in each phase which can be seen in Figure 6.7 (b) and Figure 6.8 (b).



(b)

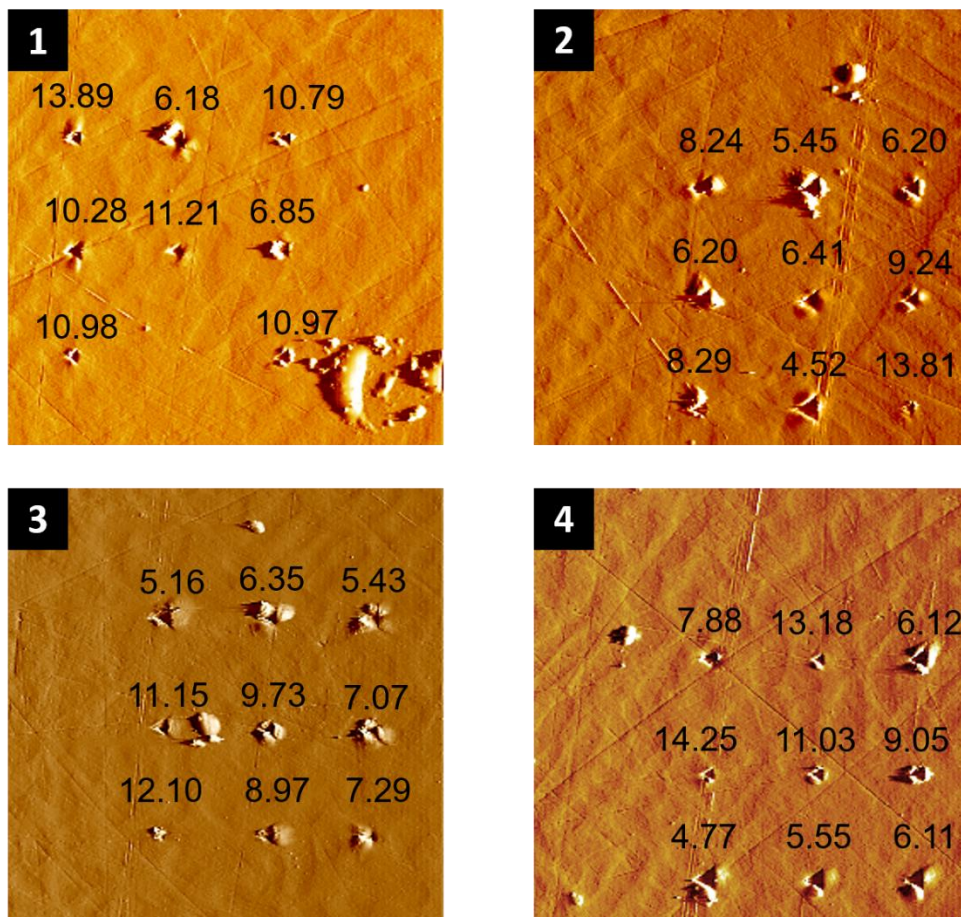
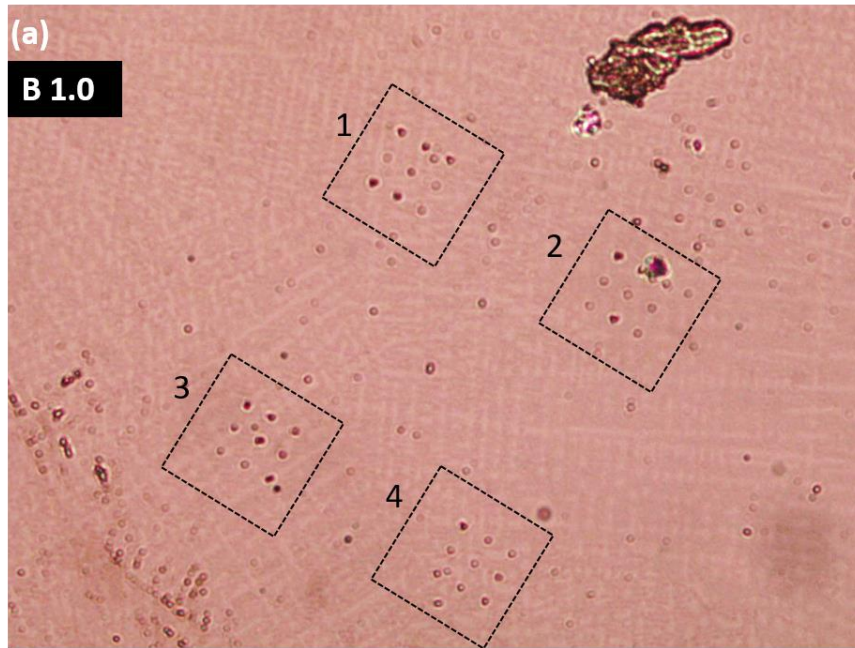


Figure 6.7: Optical microscope image of the sample surface after the indentation test of (a) the whole sample area, (b) magnified image of each indentation area with the hardness values in GPa (inside the dashed square region) of B0.7 alloy



(b)

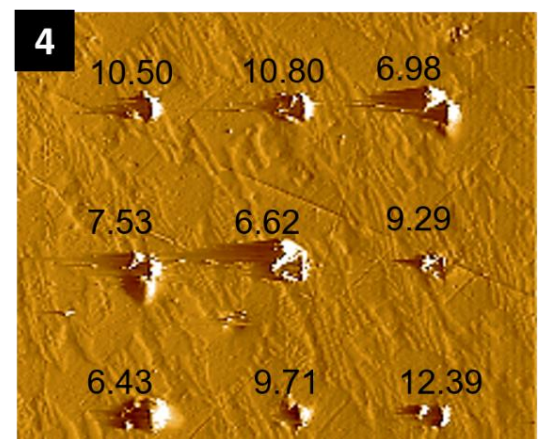
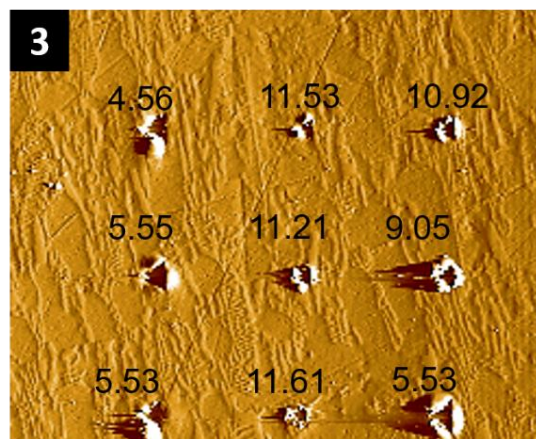
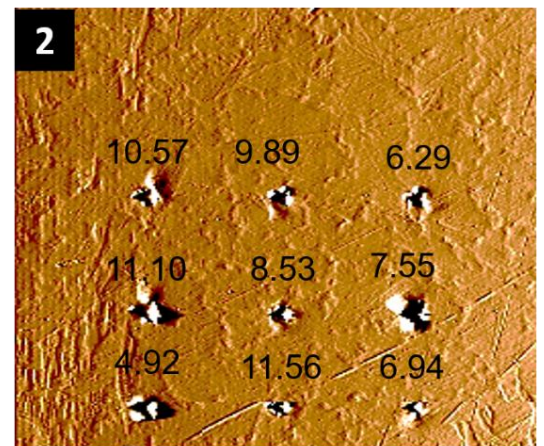
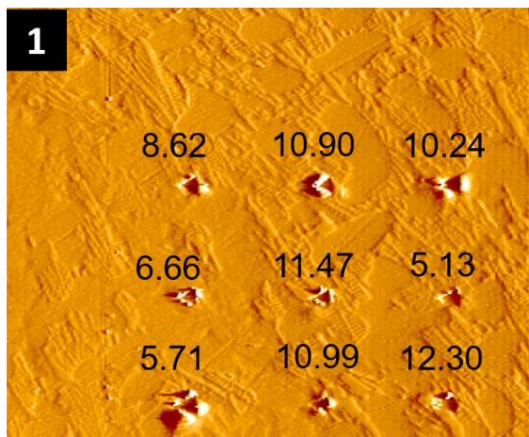


Figure 6.8: Optical microscope image from the sample surface after the indentation test of (a) the whole sample area, (b) magnified image of each indentation area with the hardness values in GPa (inside the dashed square region) of B1.0 alloy

Within each area bounded by the dashed black rectangle, there were 9 indentations with different indented size. From that image, smaller indent marks were observed which located at the lamellar structure while the larger indent marks could be seen at the primary FCC phase. Therefore, it can be deduced that the FCC phase was softer than the lamellar phase. The indentation size can be used to determine the hardness of a material which subjected to deformation as presented in Equation 6.3

$$H = \frac{P_{max}}{A_r} \quad \text{Equation 6.3}$$

where  $P_{max}$  is the maximum load while  $A_r$  is the indentation area. Therefore, according to the equation, it can be interpreted that the smaller indents can be seen in a hard materials than in a soft materials under a constant load.

This phenomenon was proved by the hardness obtained which was recorded during the test, (as shown in Figure 6.7 (b)). For B0.7, the lowest hardness was attained in the range of 4 to 7 GPa, which indicated the FCC phase while the highest hardness was recorded in the range of 10 to 15 GPa which exactly located at the lamellar region. This finding was in agreement with the work performed by Castro *et al.* who reported that hardness of Fe<sub>2</sub>B layers in tool borided steel, tested using Berkovich nanoindentation technique at 250 mN applied load was approximately 14 GPa, [215]. However, lower hardness was expected in this study due to low volume fraction of boron (< 0.1 at%) in the composition. Meanwhile the range of FCC phase was determined according to Almasri and Voyiadjis [216] who performed experimental studies on nanoindentation in FCC metal. The image of the indents also revealed that, there were some intermediate indents located between FCC and lamellar structure. The intermediate indents were expected to be BCC/B2 phase which gave the hardness in the range of 7 to 10 GPa which was out of the range between FCC and Fe<sub>2</sub>B phase.

The distribution of hardness on each phase for B0.7 sample was illustrated in Figure 6.8.

The same scenario can be seen in the B1.0 sample as displayed in Figure 6.8 (b). However, as the sample was only comprised of FCC and Fe<sub>2</sub>B phases, the hardness can be determined directly, either FCC or Fe<sub>2</sub>B phase. It was noted that the highest hardness up to 12.39 GPa was recorded. This situation was due to the absence of BCC/B2 phase in the alloy that resulted in lower hardness as compared to B0.7 alloy. The hardness distribution of B1.0 alloy was showed that the distribution of lamellar phase was higher than B0.7 sample (Figure 6.10). This condition was in accordance with the SEM images as illustrated in Figure 5.4. Besides, the hardness in the range of 7 to 10 GPa indicated the intermediate indents between FCC and lamellar phase. Table 6.2 shows the average of hardness of three different phases in this alloy (FCC, lamellar (FCC+Fe<sub>2</sub>B) and FCC/BCC + lamellar). It was shown that the average of FCC and lamellar phase for B0.7 and B1.0 was almost similar which were 5.78 and 5.70 and 12.14 and 11.89 GPa respectively. However, the significant differences of average hardness values can be seen for the intermediate phases (FCC/BCC + lamellar). This phenomenon might be due to the existence of hard and brittle BCC/B2 phases in the B0.7 alloy.

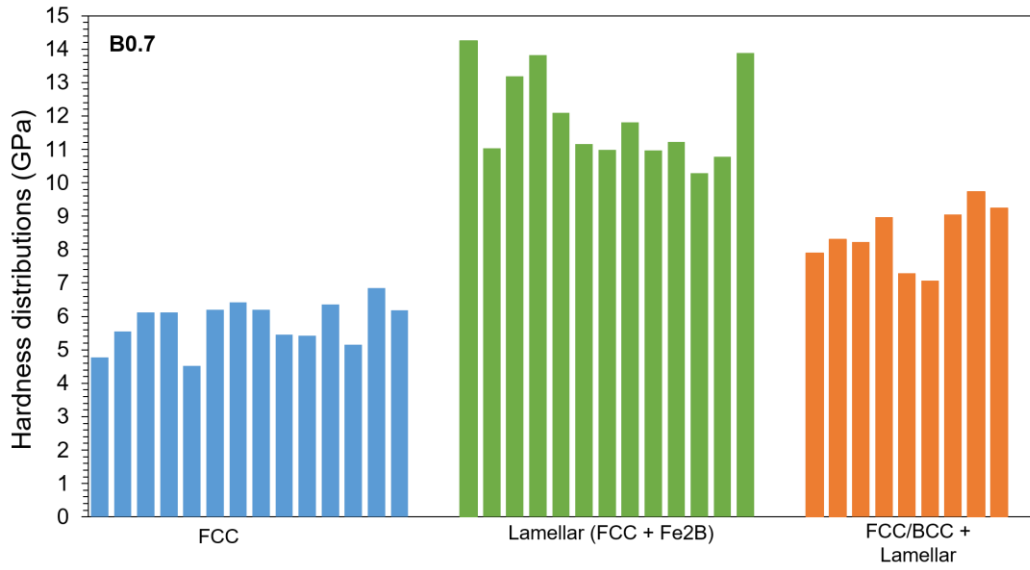


Figure 6.9: Distribution of hardness values of FCC, Fe<sub>2</sub>B and BCC/B<sub>2</sub> phases in B0.7 sample

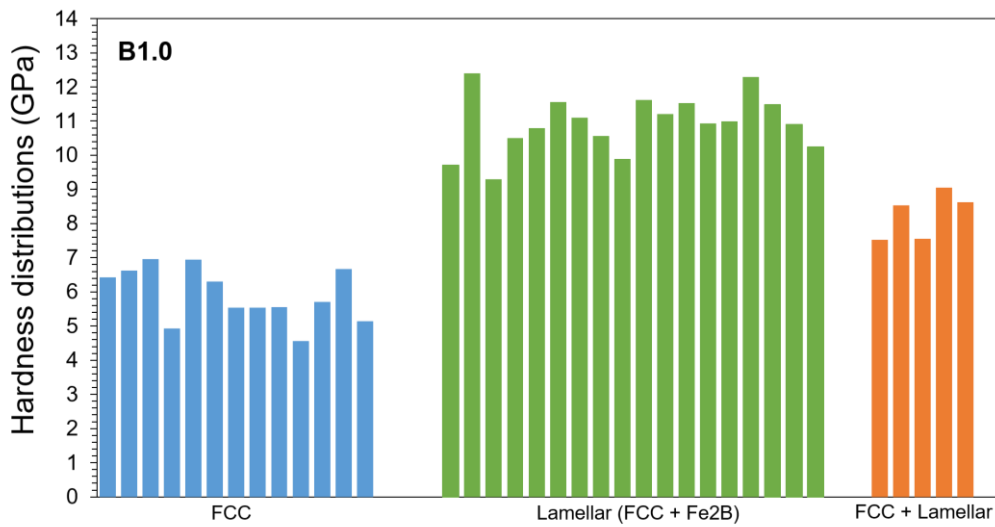


Figure 6.10: Distribution of hardness values of FCC, Fe<sub>2</sub>B and BCC/B<sub>2</sub> phases in B1.0 sample

Table 6.2: Average hardness of three different phases FCC, lamellar (FCC+Fe<sub>2</sub>B) and FCC/BCC + lamellar in B0.7 and B1.0

Sample	FCC (GPa)	Lamellar (GPa)	FCC/BCC + Lamellar (GPa)
B0.7	5.78±0.5	12.14±2.5	8.90±1.2
B1.0	5.70±1.5	11.89±2.0	8.16±0.3

## 6.5 Conclusions

1. Lamellar structured-high entropy alloys were designed to obtain a balance in strength and ductility for  $\text{FeCoNi}(\text{B}_x \text{Al}_{1-x})_{0.1}\text{Si}_{0.1}$  high entropy alloys where it can be tailored by modification of boron content.
2. The mechanical properties of the studied alloys were closely related to their structures. The optimum balance of strength (1550MPa) and ductility (19%) were attained at 0.5% boron content.
3. The microhardness varied with the change in the phase presented. Changes in BCC/B2 structure and the presence of lamellar structure affected the hardness in the alloys from B0 to B0.5 while the lamellar spacing possessed a significant effect of the hardness at B0.5 to B1.0.
4. Nanoindentation test along with the indent morphologies has distinguished the hardness of each phase in the alloy. The highest hardness by nanoindentation was 14.2 GPa which was indented at the lamellar structure belong to B0.7 sample.

## CHAPTER 7

### CONCLUSIONS AND RECOMMENDATIONS

The effort to study the phase transformation that occur in two types of HEAs; HE-BMG and lamellar structured HEA was considerably successful. In addition, the lamellar structured HEA was developed to improve the mechanical properties of single phase HEA. A number of the remarkable findings throughout this current work were summarised below:

- HE-BMG possessed better resistance to phase transformation compared to conventional amorphous alloys which was investigated by annealing process using DSC technique in isothermal and non-isothermal conditions. The analysis of activation energy presented using various analytical methods showed the growth process was more difficult than nucleation process for crystallisation stages. Meanwhile, average activation energy determined by Kissinger method in isothermal condition was lower than non-isothermal condition. This phenomenon explained, the energy barrier in non-isothermal condition was higher than isothermal annealing mode. The nucleation rate calculated from Avrami exponent,  $n$  showed slow nucleation process at higher annealing temperature in isothermal condition. This current work suggested that the crystallisation resistance that was perceived in this alloy at high annealing temperature provided the evidence for the sluggish diffusion kinetics. This finding was associated with the theory of sluggish diffusion in HEA principles.
- The addition of boron changed the phase formation, phase stability and morphology of FeCoNi(Al<sub>0.1</sub>Si<sub>0.1</sub>) single phase HEA alloy. The

substitution of boron with aluminum changed the BCC/B2 phase to FCC and Fe<sub>2</sub>B phase. The metastability studies calculated by theoretical critical metastability temperature indicated that the addition of boron reduced the stability of solid solution thus promoted the formation of secondary phase in the alloy. The predicted structural stabilities corresponded well to experimental results.

- The SEM micrograph showed a unique herring-bone like lamellar pattern was formed with increasing boron content. The interfacial energy evaluated from the lamellar spacing data signified the interfacial energy increases with increasing lamellar spacing and decreased as a function of boron addition where the disordered structures was found to be higher than the ordered structures, which was in agreement with the XRD result.
- Prior studies on FeCoNi(Al<sub>0.1</sub>Si<sub>0.1</sub>) HEA has showed that the single-phase BCC alloy possessed excellent mechanical strength but poor ductility. The addition of boron improved the mechanical properties through microstructural modification and refinement. The lamellar structured HEA also was designed in purpose to obtain a balance in strength and ductility for FeCoNi(B<sub>x</sub> Al<sub>1-x</sub>)<sub>0.1</sub>Si<sub>0.1</sub> alloy. The optimum balance of strength (1550 MPa) and ductility (19%) was attained at B0.5 sample. The hardness value was significantly affected by the phase changes in the alloy up to B0.5 and it was then influenced by the lamellar spacing from B0.5 to B1.0. Hall-Petch equation was employed to analyse this situation. The difference of the slope of the graph, *m* suggested that that hardness was not only influenced by the lamellar spacing but also the phases presented in the alloy.

## 7.1 Suggestions for Future Works

1. High throughput measurement can be employed to determine the crystallisation kinetics or diffusion coefficient of TiZrHfNiCu HE-BMG by using the recently developed numerical method such as numerical inverse method. Therefore, the reliability of the obtained experimental data can be confirmed by comparing the simulated diffusion profiles with the experimental measurement. Besides, interpretation of experimental crystallisation kinetics will be more beneficial with the detailed studies of microscopic observation (SEM or TEM). Therefore, nucleation rate and mode of growth can be clearly analysed on each crystallisation stages

2. Through adjusting the content of boron, fully eutectic structure can be obtained with promising mechanical properties. However experimental work is costly and very time consuming. Therefore, modelling of using thermo-calc software using SSOI database would be beneficial to determine the optimised composition to achieve fully eutectic structure HEA.

3. Investigate the effect of annealing temperature and annealing time on the phase transformation, morphology and mechanical properties of the  $\text{FeCoNi}(\text{B}_x \text{Al}_{1-x})_{0.1}\text{Si}_{0.1}$  lamellar structured HEA at cryogenic temperature.

4. The composition of  $\text{FeCoNi}(\text{B}_x \text{Al}_{1-x})_{0.1}\text{Si}_{0.1}$  lamellar structured HEA containing ferro-magnetic elements, it may have many interesting properties such as magnetic, resistivity and electrical conductivity. Therefore, the detail studies on the physical properties of this alloy may be beneficial to explore on this composition.

## 7.2 Contributions of Current Work

A studies of phase transformation occurred HE-BMG and lamellar structured HEA was successfully developed for advanced applications particularly at high temperature environment. In aerospace industry, sustainable engine parts i.e. turbines, compressors and fans require a material that can handle extreme working temperature. Therefore, this study provides a guideline for the phase stability and crystallisation mechanism of this alloy at high temperature applications. Besides, the development of lamellar structured HEA would be a potential candidate material for many structural applications that requires strength and ductility balance such as frames and casing.

### **PUBLICATIONS AND CONFERENCE PRESENTATION**

- 1) N.H.Nordin, H.Nan, H.Wang, J.Corteen, W.M.Rainforth, I.Todd. Study of Glass Forming Ability of Different Bulk Metallic Glass Alloys. In: USES 2015 - The University of Sheffield Engineering Symposium, 24 Jun 2015, The Octagon Centre, University of Sheffield.
- 2) N.H. Nordin, Leong Z., R. Goodall, I. Todd. *Design of novel lamellar-microstructured high entropy alloy via controlled boron addition*. 24th International Symposium on Metastable, Amorphous and Nanostructured Materials (ISMANAM 2017), June 18-23, 2017 Donostia- San Sebastian, Spain.
- 3) N.H. Nordin, Leong Z., R.Goodall, I. Todd. Design of Lamellar-microstructured High Entropy Alloys through Controlled Boron Additions (In-Peparation).

## References

1. *Metals Handbook: Properties and selection*. 10 ed. Vol. 2. 1990: ASM International.
2. D. Miracle, J. Miller, O. Senkov, C. Woodward, M. Uchic, J. Tiley. *Exploration and Development of High Entropy Alloys for Structural Applications*. Entropy, 2014. **16**(1): p. 494.
3. O. Senkov, G. Wilks, J. Scott, D. Miracle. *Mechanical properties of Nb 25 Mo 25 Ta 25 W 25 and V 20 Nb 20 Mo 20 Ta 20 W 20 refractory high entropy alloys*. Intermetallics, 2011. **19**(5): p. 698-706.
4. J.-W. Yeh, S.-J. Lin, T.-S. Chin, J.-Y. Gan, S.-K. Chen, T.-T. Shun, C.-H. Tsau, S.-Y. Chou. *Formation of simple crystal structures in Cu-Co-Ni-Cr-Al-Fe-Ti-V alloys with multiprincipal metallic elements*. Metallurgical and Materials Transactions A, 2004. **35**(8): p. 2533-2536.
5. F. Otto, A. Dlouhý, C. Somsen, H. Bei, G. Eggeler, E.P. George. *The influences of temperature and microstructure on the tensile properties of a CoCrFeMnNi high-entropy alloy*. Acta Materialia, 2013. **61**(15): p. 5743-5755.
6. C. Zhu, Z. Lu, T. Nieh. *Incipient plasticity and dislocation nucleation of FeCoCrNiMn high-entropy alloy*. Acta Materialia, 2013. **61**(8): p. 2993-3001.
7. K.A. Christofidou, E.J. Pickering, P. Orsatti, P.M. Mignanelli, T.J.A. Slater, H.J. Stone, N.G. Jones. *On the influence of Mn on the phase stability of the CrMnxFeCoNi high entropy alloys*. Intermetallics, 2018. **92**(Supplement C): p. 84-92.
8. M.C. Gao, J.-W. Yeh, P.K. Liaw, Y. Zhang. *High-entropy alloys: fundamentals and applications*. 2016: Springer.
9. C.S. Smith. *Four outstanding researches in metallurgical history*. 1963.
10. B. Cantor, I. Chang, P. Knight, A. Vincent. *Microstructural development in equi-atomic multicomponent alloys*. Materials Science and Engineering: A, 2004. **375**: p. 213-218.
11. K.B. Kim, P.J. Warren, B. Cantor. *Formation of metallic glasses in novel (Ti<sub>33</sub>Zr<sub>33</sub>Hf<sub>33</sub>)<sub>100-xy</sub> (Ni<sub>50</sub>Cu<sub>50</sub>)<sub>x</sub>Al<sub>y</sub> Alloys*. Materials transactions, 2003. **44**(3): p. 411-413.
12. J.W. Yeh, S.K. Chen, S.J. Lin, J.Y. Gan, T.S. Chin, T.T. Shun, C.H. Tsau, S.Y. Chang. *Nanostructured High-Entropy Alloys with Multiple Principal Elements: Novel Alloy Design Concepts and Outcomes*. Advanced Engineering Materials, 2004. **6**(5): p. 299-303.
13. A.L. Greer. *Confusion by design*. Nature, 1993. **366**(6453): p. 303-304.
14. Y. Zhang, Y.J. Zhou, J.P. Lin, G.L. Chen, P.K. Liaw. *Solid-solution phase formation rules for multi-component alloys*. Advanced Engineering Materials, 2008. **10**(6): p. 534-538.
15. B. Fultz. *Vibrational thermodynamics of materials*. Progress in Materials Science, 2010. **55**(4): p. 247-352.
16. R.A. Swalin. *Thermodynamics of Solids*. 1970: John Wiley and Sons.
17. J.W. Yeh, S.K. Chen, S.J. Lin, J.Y. Gan, T.S. Chin, T.T. Shun, C.H. Tsau, S.Y. Chang. *Nanostructured High-Entropy Alloys with Multiple Principal Elements: Novel Alloy Design Concepts and Outcomes*. Advanced Engineering Materials, 2004. **6**(5): p. 299-303.
18. Y. Jien-Wei. *Recent progress in high-entropy alloys*. Ann. Chim. Sci. Mat, 2006. **31**(6): p. 633-648.
19. M.-H. Tsai, J.-W. Yeh. *High-Entropy Alloys: A Critical Review*. Materials Research Letters, 2014. **2**(3): p. 107-123.

20. B. Cantor. *Multicomponent and high entropy alloys*. Entropy, 2014. **16**(9): p. 4749-4768.
21. Y. Zhang, Z. Lu, S. Ma, P. Liaw, Z. Tang, Y. Cheng, M. Gao. *Guidelines in predicting phase formation of high-entropy alloys*. Mrs Communications, 2014. **4**(2): p. 57-62.
22. B.S. Murty, J.-W. Yeh, S. Ranganathan. *High-entropy alloys*. 2014: Butterworth-Heinemann.
23. Y. Wu, H. Wang, X.J. Liu, X.H. Chen, X.D. Hui, Y. Zhang, Z.P. Lu. *Designing Bulk Metallic Glass Composites with Enhanced Formability and Plasticity*. Journal of Materials Science & Technology, 2014. **30**(6): p. 566-575.
24. G. Sheng, C.T. Liu. *Phase stability in high entropy alloys: formation of solid-solution phase or amorphous phase*. Progress in Natural Science: Materials International, 2011. **21**(6): p. 433-446.
25. F. Boer, R. Boom, W. Mattens, A. Miedema, A. Niessen. *Cohesion in Metals: Transition Metal Alloys (Cohesion and Structure)*. 1989, North Holland, Amsterdam.
26. A. Takeuchi, A. Inoue. *Calculations of Mixing Enthalpy and Mismatch Entropy for Ternary Amorphous Alloys*. Materials Transactions, JIM, 2000. **41**(11): p. 1372-1378.
27. P.S. Rudman, J. Stringer, R.I. Jaffee. *Phase stability in metals and alloys*. Factors affecting the stability of metallic phases, ed. W. Hume-Rothery. Vol. 1. 1967: McGraw-Hill.
28. D.A. Porter, K.E. Easterling, M. Sherif. *Phase Transformations in Metals and Alloys, (Revised Reprint)*. 2009: CRC press.
29. M. De Graef, M.E. McHenry. *Structure of materials: an introduction to crystallography, diffraction and symmetry*. 2012: Cambridge University Press.
30. L. Pauling. *The nature of the chemical bond. IV. The energy of single bonds and the relative electronegativity of atoms*. Journal of the American Chemical Society, 1932. **54**(9): p. 3570-3582.
31. R.S. Mulliken. *A new electroaffinity scale; together with data on valence states and on valence ionization potentials and electron affinities*. The Journal of Chemical Physics, 1934. **2**(11): p. 782-793.
32. L.C. Allen. *Electronegativity is the average one-electron energy of the valence-shell electrons in ground-state free atoms*. Journal of the American Chemical Society, 1989. **111**(25): p. 9003-9014.
33. X. Gao, K. Zhao, H. Ke, D. Ding, W. Wang, H. Bai. *High mixing entropy bulk metallic glasses*. Journal of Non-Crystalline Solids, 2011. **357**(21): p. 3557-3560.
34. S. Guo, Q. Hu, C. Ng, C. Liu. *More than entropy in high-entropy alloys: Forming solid solutions or amorphous phase*. Intermetallics, 2013. **41**: p. 96-103.
35. A. Inoue. *Stabilization of metallic supercooled liquid and bulk amorphous alloys*. Acta Materialia, 2000. **48**(1): p. 279-306.
36. C.T.L. Sheng GUO. *Phase stability in high entropy alloys Formation of solid-solution phase or amorphous phase*. 2011. **21**: p. 443-446.
37. A. Cunliffe, J. Plummer, I. Figueroa, I. Todd. *Glass formation in a high entropy alloy system by design*. Intermetallics, 2012. **23**: p. 204-207.
38. X. Yang, Y. Zhang. *Prediction of high-entropy stabilized solid-solution in multi-component alloys*. Materials Chemistry and Physics, 2012. **132**(2): p. 233-238.

39. Y. Zhang, X. Yang, P. Liaw. *Alloy design and properties optimization of high-entropy alloys*. Jom, 2012. **64**(7): p. 830-838.
40. C. Zhang, F. Zhang, S. Chen, W. Cao. *Computational thermodynamics aided high-entropy alloy design*. Jom, 2012. **64**(7): p. 839-845.
41. A. Durga, K.H. Kumar, B. Murty. *Phase formation in equi-atomic high entropy alloys: Calphad approach and experimental studies*. Transactions of the Indian Institute of Metals, 2012. **65**(4): p. 375-380.
42. R. Raghavan, K.H. Kumar, B. Murty. *Analysis of phase formation in multi-component alloys*. Journal of Alloys and Compounds, 2012. **544**: p. 152-158.
43. C. Li, M. Zhao, J. Li, Q. Jiang. *B2 structure of high-entropy alloys with addition of Al*. Journal of Applied Physics, 2008. **104**(11): p. 113504.
44. M.F. del Grosso, G. Bozzolo, H.O. Mosca. *Determination of the transition to the high entropy regime for alloys of refractory elements*. Journal of Alloys and Compounds, 2012. **534**: p. 25-31.
45. S.-W. Kao, J.-W. Yeh, T.-S. Chin. *Rapidly solidified structure of alloys with up to eight equal-molar elements—a simulation by molecular dynamics*. Journal of Physics: Condensed Matter, 2008. **20**(14): p. 145214.
46. S. Wang. *Atomic structure modeling of multi-principal-element alloys by the principle of maximum entropy*. Entropy, 2013. **15**(12): p. 5536-5548.
47. F. Tian, L. Delczeg, N. Chen, L.K. Varga, J. Shen, L. Vitos. *Structural stability of NiCoFeCrAl<sub>x</sub> high-entropy alloy from ab initio theory*. Physical Review B, 2013. **88**(8): p. 085128.
48. J.-W. Yeh. *Alloy Design Strategies and Future Trends in High-Entropy Alloys*. JOM, 2013. **65**(12): p. 1759-1771.
49. F. Otto, A. Dlouhý, K.G. Pradeep, M. Kuběnová, D. Raabe, G. Eggeler, E.P. George. *Decomposition of the single-phase high-entropy alloy CrMnFeCoNi after prolonged anneals at intermediate temperatures*. Acta Materialia, 2016. **112**: p. 40-52.
50. N. Jones, J. Aveson, A. Bhowmik, B. Conduit, H. Stone. *On the entropic stabilisation of an Al<sub>0.5</sub>CrFeCoNiCu high entropy alloy*. Intermetallics, 2014. **54**: p. 148-153.
51. N.G. Jones, K. Christofidou, H.J. Stone. *Rapid precipitation in an Al<sub>0.5</sub>CrFeCoNiCu high entropy alloy*. Materials Science and Technology, 2015. **31**(10): p. 1171-1177.
52. E. Pickering, H. Stone, N. Jones. *Fine-scale precipitation in the high-entropy alloy Al<sub>0.5</sub>CrFeCoNiCu*. Materials Science and Engineering: A, 2015. **645**: p. 65-71.
53. N.G. Jones, A. Frezza, H.J. Stone. *Phase equilibria of an Al<sub>0.5</sub>CrFeCoNiCu High Entropy Alloy*. Materials Science and Engineering: A, 2014. **615**: p. 214-221.
54. N.G. Jones, R. Izzo, P.M. Mignanelli, K.A. Christofidou, H.J. Stone. *Phase evolution in an Al<sub>0.5</sub>CrFeCoNiCu High Entropy Alloy*. Intermetallics, 2016. **71**: p. 43-50.
55. O. Senkov, J. Miller, D. Miracle, C. Woodward. *Accelerated exploration of multi-principal element alloys with solid solution phases*. Nature communications, 2015. **6**.
56. O. Senkov, G. Wilks, D. Miracle, C. Chuang, P. Liaw. *Refractory high-entropy alloys*. Intermetallics, 2010. **18**(9): p. 1758-1765.

57. Y.-F. Kao, S.-K. Chen, T.-J. Chen, P.-C. Chu, J.-W. Yeh, S.-J. Lin. *Electrical, magnetic, and Hall properties of Al<sub>x</sub>CoCrFeNi high-entropy alloys*. Journal of alloys and compounds, 2011. **509**(5): p. 1607-1614.
58. J.-W. Yeh, S.-Y. Chang, Y.-D. Hong, S.-K. Chen, S.-J. Lin. *Anomalous decrease in X-ray diffraction intensities of Cu–Ni–Al–Co–Cr–Fe–Si alloy systems with multi-principal elements*. Materials chemistry and physics, 2007. **103**(1): p. 41-46.
59. K.-Y. Tsai, M.-H. Tsai, J.-W. Yeh. *Sluggish diffusion in Co–Cr–Fe–Mn–Ni high-entropy alloys*. Acta Materialia, 2013. **61**(13): p. 4887-4897.
60. E. Pickering, N. Jones. *High-entropy alloys: a critical assessment of their founding principles and future prospects*. International Materials Reviews, 2016. **61**(3): p. 183-202.
61. Y. Zou, S. Maiti, W. Steurer, R. Spolenak. *Size-dependent plasticity in an Nb<sub>25</sub>Mo<sub>25</sub>Ta<sub>25</sub>W<sub>25</sub> refractory high-entropy alloy*. Acta Materialia, 2014. **65**: p. 85-97.
62. L.J. Santodonato, Y. Zhang, M. Feygenson, C.M. Parish, M.C. Gao, R.J. Weber, J.C. Neufeld, Z. Tang, P.K. Liaw. *Deviation from high-entropy configurations in the atomic distributions of a multi-principal-element alloy*. Nature communications, 2015. **6**: p. 5964.
63. Y. Jien-Wei. *Recent progress in high entropy alloys*. Ann. Chim. Sci. Mat, 2006. **31**(6): p. 633-648.
64. K.-H. Cheng, C.-H. Lai, S.-J. Lin, J.-W. Yeh, *Recent progress in multi-element alloy and nitride coatings sputtered from high-entropy alloy targets*. in *Annales de chimie*. 2006. Lavoisier.
65. W.F. Smith, J. Hashemi. *Foundations of materials science and engineering*. 2011: McGraw-Hill.
66. S. Praveen, B. Murty, R.S. Kottada. *Alloying behavior in multi-component AlCoCrCuFe and NiCoCrCuFe high entropy alloys*. Materials Science and Engineering: A, 2012. **534**: p. 83-89.
67. Y.P. Wang, B.S. Li, H.Z. Fu. *Solid Solution or Intermetallics in a High-Entropy Alloy*. Advanced engineering materials, 2009. **11**(8): p. 641-644.
68. M.-H. Tsai, H. Yuan, G. Cheng, W. Xu, K.-Y. Tsai, C.-W. Tsai, W.W. Jian, C.-C. Juan, W.-J. Shen, M.-H. Chuang. *Morphology, structure and composition of precipitates in Al<sub>0.3</sub>CoCrCu<sub>0.5</sub>FeNi high-entropy alloy*. Intermetallics, 2013. **32**: p. 329-336.
69. C.-J. Tong, Y.-L. Chen, J.-W. Yeh, S.-J. Lin, S.-K. Chen, T.-T. Shun, C.-H. Tsau, S.-Y. Chang. *Microstructure characterization of Al<sub>x</sub>CoCrCuFeNi high-entropy alloy system with multiprincipal elements*. Metallurgical and Materials Transactions A, 2005. **36**(4): p. 881-893.
70. W.-R. Wang, W.-L. Wang, S.-C. Wang, Y.-C. Tsai, C.-H. Lai, J.-W. Yeh. *Effects of Al addition on the microstructure and mechanical property of Al<sub>x</sub>CoCrFeNi high-entropy alloys*. Intermetallics, 2012. **26**(Supplement C): p. 44-51.
71. R. Sriharitha, B. Murty, R.S. Kottada. *Phase formation in mechanically alloyed Al<sub>x</sub>CoCrCuFeNi (x= 0.45, 1, 2.5, 5 mol) high entropy alloys*. Intermetallics, 2013. **32**: p. 119-126.
72. Y. Ma, B. Jiang, C. Li, Q. Wang, C. Dong, P.K. Liaw, F. Xu, L. Sun. *The BCC/B2 morphologies in Al<sub>x</sub>NiCoFeCr high-entropy alloys*. Metals, 2017. **7**(2): p. 57.

73. W.-R. Wang, W.-L. Wang, J.-W. Yeh. *Phases, microstructure and mechanical properties of Al<sub>x</sub>CoCrFeNi high-entropy alloys at elevated temperatures.* Journal of Alloys and Compounds, 2014. **589**: p. 143-152.
74. M.-R. Chen, S.-J. Lin, J.-W. Yeh, M.-H. Chuang, S.-K. Chen, Y.-S. Huang. *Effect of vanadium addition on the microstructure, hardness, and wear resistance of Al 0.5 CoCrCuFeNi high-entropy alloy.* Metallurgical and Materials Transactions A, 2006. **37**(5): p. 1363-1369.
75. C.-Y. Hsu, C.-C. Juan, W.-R. Wang, T.-S. Sheu, J.-W. Yeh, S.-K. Chen. *On the superior hot hardness and softening resistance of AlCoCr<sub>x</sub>FeMo 0.5 Ni high-entropy alloys.* Materials Science and Engineering: A, 2011. **528**(10): p. 3581-3588.
76. O.N. Senkov, F. Zhang, J.D. Miller. *Phase composition of a CrMo<sub>0.5</sub>NbTa<sub>0.5</sub>TiZr high entropy alloy: Comparison of experimental and simulated data.* Entropy, 2013. **15**(9): p. 3796-3809.
77. Y. Dong, Y.P. Lu, J.J. Zhang, T.J. Li, *Microstructure and properties of multi-component Al<sub>x</sub>CoCrFeNiTi<sub>0.5</sub> high-entropy alloys.* in *Materials Science Forum.* 2013. Trans Tech Publ.
78. J. Cheng, X. Liang, B. Xu. *Effect of Nb addition on the structure and mechanical behaviors of CoCrCuFeNi high-entropy alloy coatings.* Surface and Coatings Technology, 2014. **240**: p. 184-190.
79. L. Ma, L. Wang, T. Zhang, A. Inoue. *Bulk glass formation of Ti-Zr-Hf-Cu-M (M= Fe, Co, Ni) alloys.* Materials transactions, 2002. **43**(2): p. 277-280.
80. N. Nishiyama, A. Inoue. *Stability and nucleation behavior of glass-forming Pd-Cu-Ni-P alloy with a critical cooling rate of 0.067 K/s.* Intermetallics, 2002. **10**(11-12): p. 1141-1147.
81. A. Inoue, N. Nishiyama, H. Kimura. *Preparation and thermal stability of bulk amorphous Pd 40Cu 30Ni 10P 20 alloy cylinder of 72 mm in diameter.* Materials Transactions, JIM, 1997. **38**(2): p. 179-183.
82. D. Turnbull. *Under what conditions can a glass be formed?* Contemporary physics, 1969. **10**(5): p. 473-488.
83. A. Inoue, A. Takeuchi. *Recent development and application products of bulk glassy alloys.* Acta Materialia, 2011. **59**(6): p. 2243-2267.
84. A. Peker, W.L. Johnson. *A highly processable metallic glass: Zr<sub>41</sub>Ti<sub>13.8</sub>Cu<sub>12.5</sub>Ni<sub>10.0</sub>Be<sub>22.5</sub>.* Applied Physics Letters, 1993. **63**(17): p. 2342-2344.
85. A. Inoue, T. Zhang, T. Itoi, A. Takeuchi. *New Fe-Co-Ni-Zr-B amorphous alloys with wide supercooled liquid regions and good soft magnetic properties.* Materials Transactions, JIM, 1997. **38**(4): p. 359-362.
86. X. Wang, I. Yoshii, A. Inoue, Y.-H. Kim, I.-B. Kim. *Bulk amorphous Ni 75-x Nb 5 M x P 20-y B y (M= Cr, Mo) alloys with large supercooling and high strength.* Materials Transactions, JIM, 1999. **40**(10): p. 1130-1136.
87. T. Zhang, A. Inoue. *Thermal and mechanical properties of Ti-Ni-Cu-Sn amorphous alloys with a wide supercooled liquid region before crystallization.* Materials transactions, JIM, 1998. **39**(10): p. 1001-1006.
88. A. Inoue. *High strength bulk amorphous alloys with low critical cooling rates.* Materials Transactions, JIM, 1995. **36**(7): p. 866-875.
89. A. Takeuchi, N. Chen, T. Wada, Y. Yokoyama, H. Kato, A. Inoue, J. Yeh. *Pd 20 Pt 20 Cu 20 Ni 20 P 20 high-entropy alloy as a bulk metallic glass in the centimeter.* Intermetallics, 2011. **19**(10): p. 1546-1554.

90. H.F. Li, X.H. Xie, K. Zhao, Y.B. Wang, Y.F. Zheng, W.H. Wang, L. Qin. *In vitro and in vivo studies on biodegradable CaMgZnSrYb high-entropy bulk metallic glass*. Acta Biomaterialia, 2013. **9**(10): p. 8561-8573.
91. K. Kim, P. Warren, B. Cantor. *Glass-forming ability of novel multicomponent (Ti 33 Zr 33 Hf 33)–(Ni 50 Cu 50)–Al alloys developed by equi-atomic substitution*. Materials Science and Engineering: A, 2004. **375**: p. 317-321.
92. J. Wang, Z. Zheng, J. Xu, Y. Wang. *Microstructure and magnetic properties of mechanically alloyed FeSiBAlNi (Nb) high entropy alloys*. Journal of Magnetism and Magnetic Materials, 2014. **355**(0): p. 58-64.
93. K.-H. Cheng, C.-H. Lai, S.-J. Lin, J.-W. Yeh. *Structural and mechanical properties of multi-element (AlCrMoTaTiZr)<sub>Nx</sub> coatings by reactive magnetron sputtering*. Thin Solid Films, 2011. **519**(10): p. 3185-3190.
94. K. Ohsaka, E. Trinh, J. Holzer, W. Johnson. *Gibbs free-energy difference between the glass and crystalline phases of a Ni-Zr alloy*. Applied physics letters, 1993. **62**(19): p. 2319-2321.
95. M.A. Hemphill, T. Yuan, G.Y. Wang, J.W. Yeh, C.W. Tsai, A. Chuang, P.K. Liaw. *Fatigue behavior of Al<sub>0.5</sub>CoCrCuFeNi high entropy alloys*. Acta Materialia, 2012. **60**(16): p. 5723-5734.
96. D.A. Porter, K.E. Easterling, M. Sherif. *Phase Transformations in Metals and Alloys, Third Edition (Revised Reprint)*. 2009: CRC Press.
97. M.C. Gao, J.W. Yeh, P.K. Liaw, Y. Zhang. *High-Entropy Alloys: Fundamentals and Applications*. Physical Metallurgy, ed. J.-W. Yeh. 2016: Springer International Publishing. 516.
98. T. Egami. *The atomic structure of aluminum based metallic glasses and universal criterion for glass formation*. Journal of non-crystalline solids, 1996. **205**: p. 575-582.
99. T. Egami, Y. Waseda. *Atomic size effect on the formability of metallic glasses*. Journal of non-crystalline solids, 1984. **64**(1-2): p. 113-134.
100. J. Gao, J. Sharp, D. Guan, W. Rainforth, I. Todd. *New compositional design for creating tough metallic glass composites with excellent work hardening*. Vol. 86. 2015.
101. H. Yinnon, D.R. Uhlmann. *Applications of thermoanalytical techniques to the study of crystallization kinetics in glass-forming liquids, part I: theory*. Journal of Non-Crystalline Solids, 1983. **54**(3): p. 253-275.
102. P. Gong, S. Zhao, H. Ding, K. Yao, X. Wang. *Nonisothermal crystallization kinetics, fragility and thermodynamics of Ti 20 Zr 20 Cu 20 Ni 20 Be 20 high entropy bulk metallic glass*. Journal of Materials Research, 2015. **30**(18): p. 2772-2782.
103. P. Gong, K.F. Yao, H.Y. Ding. *Crystallization kinetics of TiZrHfCuNiBe high entropy bulk metallic glass*. Materials Letters, 2015. **156**: p. 146-149.
104. J.C. Qiao, J.M. Pelletier. *Crystallization kinetics in Cu<sub>46</sub>Zr<sub>45</sub>Al<sub>7</sub>Y<sub>2</sub> bulk metallic glass by differential scanning calorimetry (DSC)*. Journal of Non-Crystalline Solids, 2011. **357**(14): p. 2590-2594.
105. M. Song, Y. He. *Effect of isothermal annealing on the compressive strength of a ZrAlNiCuNb metallic glass*. Journal of Alloys and Compounds, 2011. **509**(5): p. 2606-2610.
106. Y. Hiki, M. Tanahashi, R. Tamura, S. Takeuchi, H. Takahashi. *Stabilization of metallic glass by isochronal and isothermal annealing treatments*. Journal of Physics: Condensed Matter, 2007. **19**(20): p. 205147.

107. J. Schroers, A. Masuhr, W.L. Johnson, R. Busch. *Pronounced asymmetry in the crystallization behavior during constant heating and cooling of a bulk metallic glass-forming liquid*. Physical Review B, 1999. **60**(17): p. 11855.
108. M. Çelikbilek, A.E. Ersundu, S. Aydın. *Crystallization kinetics of amorphous materials*, in *Advances in crystallization processes*. 2012, InTech.
109. F. Hernández-Sánchez, L.F. del Castillo, R. Vera-Graziano. *Isothermal crystallization kinetics of polypropylene by differential scanning calorimetry. I. Experimental conditions*. Journal of applied polymer science, 2004. **92**(2): p. 970-978.
110. S. Kasyap, A.T. Patel, A. Pratap. *Crystallization kinetics of Ti<sub>20</sub>Zr<sub>20</sub>Cu<sub>60</sub> metallic glass by isoconversional methods using modulated differential scanning calorimetry*. Journal of Thermal Analysis and Calorimetry, 2014. **116**(3): p. 1325-1336.
111. M. Avrami. *Kinetics of phase change. I General theory*. The Journal of Chemical Physics, 1939. **7**(12): p. 1103-1112.
112. M. Avrami. *Kinetics of phase change. II Transformation-time relations for random distribution of nuclei*. The Journal of Chemical Physics, 1940. **8**(2): p. 212-224.
113. M. Avrami. *Granulation, phase change, and microstructure kinetics of phase change. III*. The Journal of chemical physics, 1941. **9**(2): p. 177-184.
114. W.A. Johnson, M. K.F. 1981. **135**(416).
115. D.V. Ragone. *Thermodynamics of Materials, Volume 1*. Thermodynamics of Materials, Volume 1, by David V. Ragone, pp. 336. ISBN 0-471-30885-4. Wiley-VCH, October 1994., 1994: p. 336.
116. J.W. Christian. *The Theory of Transformations in Metals and Alloys*. 2002: Elsevier Science.
117. A.L. Greer. *Crystallisation kinetics of Fe<sub>80</sub>B<sub>20</sub> glass*. Acta Metallurgica, 1982. **30**(1): p. 171-192.
118. M.M. Nicolaus, H.R. Sinning, F. Haessner. *Crystallization behaviour and generation of a nanocrystalline state from amorphous Co<sub>33</sub>Zr<sub>67</sub>*. Materials Science and Engineering: A, 1992. **150**(1): p. 101-112.
119. T. Ozawa. *Kinetics of non-isothermal crystallization*. Polymer, 1971. **12**(3): p. 150-158.
120. K. Matsushita, S. Sakka. *Kinetic Study on Non-Isothermal Crystallization of Glass by Thermal Analysis (Commemoration Issue Dedicated to Professor Megumi Tashiro on the Occasion of his Retirement)*. 1981.
121. T.-T. Shun, L.-Y. Chang, M.-H. Shiu. *Microstructures and mechanical properties of multiprincipal component CoCrFeNiTi<sub>x</sub> alloys*. Materials Science and Engineering: A, 2012. **556**: p. 170-174.
122. N. Stepanov, D. Shaysultanov, G. Salishchev, M. Tikhonovsky, E. Oleynik, A. Tortika, O. Senkov. *Effect of V content on microstructure and mechanical properties of the CoCrFeMnNiV<sub>x</sub> high entropy alloys*. Journal of Alloys and Compounds, 2015. **628**: p. 170-185.
123. W.-R. Wang, W.-L. Wang, S.-C. Wang, Y.-C. Tsai, C.-H. Lai, J.-W. Yeh. *Effects of Al addition on the microstructure and mechanical property of Al<sub>x</sub>CoCrFeNi high-entropy alloys*. Intermetallics, 2012. **26**: p. 44-51.
124. C.-C. Juan, C.-Y. Hsu, C.-W. Tsai, W.-R. Wang, T.-S. Sheu, J.-W. Yeh, S.-K. Chen. *On microstructure and mechanical performance of AlCoCrFeMo<sub>0.5</sub>Ni<sub>x</sub> high-entropy alloys*. Intermetallics, 2013. **32**: p. 401-407.

125. W. Liu, Z. Lu, J. He, J. Luan, Z. Wang, B. Liu, Y. Liu, M. Chen, C. Liu. *Ductile CoCrFeNiMo x high entropy alloys strengthened by hard intermetallic phases*. Acta Materialia, 2016. **116**: p. 332-342.
126. Y. Zhang, T.T. Zuo, Z. Tang, M.C. Gao, K.A. Dahmen, P.K. Liaw, Z.P. Lu. *Microstructures and properties of high-entropy alloys*. Progress in Materials Science, 2014. **61**: p. 1-93.
127. Y. Lu, Y. Dong, S. Guo, L. Jiang, H. Kang, T. Wang, B. Wen, W. Zhijun, J.C. Jie, Z. Cao, H.H. Ruan, Y. Lu. *A Promising New Class of High-Temperature Alloys: Eutectic High-Entropy Alloys*. Vol. 4. 2014. 6200.
128. F. He, Z. Wang, P. Cheng, Q. Wang, J. Li, Y. Dang, J. Wang, C. Liu. *Designing eutectic high entropy alloys of CoCrFeNiNb x*. Journal of Alloys and Compounds, 2016. **656**: p. 284-289.
129. M.C. Tropicovsky, J.R. Morris, P.R. Kent, A.R. Lupini, G.M. Stocks. *Criteria for predicting the formation of single-phase high-entropy alloys*. Physical Review X, 2015. **5**(1): p. 011041.
130. M.C. Gao, D.E. Alman. *Searching for next single-phase high-entropy alloy compositions*. Entropy, 2013. **15**(10): p. 4504-4519.
131. C. Toffolon, C. Servant. *Thermodynamic assessment of the Fe-Nb system*. Calphad, 2000. **24**(2): p. 97-112.
132. J.G.C. Neto, S.G. Fries, H.L. Lukas, S. Gama, G. Effenberg. *Thermodynamic optimisation of the Nb-Cr system*. Calphad, 1993. **17**(3): p. 219-228.
133. F. Stein, D. Jiang, M. Palm, G. Sauthoff, D. Grüner, G. Kreiner. *Experimental reinvestigation of the Co-Nb phase diagram*. Intermetallics, 2008. **16**(6): p. 785-792.
134. P. Nash, A. Nash. *The Nb-Ni (niobium-nickel) system*. Journal of Phase Equilibria, 1986. **7**(2): p. 124-130.
135. I.S. Wani, T. Bhattacharjee, S. Sheikh, P.P. Bhattacharjee, S. Guo, N. Tsuji. *Tailoring nanostructures and mechanical properties of AlCoCrFeNi2.1 eutectic high entropy alloy using thermo-mechanical processing*. Materials Science and Engineering: A, 2016. **675**(Supplement C): p. 99-109.
136. I.S. Wani, T. Bhattacharjee, S. Sheikh, I.T. Clark, M.H. Park, T. Okawa, S. Guo, P.P. Bhattacharjee, N. Tsuji. *Cold-rolling and recrystallization textures of a nano-lamellar AlCoCrFeNi2.1 eutectic high entropy alloy*. Intermetallics, 2017. **84**(Supplement C): p. 42-51.
137. Z. Li, K.G. Pradeep, Y. Deng, D. Raabe, C.C. Tasan. *Metastable high-entropy dual-phase alloys overcome the strength-ductility trade-off*. Nature, 2016. **534**(7606): p. 227-230.
138. A.C. Larson, R.B. Von Dreele. *Gsas. General Structure Analysis System*. LANSCE, MS-H805, Los Alamos, New Mexico, 1994.
139. B.H. Toby. *EXPGUI, a graphical user interface for GSAS*. Journal of applied crystallography, 2001. **34**(2): p. 210-213.
140. G. Yuan, A. Inoue. *The effect of Ni substitution on the glass-forming ability and mechanical properties of Mg-Cu-Gd metallic glass alloys*. Journal of Alloys and Compounds, 2005. **387**(1): p. 134-138.
141. C. Suryanarayana, A. Inoue. *Bulk metallic glasses*. 2010: CRC press.
142. X. Qiu-Wei, Z. Yong. *Amorphous phase formation rules in high-entropy alloys*.
143. T. Chen, T. Shun, J. Yeh, M. Wong. *Nanostructured nitride films of multi-element high-entropy alloys by reactive DC sputtering*. Surface and Coatings Technology, 2004. **188**: p. 193-200.

144. R. Busch, J. Schroers, W.H. Wang. *Thermodynamics and Kinetics of Bulk Metallic Glass*. MRS Bulletin, 2007. **32**(08): p. 620-623.
145. J.S.C. Jang, L.J. Chang, G.J. Chen, J.C. Huang. *Crystallization behavior of the Zr<sub>63</sub>Al<sub>17.5</sub>Cu<sub>17.5</sub>Ni<sub>10</sub>B<sub>2</sub> amorphous alloy during isothermal annealing*. Intermetallics, 2005. **13**(8): p. 907-911.
146. I. Martin, T. Ohkubo, M. Ohnuma, B. Deconihout, K. Hono. *Nanocrystallization of Zr<sub>41.2</sub>Ti<sub>13.8</sub>Cu<sub>12.5</sub>Ni<sub>10.0</sub>Be<sub>22.5</sub> metallic glass*. Acta Materialia, 2004. **52**(15): p. 4427-4435.
147. D.W. Henderson. *Thermal analysis of non-isothermal crystallization kinetics in glass forming liquids*. Journal of Non-Crystalline Solids, 1979. **30**(3): p. 301-315.
148. L.-C. Zhang, J. Xu, J. Eckert. *Thermal stability and crystallization kinetics of mechanically alloyed Ti C/ Ti-based metallic glass matrix composite*. Journal of applied physics, 2006. **100**(3): p. 033514.
149. L. Zou, Y. Li, C. Yang, S. Qu, Y. Li. *Effect of Fe content on glass-forming ability and crystallization behavior of a (Ti 69.7 Nb 23.7 Zr 4.9 Ta 1.7) 100-xFex alloy synthesized by mechanical alloying*. Journal of Alloys and Compounds, 2013. **553**: p. 40-47.
150. D.S. dos Santos, D.R. dos Santos. *Crystallization kinetics of Fe-B-Si metallic glasses*. Journal of Non-Crystalline Solids, 2002. **304**(1): p. 56-63.
151. H.-R. Wang, Y.-L. Gao, Y.-F. Ye, G.-H. Min, Y. Chen, X.-Y. Teng. *Crystallization kinetics of an amorphous Zr-Cu-Ni alloy: calculation of the activation energy*. Journal of Alloys and Compounds, 2003. **353**(1): p. 200-206.
152. Z.-Z. Yuan, X.-D. Chen, B.-X. Wang, Z.-J. Chen. *Crystallization kinetics of melt-spun Co<sub>43</sub>Fe<sub>20</sub>Ta<sub>5.5</sub>B<sub>31.5</sub> amorphous alloy*. Journal of Alloys and Compounds, 2005. **399**(1): p. 166-172.
153. H.E. Kissinger. *Variation of peak temperature with heating rate in differential thermal analysis*. Journal of research of the National Bureau of Standards, 1956. **57**(4): p. 217-221.
154. J. Augis, J. Bennett. *Calculation of the Avrami parameters for heterogeneous solid state reactions using a modification of the Kissinger method*. Journal of Thermal Analysis and Calorimetry, 1978. **13**(2): p. 283-292.
155. Y.-L. Gao, J. Shen, J.-F. Sun, G. Wang, D.-W. Xing, H.-Z. Xian, B.-D. Zhou. *Crystallization behavior of ZrAlNiCu bulk metallic glass with wide supercooled liquid region*. Materials Letters, 2003. **57**(13): p. 1894-1898.
156. K. Nakamura, T. Watanabe, K. Katayama, T. Amano. *Some aspects of nonisothermal crystallization of polymers. I. Relationship between crystallization temperature, crystallinity, and cooling conditions*. Journal of Applied Polymer Science, 1972. **16**(5): p. 1077-1091.
157. K. Nakamura, K. Katayama, T. Amano. *Some aspects of nonisothermal crystallization of polymers. II. Consideration of the isokinetic condition*. Journal of Applied Polymer Science, 1973. **17**(4): p. 1031-1041.
158. A. Takeuchi, A. Inoue. *Classification of bulk metallic glasses by atomic size difference, heat of mixing and period of constituent elements and its application to characterization of the main alloying element*. Materials Transactions, 2005. **46**(12): p. 2817-2829.
159. J.-M. Pelletier, B. Van de Moortèle. *Phase separation and crystallization in the Zr 41.2-Ti 13.8-Cu 12.5-Ni 10-Be 22.5 bulk metallic glass determined by*

- physical measurements and electron microscopy*. Journal of non-crystalline solids, 2003. **325**(1): p. 133-141.
160. H. Li, X. Xie, K. Zhao, Y. Wang, Y. Zheng, W. Wang, L. Qin. *In vitro and in vivo studies on biodegradable CaMgZnSrYb high-entropy bulk metallic glass*. Acta biomaterialia, 2013. **9**(10): p. 8561-8573.
  161. K.K. Song, P. Gargarella, S. Pauly, G.Z. Ma, U. Kühn, J. Eckert. *Correlation between glass-forming ability, thermal stability, and crystallization kinetics of Cu-Zr-Ag metallic glasses*. Journal of Applied Physics, 2012. **112**(6): p. 063503.
  162. Y. Li, C. Yang, L. Kang, H. Zhao, S. Qu, X. Li, W. Zhang, Y. Li. *Non-isothermal and isothermal crystallization kinetics and their effect on microstructure of sintered and crystallized TiNbZrTaSi bulk alloys*. Journal of Non-Crystalline Solids, 2016. **432**: p. 440-452.
  163. J. Colmenero, J. Barandiaran. *Crystallization of Al<sub>23</sub>Te<sub>77</sub> glasses*. Journal of Non-Crystalline Solids, 1979. **30**(3): p. 263-271.
  164. S. Venkataraman, E. Rozhkova, J. Eckert, L. Schultz, D. Sordelet. *Thermal stability and crystallization kinetics of Cu-reinforced Cu<sub>47</sub>Ti<sub>33</sub>Zr<sub>11</sub>Ni<sub>8</sub>Si<sub>1</sub> metallic glass composite powders synthesized by ball milling: the effect of particulate reinforcement*. Intermetallics, 2005. **13**(8): p. 833-840.
  165. Y. Yang, D. Xing, J. Shen, J. Sun, S. Wei, H. He, D. McCartney. *Crystallization kinetics of a bulk amorphous Cu-Ti-Zr-Ni alloy investigated by differential scanning calorimetry*. Journal of Alloys and Compounds, 2006. **415**(1): p. 106-110.
  166. L. Liu, X. Zhao, C. Ma, T. Zhang. *Kinetics of crystallization process for Pd-based bulk metallic glasses*. Intermetallics, 2009. **17**(4): p. 241-245.
  167. J.W. Yeh, Y.L. Chen, S.J. Lin, S.K. Chen, *High-entropy alloys—a new era of exploitation*. in *Materials Science Forum*. 2007. Trans Tech Publ.
  168. S. Wei, B. Ding, T. Lei, Z. Hu. *Crystallization of amorphous Zr<sub>65</sub>Cu<sub>27</sub>Al<sub>8</sub> alloy with wide supercooled liquid region*. Materials Letters, 1998. **37**(4): p. 263-267.
  169. X. Hu, J. Qiao, J.M. Pelletier, Y. Yao. *Evaluation of thermal stability and isochronal crystallization kinetics in the Ti<sub>40</sub>Zr<sub>25</sub>Ni<sub>8</sub>Cu<sub>9</sub>Be<sub>18</sub> bulk metallic glass*. Journal of Non-Crystalline Solids, 2016. **432**(Part B): p. 254-264.
  170. L. Liu, Z.F. Wu, J. Zhang. *Crystallization kinetics of Zr<sub>55</sub>Cu<sub>30</sub>Al<sub>10</sub>Ni<sub>5</sub> bulk amorphous alloy*. Journal of Alloys and Compounds, 2002. **339**(1): p. 90-95.
  171. Y. Lu, Y. Dong, S. Guo, L. Jiang, H. Kang, T. Wang, B. Wen, Z. Wang, J. Jie, Z. Cao. *A promising new class of high-temperature alloys: eutectic high-entropy alloys*. Scientific reports, 2014. **4**: p. 6200.
  172. Y. Lu, X. Gao, L. Jiang, Z. Chen, T. Wang, J. Jie, H. Kang, Y. Zhang, S. Guo, H. Ruan. *Directly cast bulk eutectic and near-eutectic high entropy alloys with balanced strength and ductility in a wide temperature range*. Acta materialia, 2017. **124**: p. 143-150.
  173. Y. Lu, Y. Dong, S. Guo, L. Jiang, H. Kang, T. Wang, B. Wen, Z. Wang, J. Jie, Z. Cao. *A promising new class of high-temperature alloys: eutectic high-entropy alloys*. Scientific reports, 2014. **4**.
  174. Y. Tan, J. Li, J. Wang, H. Kou. *Seaweed eutectic-dendritic solidification pattern in a CoCrFeNiMnPd eutectic high-entropy alloy*. Intermetallics, 2017. **85**: p. 74-79.

175. J. Zhu, H. Fu, H. Zhang, A. Wang, H. Li, Z. Hu. *Microstructures and compressive properties of multicomponent AlCoCrFeNiMo<sub>x</sub> alloys*. Materials Science and Engineering: A, 2010. **527**(26): p. 6975-6979.
176. Y. Dong, Y. Lu, J. Kong, J. Zhang, T. Li. *Microstructure and mechanical properties of multi-component AlCrFeNiMo<sub>x</sub> high-entropy alloys*. Journal of Alloys and Compounds, 2013. **573**: p. 96-101.
177. S. Ma, Y. Zhang. *Effect of Nb addition on the microstructure and properties of AlCoCrFeNi high-entropy alloy*. Materials Science and Engineering: A, 2012. **532**: p. 480-486.
178. F. He, Z. Wang, P. Cheng, Q. Wang, J. Li, Y. Dang, J. Wang, C.T. Liu. *Designing eutectic high entropy alloys of CoCrFeNiNb<sub>x</sub>*. Journal of Alloys and Compounds, 2016. **656**: p. 284-289.
179. B. Li, Y. Wang, M. Ren, C. Yang, H. Fu. *Effects of Mn, Ti and V on the microstructure and properties of AlCrFeCoNiCu high entropy alloy*. Materials Science and Engineering: A, 2008. **498**(1): p. 482-486.
180. S. Guo, C. Ng, C. Liu. *Sunflower-like solidification microstructure in a near-eutectic high-entropy alloy*. Materials Research Letters, 2013. **1**(4): p. 228-232.
181. Y. Tan, J. Li, J. Wang, M. Kolbe, H. Kou. *Microstructure characterization of CoCrFeNiMnPdx eutectic high-entropy alloys*. Journal of Alloys and Compounds, 2018. **731**(Supplement C): p. 600-611.
182. Y. Zhang, T. Zuo, Y. Cheng, P.K. Liaw. *High-entropy alloys with high saturation magnetization, electrical resistivity, and malleability*. Scientific reports, 2013. **3**.
183. S.N. Kabekkodu, J. Faber, T. Fawcett. *New Powder Diffraction File (PDF-4) in relational database format: advantages and data-mining capabilities*. Acta Crystallographica Section B: Structural Science, 2002. **58**(3): p. 333-337.
184. R. Hill, C. Howard. *Quantitative phase analysis from neutron powder diffraction data using the Rietveld method*. Journal of Applied Crystallography, 1987. **20**(6): p. 467-474.
185. S. Guo, C. Ng, J. Lu, C. Liu. *Effect of valence electron concentration on stability of fcc or bcc phase in high entropy alloys*. Journal of applied physics, 2011. **109**(10): p. 103505.
186. Z. Leong, J.S. Wróbel, S.L. Dudarev, R. Goodall, I. Todd, D. Nguyen-Manh. *The Effect of Electronic Structure on the Phases Present in High Entropy Alloys*. Scientific Reports, 2017. **7**: p. 39803.
187. M. Palm. *Concepts derived from phase diagram studies for the strengthening of Fe–Al-based alloys*. Intermetallics, 2005. **13**(12): p. 1286-1295.
188. R. Nakamura, K. Takasawa, Y. Yamazaki, Y. Iijima. *Single-phase interdiffusion in the B2 type intermetallic compounds NiAl, CoAl and FeAl*. Intermetallics, 2002. **10**(2): p. 195-204.
189. Z. Tang, M.C. Gao, H. Diao, T. Yang, J. Liu, T. Zuo, Y. Zhang, Z. Lu, Y. Cheng, Y. Zhang. *Aluminum alloying effects on lattice types, microstructures, and mechanical behavior of high-entropy alloys systems*. Jom, 2013. **65**(12): p. 1848-1858.
190. Y. Kimura, H. Kuriyama, T. Suzuki, Y. Mishima. *Microstructure Control and Mechanical Properties of Binary Co–Al Alloys Based on B2 Intermetallic Compound CoAl*. Materials Transactions, JIM, 1994. **35**(3): p. 182-188.
191. D. Kashchiev. *Nucleation*. 2000: Butterworth-Heinemann.

192. J.W. Schmelzer, A.S. Abyzov. *Crystallization of glass-forming liquids: Specific surface energy*. The Journal of Chemical Physics, 2016. **145**(6): p. 064512.
193. D. Nguyen-Manh, D.G. Pettifor. *Electronic structure, phase stability and elastic moduli of AB transition metal aluminides*. Intermetallics, 1999. **7**(10): p. 1095-1106.
194. R. Goetzinger, M. Barth, D. Herlach. *Growth of lamellar eutectic dendrites in undercooled melts*. Journal of applied physics, 1998. **84**(3): p. 1643-1649.
195. C. Zener. *Phase transformations in steel*. Transactions of the Metallurgical Society, AIME, 1946. **167**: p. 550-559.
196. M.P. Hillert. *Internal Report, Swedish Inst. Met. Res., Stockholm, Sweden, 1953*.
197. H.I. Aaronson, J.B. Clark, C. Laird. *Interfacial Energy of Dislocation and of Coherent Interphase Boundaries*. Metal Science Journal, 1968. **2**(1): p. 155-158.
198. R.E. Smallman, R.J. Bishop. *Modern Physical Metallurgy and Materials Engineering: Science, Process, Applications*. 1999: Butterworth-Heinemann.
199. Y. Zhou, Y. Zhang, Y. Wang, G. Chen. *Solid solution alloys of Al Co Cr Fe Ni Ti x with excellent room-temperature mechanical properties*. Applied physics letters, 2007. **90**(18): p. 181904.
200. T. Borkar, B. Gwalani, D. Choudhuri, C. Mikler, C. Yannetta, X. Chen, R. Ramanujan, M. Styles, M. Gibson, R. Banerjee. *A combinatorial assessment of Al x CrCuFeNi 2 (0 < x < 1.5) complex concentrated alloys: Microstructure, microhardness, and magnetic properties*. Acta Materialia, 2016. **116**: p. 63-76.
201. F. He, Z. Wang, X. Shang, C. Leng, J. Li, J. Wang. *Stability of lamellar structures in CoCrFeNiNb x eutectic high entropy alloys at elevated temperatures*. Materials & Design, 2016. **104**: p. 259-264.
202. Ł. Rogal, J. Morgiel, Z. Świątek, F. Czerwiński. *Microstructure and mechanical properties of the new Nb25Sc25Ti25Zr25 eutectic high entropy alloy*. Materials Science and Engineering: A, 2016. **651**: p. 590-597.
203. W.-j. Liu, J. Li, C.-b. Shi, C.-m. Wang. *Effect of Micro-alloying Element Boron on the Strengthening of High-Strength Steel Q690D*. Metallography, Microstructure, and Analysis, 2015. **4**(2): p. 102-108.
204. T. Chaki. *Mechanism of boron-induced strengthening of grain boundaries in Ni3Al*. Philosophical Magazine Letters, 1991. **63**(3): p. 123-126.
205. S. Sun, Y. Tian, H. Lin, X. Dong, Y. Wang, Z. Zhang, Z. Zhang. *Enhanced strength and ductility of bulk CoCrFeMnNi high entropy alloy having fully recrystallized ultrafine-grained structure*. Materials & Design, 2017. **133**: p. 122-127.
206. L. Jiang, Z. Cao, J. Jie, J. Zhang, Y. Lu, T. Wang, T. Li. *Effect of Mo and Ni elements on microstructure evolution and mechanical properties of the CoFeNi x VMo y high entropy alloys*. Journal of Alloys and Compounds, 2015. **649**: p. 585-590.
207. C. Ai, F. He, M. Guo, J. Zhou, Z. Wang, Z. Yuan, Y. Guo, Y. Liu, L. Liu. *Alloy design, micromechanical and macromechanical properties of CoCrFeNiTax eutectic high entropy alloys*. Journal of Alloys and Compounds, 2018. **735**: p. 2653-2662.
208. L. Jiang, Z.Q. Cao, J.C. Jie, J.J. Zhang, Y.P. Lu, T.M. Wang, T.J. Li. *Effect of Mo and Ni elements on microstructure evolution and mechanical properties of*

- the CoFeNiVMoy high entropy alloys*. Journal of Alloys and Compounds, 2015. **649**(Supplement C): p. 585-590.
209. F. He, Z. Wang, P. Cheng, Q. Wang, J. Li, Y. Dang, J. Wang, C.T. Liu. *Designing eutectic high entropy alloys of CoCrFeNiNbx*. Journal of Alloys and Compounds, 2016. **656**(Supplement C): p. 284-289.
210. H. Jiang, H. Zhang, T. Huang, Y. Lu, T. Wang, T. Li. *Microstructures and mechanical properties of Co<sub>2</sub>MoxNi<sub>2</sub>VW<sub>x</sub> eutectic high entropy alloys*. Materials & Design, 2016. **109**(Supplement C): p. 539-546.
211. E. Hall. *The deformation and ageing of mild steel: III discussion of results*. Proceedings of the Physical Society. Section B, 1951. **64**(9): p. 747.
212. N. Petch. *The ductile-brittle transition in the fracture of  $\alpha$ -iron: I*. Philosophical Magazine, 1958. **3**(34): p. 1089-1097.
213. H. Kaya, M. Gündüz, E. Çadirli, O. Uzun. *Effect of growth rate and lamellar spacing on microhardness in the directionally solidified Pb-Cd, Sn-Zn and Bi-Cd eutectic alloys*. Journal of Materials Science, 2004. **39**(21): p. 6571-6576.
214. E. Cadirli, M. Gündüz. *The dependence of lamellar spacing on growth rate and temperature gradient in the lead-tin eutectic alloy*. Journal of Materials Processing Technology, 2000. **97**(1): p. 74-81.
215. I. Campos-Silva, E. Hernández-Sánchez, G. Rodríguez-Castro, H. Cimenoglu, J.L. Nava-Sánchez, A. Meneses-Amador, R. Carrera-Espinoza. *A study of indentation for mechanical characterization of the Fe<sub>2</sub>B layer*. Surface and Coatings Technology, 2013. **232**: p. 173-181.
216. A.H. Almasri, G.Z. Voyiadjis. *Nano-indentation in FCC metals: experimental study*. Acta Mechanica, 2009. **209**(1): p. 1.

## **Appendix A**

### **Abbreviations and Symbols**

- **Abbreviations**

BCC	=	Body Centred Cubic
CALPHAD	=	Calculation of Phase Diagram
BMG	=	Bulk Metallic Glass
DSC	=	Differential Scanning Calorimetry
DTA	=	Differential Thermal Analysis
EDS	=	Energy Dispersive Spectrometer
EHEA	=	Eutectic High Entropy Alloy
GFA	=	Glass Forming Ability
FCC	=	Face Centred Cubic
HEA	=	High Entropy Alloy
HE-BMG	=	High Entropy Bulk Metallic Glass
IM	=	Intermetallic
SS	=	Solid solution
SEM	=	Scanning Electron Microscopy
TEM	=	Transmission Electron Microscopy
EELS	=	Electron energy Loss Spectroscopy
SADP	=	Selected Area Diffraction Pattern
TRIP-DP	=	Transformation Induced Plasticity- Dual Phase
VEC	=	Valence Electron Concentration
XRD	=	X-Ray Diffraction
XRD-ECCI	=	X-Ray Diffraction - Electron Channelling Contrast

Image

- **Symbols**

$\delta$	=	Atomic size difference
$\Delta S_{\text{mix}}$	=	Mixing entropy
$\Delta\chi$	=	Electronegativity difference
$H_{\text{mix}}$	=	Enthalpy of mixing
$T$	=	Temperature
$G_{\text{mix}}$	=	Gibbs free energy of mixing
$\chi_i$	=	Pauling electronegativity
$S_{\text{conf}}$	=	Configurational entropy or entropy of mixing
$k$	=	Boltzmann's constant
$T_c$	=	Critical temperature
$x$	=	Crystallisation volume fraction
$r^*$	=	Critical radius
$\tau$	=	Thickness of cluster surface
$E_g$	=	Activation energy of glass transition
$E_x$	=	Activation energy of crystallisation
$E_p$	=	Activation energy of peak crystallisation
$G^{\text{mix}}$	=	Gibbs free energy of the liquid
$R$	=	Gas constant
$\beta$	=	Heating rate
$T_g$	=	Glass transition temperature
$T_x$	=	Crystallisation temperature
$T_m$	=	Melting temperature
$T_l$	=	Liquidus temperature
$T_p$	=	Peak temperature

$v^*$	=	Hard sphere volume
$x_i$	=	Atomic fraction
$\rho$	=	Density
$\Delta T_x$	=	Supercooled liquid region
$H_v$	=	Hardness
$H_0$	=	Initial hardness at room temperature
$k_l$	=	Strengthening coefficient
$\lambda$	=	Lamellar spacing
$X$	=	Parameter of proportionality from the Stefan-Skapski-Turnbull
$T_0$	=	Starting temperature for the crystallisation process
$T_\infty$	=	Ending temperature for the crystallisation process
$\tau$	=	incubation time
$n$	=	Avrami exponent
$k$	=	Kinetic coefficient as a function of absolute temperature
$\sigma$	=	Interfacial energy
$D$	=	Combined width of interlamellar spacing
$T_E$	=	Equilibrium temperature in K
$\Delta H_v$	=	Change in enthalpy per unit volume
$P_{\max}$	=	Maximum load
$A_r$	=	Indentation area

## Appendix B

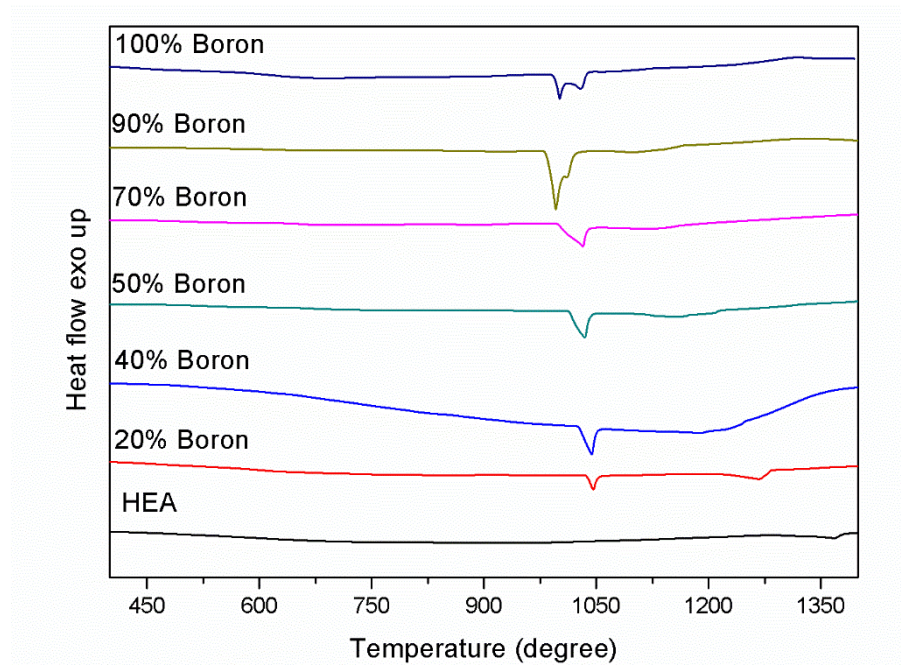


Figure A1: The DTA thermogram of FeCoNi(B<sub>x</sub>Al<sub>1-x</sub>)<sub>0.1</sub>Si<sub>0.1</sub> alloy with increase boron content

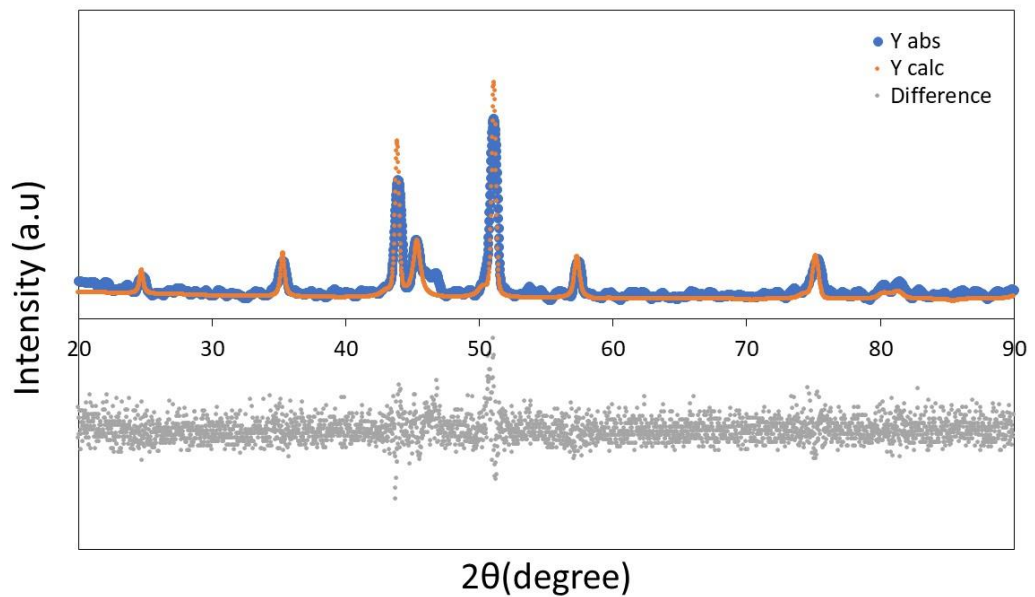


Figure A2: Rietveld refinement of B1.0 sample